

# The Design, Prototyping, Interfacing, and Control of an Innovative Schönflies Motion Generator

TR-CIM 06.05

Jorge Angeles, Stéphane Caro, Guillaume Hirigoyen, Waseem Khan, Alexei Morosov, Alessio Salerno, James Smith

October 13, 2006

## Contents

<b>1</b>	<b>Introduction</b>	<b>3</b>
1.1	Historical Notes and State of the Art . . . . .	3
1.2	The Schönflies-Motion Generator . . . . .	6
<b>2</b>	<b>Conceptual Design</b>	<b>8</b>
2.1	Candidate Morphologies . . . . .	8
2.1.1	The Topology . . . . .	8
2.1.2	The Actuation-sensing Subsystem . . . . .	11
2.2	The Morphology of Choice . . . . .	12
2.3	Embodiment . . . . .	12
2.4	Conclusions . . . . .	13
<b>3</b>	<b>Parameterization</b>	<b>14</b>
3.1	The Kinematics of the SMG . . . . .	14
3.1.1	Direct Kinematics . . . . .	14
3.1.2	Inverse Kinematics . . . . .	15
3.2	The Kinetostatic Design of the SMG . . . . .	15
3.2.1	Jacobian Matrices . . . . .	15
3.2.2	Singularity Analysis . . . . .	18
3.3	Dynamics of the SMG . . . . .	20
3.3.1	Inverse Dynamics of the parallel SMG . . . . .	21
3.4	The Drive Units . . . . .	24
3.4.1	Description . . . . .	24
3.4.2	Mechanism Kinematics . . . . .	25
3.4.3	Dynamics of the Drive Units . . . . .	27
3.5	The Right Angle Gear Boxes (RAGB) . . . . .	28
3.5.1	Description . . . . .	28
3.5.2	Dynamics of RAGB . . . . .	29
3.6	Dimensioning . . . . .	31
3.6.1	Trajectory-Planning . . . . .	31
3.6.2	SMG Dynamics . . . . .	34
3.6.3	Drive Dynamics . . . . .	35
3.6.4	Motor and Gear-Head Selection . . . . .	38

<b>4</b>	<b>Control of the McGill SMG</b>	<b>40</b>
4.1	Interfacing . . . . .	40
4.1.1	SMG Control box . . . . .	40
4.1.2	Rt-Lab Interface . . . . .	40
4.1.3	Sensors . . . . .	41
4.1.4	Encoders . . . . .	42
4.1.5	Analogue Input Circuit . . . . .	43
4.2	Control Algorithm . . . . .	44
4.2.1	PD linear Controller . . . . .	44
4.2.2	Inverse Dynamics controller . . . . .	44
4.2.3	Friction/Stiction Compensation . . . . .	45
4.3	Experiments . . . . .	46
4.3.1	Parameters settings . . . . .	46
4.3.2	First Test . . . . .	46
4.3.3	PD controller tests . . . . .	46
4.3.4	Comments . . . . .	47
<b>5</b>	<b>Detailed Design</b>	<b>50</b>
5.1	Design of links and joints . . . . .	50
5.2	Design of drives . . . . .	50
5.2.1	The support . . . . .	50
5.2.2	The Gearbox . . . . .	51
5.2.3	The Transmission . . . . .	53
5.2.4	Assembly . . . . .	54
<b>6</b>	<b>Test results</b>	<b>58</b>
<b>A</b>	<b>SMG Robot Control:Actuation System, I/O Control-Signal Board, and Motor-Starter Design &amp; Test</b>	
A.1	Introduction . . . . .	62
A.2	Motor and Servo Amplifier Dimensioning . . . . .	62
A.3	Gearhead Dimensioning . . . . .	63
A.3.1	Maximum Output Torque . . . . .	65
A.3.2	Extra Support for the Gearhead Pinion Shaft . . . . .	65
A.3.3	Reaction Forces . . . . .	65
A.3.4	Bending Moment and Shear Analysis . . . . .	67
A.4	Motor Starter Design and Testing . . . . .	71
A.4.1	Background Material . . . . .	71
A.4.2	Wiring Scheme . . . . .	77
A.4.3	Component Dimensioning . . . . .	80
A.4.4	Power . . . . .	80
A.4.5	Implementation . . . . .	82
A.4.6	Power supply circuit, Servomotor Wiring and Encoder Wiring Test . . . . .	82
A.4.7	Equipment and Test Set-up . . . . .	82
A.4.8	Warnings . . . . .	88
A.4.9	Turning on the Control Power Supply of the Power Amplifier . . . . .	88
A.4.10	Turning ON the Main Circuit Power Supply of the Power Amplifier . . . . .	88
A.4.11	Turning OFF the Main Circuit Power Supply of the Power Amplifier . . . . .	90
A.4.12	Alarm Signal Testing . . . . .	90
A.5	High Level Control of the Motor Amplifiers . . . . .	91

A.6	The Yaskawa SGD8-08AE-S Servo Amplifiers . . . . .	91
A.6.1	Signal Connectors . . . . .	91
A.7	Computer Interface Card: Sensoray Model 626 . . . . .	92
A.7.1	Home Position Calibration . . . . .	95
A.8	Appendix . . . . .	97
A.8.1	Bill of Materials . . . . .	97
A.8.2	Bending Moment of the Extra-Support Bearing Structure — Matlab Code . . . . .	98
<b>B</b>	<b>Carbon Fibre Limbs: Prototype Fabrication Methodology</b>	<b>100</b>
B.1	Basic Procedures . . . . .	100
B.1.1	Cutting out Pre-Preg Material . . . . .	100
B.1.2	Mold Preparation . . . . .	100
B.1.3	Bag Preparation . . . . .	100
B.1.4	Foam Rib Preparation . . . . .	100
B.2	Part Lay-up . . . . .	104
B.2.1	Schedule of Lay-up pieces . . . . .	104
B.2.2	Lay-up Instructions . . . . .	104
B.2.3	Air bag setup . . . . .	104
B.2.4	Oven setup . . . . .	106
B.2.5	De-molding . . . . .	108
B.3	Post-Machining . . . . .	110
B.3.1	Trimming rough edges . . . . .	110
B.3.2	Removing the end plugs . . . . .	110
B.3.3	Removing the vacuum bagging . . . . .	110
B.3.4	Cutting ends to size . . . . .	110
B.3.5	Preparing parts for bonding . . . . .	111
B.3.6	Bonding inserts into part . . . . .	112
B.3.7	Curing and Post-Curing . . . . .	113

## Abstract

# 1 Introduction

## 1.1 Historical Notes and State of the Art

Most robots used for industrial manufacturing have articulated structures of the serial type, where each link is coupled to two other links, except for the end links, which are coupled to one single neighbour. However, these simple, open kinematic chains of multi-axis machines suffer from some drawbacks, mostly due to the *pyramidal effects*: each axis must carry all other axes located upstream in the chain. The history of the development of modern robots with a parallel structure can be traced back to the early eighties (Merlet, 1997). As a milestone in this regard, Karl-Erik Neumann designed and built a new type of machine, the “parallel kinematic robot” (PKR), in 1987 (Brumson, 2005). This type of robot had three or more actuators, one end of each attached to the base, the other end to the end-platform. Thus, all actuators in such a robot are laid out in parallel. In spite of the early invention of parallel robots, they were not used widely until the early 90’s, since their architectures demanded sophisticated control not affordable with the computational means available at the time. After 1992, when Comau Pico launched the first multiprocessor controller, new control systems appeared on the market, able to run PKR a.k.a. parallel-kinematics machines (PKM).

Most PKM are based on hexapods, also known as Stewart or Gough-Stewart platforms (Stewart, 1965). A sample of PKM currently used in industry is displayed in Fig. 1(a)—(c).

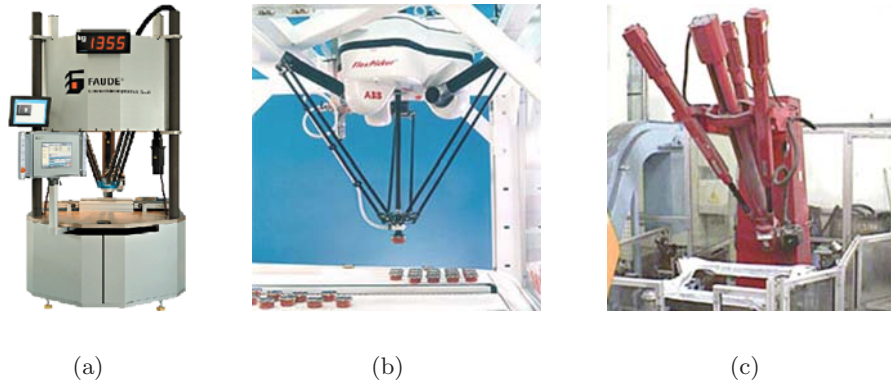


Figure 1: Parallel Robots: (a) Faude; (b) FlexPicker; (c) Tricept

The most widespread operation is machining. This includes milling, cutting, drilling and deburring of sheet and cast metal parts. For example, in 1999 more than two thirds of robotic applications of the inventors and manufacturers of Tricept technology, Neos Robotics AB (Sweden), were machining, where clients wanted to have 10 microns of repeatability, stiffer links, and higher power, while maintaining flexibility. The Tricept, shown in Fig. 1(c), is also used to hold laser and saw-cutting tools, as well as friction welders. The aerospace industry uses Tricept robots for fabricating propellers, turbine blades, impellers and other parts with intricate surfaces which require significant amount of contouring.

Other applications of PKM are as coordinate-measuring machines, such as KIM-750 (Lapic, Russia), Fig. 2(a), or as positioning devices, such as Hexapod (Hexel, USA), Fig. 2(b), which becomes possible also due to their high stiffness and accuracy.

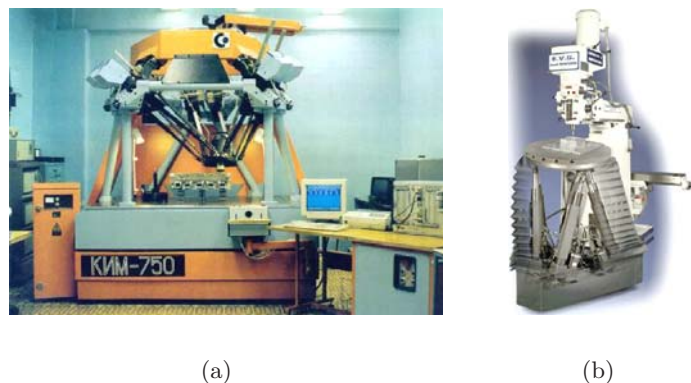
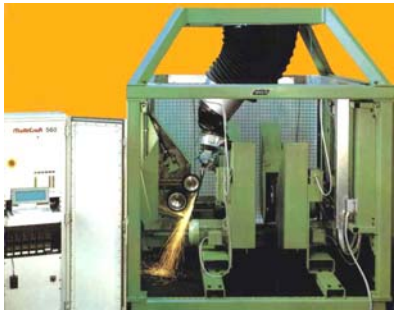


Figure 2: (a) Coordinate-measuring Machine KIM-750; (b) Hexapod, a positioning machine

Moreover, nowadays more and more PKM are not used independently but as parts of precise machine-tools. The fact of the matter is that high stiffness and high accuracy are as yet to be realized with PKM. Some examples of machine tools with a parallel architecture are MC-560 for polishing (Greif, Germany), Fig. 3(a), Triomaxx for glass-cutting and milling (Fooke, Germany), Fig. 3(b), TriCenter DMT 100, a milling machine for the aeronautics industry, (Deckel Maho, Germany), Fig. 3(c), Hexel Tornado 2000, a five-axis milling machine, (Hexel, USA), Fig. 4(a), TM 1000, a milling and measuring machine, (Lapik, Russia), Fig. 4(b).



(a)



(b)



(c)

Figure 3: (a) Polishing MC-560; (b) Glasscutting/Milling Triomaxx; (c) Milling TriCenter DMT 100 Machines



(a)



(b)

Figure 4: (a) Milling Machine Hexel Tornado 2000; (b) Milling and Measuring Machine TM 1000

Other possible applications of PKM are as medical manipulators, educational test benches, and pharmaceutical setups.

Parallel manipulators have obvious advantages over their serial counterparts. Since PKM are built with closed-loop chains, the expected result of the parallel design is a robot with higher stiffness, and hence, with increased structural stability. In PKM there is no need to carry motors, because all drives are installed on the fixed base; as a result, the links can be more compact and lighter. This should allow for shorter cycle times than with serial architectures.

Therefore, in PKM we should achieve the flexibility of a robot combined with the stiffness of a machine tool. As a consequence, parallel machines should have an accuracy comparable with those of CNC machine-tools, but at a lower cost.

For example, the Tricept, Fig. 1(c), PKM has a positioning accuracy of 0.05 mm and a repeatability of 0.010 mm; the five-axis milling machine Hexel Tornado 2000, Fig. 4(a), has a positioning accuracy of 0.025 mm and a repeatability of 0.01 mm.

The most impressive application for hexapod PKM is in machine tools for turbine and jet-engine-blade polishing and deburring, where very high accuracy is needed for machining these parts with highly complex shapes.

## 1.2 The Schönflies-Motion Generator

The Schönflies-Motion Generator (SMG) is an innovative robot, under development at McGill University; unlike hexapods the McGill University SMG has two legs, each supplied with four joints. This manipulator is capable of a special class of motions, namely, those produced with manipulators termed SCARA, an acronym for *Selective-Compliance Assembly Robot Arm*. These motions involve three independent translations and one rotation about an axis of fixed direction, similar to the motions undergone by the tray of a waiter. Such motions are known to form a subgroup of the displacement group of rigid-body motions, termed the Schönflies subgroup (Bottema and Roth, 1979; Hervé, 1978).

The SMG is a manipulator producing four-degree-of-freedom displacements of a rigid body, its moving platform (Angeles and Morozov, 2003a). This set of displacements was first studied by the German mathematician-mineralogist Arthur Moritz Schönflies (1853-1928), who found that these displacements have the algebraic structure of a group. For this reason, the set of such motions is known to geometers as the Schönflies subgroup of the group of rigid-body displacements.

The displacements comprise three independent translations and one rotation about an axis of fixed orientation with respect to a fixed base. The SMG is composed of two identical four-degree-of-freedom serial chains in a parallel array, sharing one common base and one common moving platform.

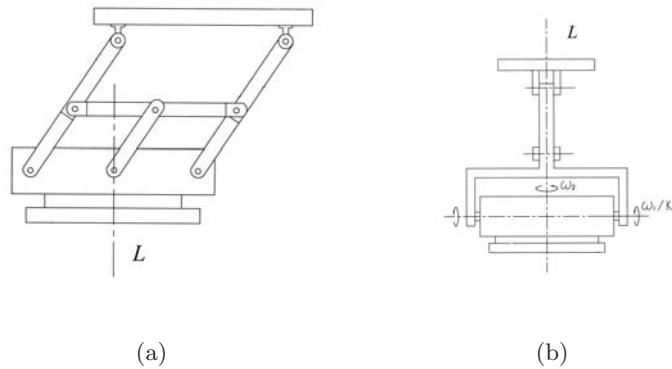


Figure 5: An SMG parallelogram module

Each serial chain comprises two cascaded modules, displayed in Figs. 5(a)—(b), producing, each, a set of two-degree-of-freedom displacements: one rotation about an axis parallel to a line  $L$  fixed to the base, the *pan motion*, and one rotation about an horizontal axis, the *tilt motion*. Besides, the axes of the first-proximal-modules are also fixed. Moreover, the planes of the two circles make a variable dihedral angle.

On the one hand, the proximal module is active and has two controlled axes. The motors are installed on the fixed base. The links can thus be made very light, thereby allowing for higher operational speeds. On the other hand, the distal module is passive and follows the motions of the active one, the whole mechanism giving, as a result, a four-degree-of-freedom motion to its end-platform. A perspective view of the system is displayed in Fig. 6.

Each leg is driven by a pair of identical motors. The whole mechanism, with the four motors installed either at the ceiling or on the floor, provides a manipulation system with a horizontal end-effector having the motion capability of a SCARA manipulator, thereby giving such a motion to a gripperholding rigidly a tool or a workpiece.

Identical motors performing identical tasks means ease of programming and maintenance as well as equal wear. Location of motors on the base, moreover, allows for lighter links and, as a consequence, higher operation speeds. A planetary gear train is used to drive each leg of the moved manipulator.

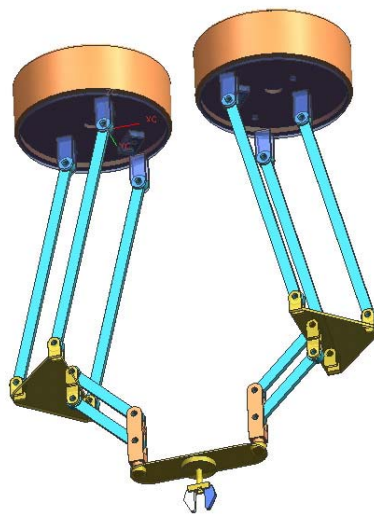


Figure 6: Schönflies-Motion Generator

## 2 Conceptual Design

### 2.1 Candidate Morphologies

The morphology of the robot, for our purposes, comprises two items: the topology and the actuation-sensing subsystem. These two items are given due consideration in this section.

#### 2.1.1 The Topology

We start by defining the *topology* of the kinematic chain, which can be serial, parallel, or hybrid. The most common topology is serial, with three revolute of vertical axes, the fourth one being prismatic, and capable of moving the load up and down. For the production of Schönflies motions, it is immaterial where the prismatic joint is located. Industrial SCARA systems bear the prismatic joint either as the proximal or as the distal joint. This topology occurs in industrial robots bearing the trademark names Adept, Epson, and Fanuc, among others. One novel class of SCARA systems, those of the M-410iB and M-420iA series, manufactured by Fanuc Robotics, and the  $\dots\dots$ , produced by ABB Robotics, exhibit the innovative II joint, as introduced by [Dietmaier \(1992\)](#), [Hervé and Sparacino \(1992\)](#) and [Wohllhart \(1992\)](#).

The II joint is nothing but a parallelogram four-bar linkage, whose two coupled links are the frame and the “coupler” links, the II joint thus allowing for pure translations of the coupler with respect to the base, all points of the coupler link tracing circles of a common radius. The FANUC and the ABB SCARA systems bear a topology formed by a concatenation of two II joints of a common vertical plane, which can pan about a vertical axis. At the coupler link of the distal II joint, moreover, a fourth axis is added, which allows for a second pan motion. This architecture is, thus, of the RIIIR type. Moreover, these SCARA systems feature two identical motors mounted on a panning base, to actuate each of the II joints, the underlying topology thus being hybrid.

A paradigm hybrid robot of the SMG type is that obtained by a concatenation of a parallel structure known as *Delta* ([Clavel, 1988](#)) and one fourth axis collocated in series on its moving platform. Delta itself allows for pure translations in three independent directions, with a parallel structure under which its three identical legs are kinematic chains of the RRIIR type. A hybrid robot with this architecture is manufactured by ABB Robotics under the trade name FLEXPICKER IRB 340; a second robot, the SIG XR22, is manufactured by SIG Pack Systems AG.

An alternative hybrid robot was introduced in ([Angeles et al., 2000](#)). This robot, dubbed the macro-manipulator of a Multi-modular Manipulating ( $M^3$ ) System, is displayed in Fig. 7(a). The underlying kinematic chain is a concatenation of two parallel subchains, each capable of producing a pan-tilt motion of its end link using two identical motors fixed to the base. While the computer-generated model of the foregoing figure depicts a serial array of two two-dof parallel subchains, the actual prototype, shown in Fig. 7(b), was built with a serial array, as imposed by budgetary constraints.

Yang and collaborators ([Yang et al., 2001](#)) reported a rich variety of 50 parallel SMG, some of them with II joints, but stayed short of exploiting these to their fullest extent. However, only one parallel robot of the SMG type has been prototyped, the H4, disclosed in European Patent EP1084802 ([Company et al., 2001](#)). This robot comprises four identical legs, each being a serial kinematic chain of the SMG type. The Schönflies motion produced by each leg has its axis of rotation horizontal, all four axes being laid out so as to form a square. The parallel array of the four legs thus, according with group theory as applied to kinematic chains ([Angeles, 2004](#)), is capable of producing three independent translations. Had the inventors of this ingenious device chosen a design of the legs with a common axis of rotation, they could have spared the complicated mechanism needed between the end of each leg and the moving platform.

**A Complexity Analysis of the Topology of the Kinematic Chain** At the outset, we assign complexity values to the various joints, P, R and II. The complexity of the P and R joints is readily



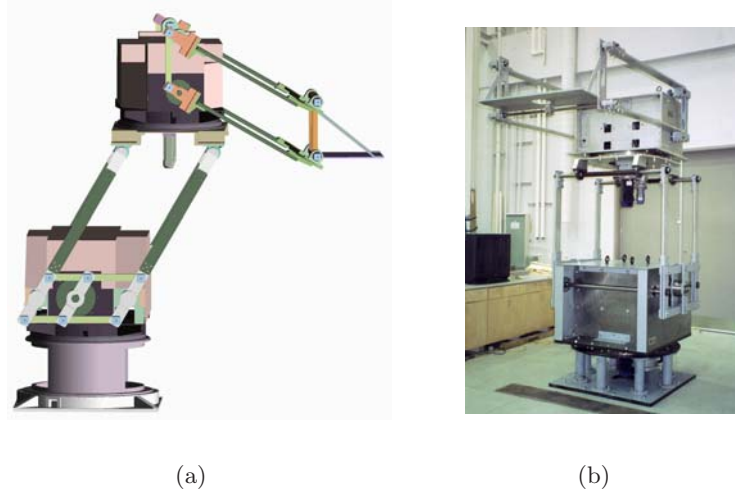


Figure 7: Macro-manipulator of the  $M^3$  system: (a) a computer-generated model and (b) the physical prototype

assigned by looking at the surface associated with each of these joints. Indeed, these joints are two of the six *lower kinematic pairs* of kinematic chains. By definition, a lower kinematic pair is the coupling of two rigid bodies via a common surface (Denavit and Hartenberg, 1964). The surface of the prismatic joint is a prism, as the name indicates, that of a revolute a cylinder. The simplest possible prism is one whose cross section is an equilateral triangle. Hence, the complexities  $K_P$  and  $K_R$  of the P and the R joints, respectively, can be assigned based on that of their cross sections. As a consequence, then, and recalling the arguments put forth by (Angeles, 2005), the kinematic complexities of the prismatic and revolute joints,  $K_P$  and  $K_R$ , respectively,

$$K_P = 1, \quad K_R = 0 \quad (1)$$

Now, to assign a complexity value to the  $\Pi$  joint, we realize that this is not a lower kinematic pair, because contact between the coupled bodies does not occur along a common surface. Actually, contact between the coupled bodies does not occur directly. In order to assign a complexity value to this joint, we define the complexity of a kinematic chain with respect to its type of joints as the mean value of its joint complexities. Hence,

$$K_\Pi = 0 \quad (2)$$

which is plausible if we consider the ease with which this joint can be manufactured and the longstanding experience that the mechanical design community has in designing with this type of joints, from drafting instruments to movable lamps, and so on.

We now can compare various alternative topologies from the complexity viewpoint. Figures 8(a)—(c) depict three alternative serial topologies to produce Schönflies motions.

According to our complexity measure, then, the joint-complexity  $K_J$  of the three topologies of Figs. 8(a)—(c) are, respectively,

$$(K_J)_a = 0.25, \quad (K_J)_b = 0.5, \quad (K_J)_c = 0.75 \quad (3)$$

where  $(K_J)_a$  is the lowest, regardless of the actual location of the P joint in the chains.

Since one prismatic joint in the design of a serial SMG is unavoidable, the robot of this kind with the lowest complexity from the viewpoint of topology and joint complexities is one with a kinematic chain

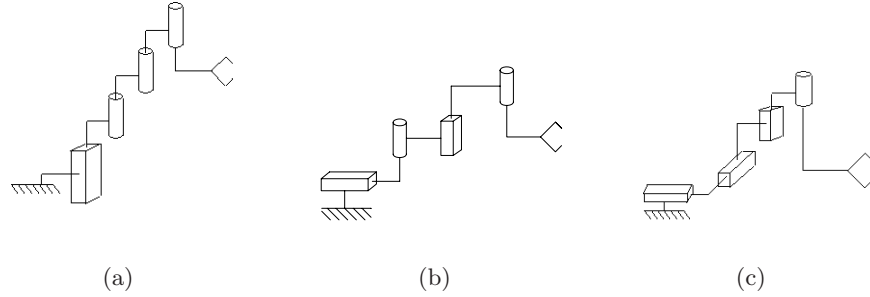


Figure 8: Three alternative serial kinematic chains to produce Schönflies motions: (a) PRRR; (b) PRPR; and (c) PPPR

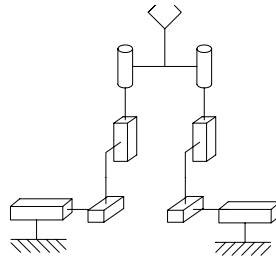


Figure 9: A possible SMG with two legs

of the type of Fig. 8(a), or its variant, whereby the P joint is located anywhere in the chain, with a complexity of 0.25.

The joint complexity of the FANUC and the ABB SCARA systems is, thus 0. Now, regarding parallel topologies, we realize that these can be readily obtained by means of two or more legs coupling the moving plate with the base plate, provided that all legs are generators of the *same* Schönflies subgroup. Now, one serial SMG should not have more than four joints, which is the number of joints needed per leg. Moreover, a parallel SMG can have a minimum of two legs, the total minimum number of joints expected in a SMG thus being eight. Any number of joints in excess of this minimum, thus, adds to the complexity of the topology. If  $N$  denotes the number of joints, then, the complexity  $K_{\parallel}$  of a parallel SMG can be assigned as

$$K_{\parallel} = 1 - e^{-(N-8)} \quad (4)$$

Shown in Fig. 2.1.1 is a possible parallel SMG with two legs, each being a SMG of the PPPR type. The joint complexity  $C_J$  of this topology can be assigned as that of its legs, or 0.75. The complexity  $K_{\parallel}$  of this topology with respect to its number of joints is 0, according with expression (4). The total topology complexity,  $C_t$ , of the chain is then assigned as a *convex combination* (Hillier and Lieberman, 1995) of its two complexities, namely, as

$$K_t = w_1 K_J + w_2 K_{\parallel} \quad (5)$$

with  $w_1 + w_2 = 1$ , and  $0 \leq w_i \leq 1$ , for  $i = 1, 2$ , defined as weights assigning relative relevance to each of the two complexities. In the absence of further considerations (so far), we can just assign  $w_1 = w_2 = 0.5$ , and hence, the SMG of Fig. ?? has a topological complexity of 0.375.

Disclosed in (Angeles and Morozov, 2003b) is a family of parallel SMG with two and four legs, instances thereof being displayed in Figs. 10(a)–(b).

The topological complexity of the SMG of Fig. 10(a) is thus 0, that of Fig. 10(b) being

$$K_t = 0.5(0) + 0.5(1 - e^{-(16-8)}) = 0.4998 \quad (6)$$

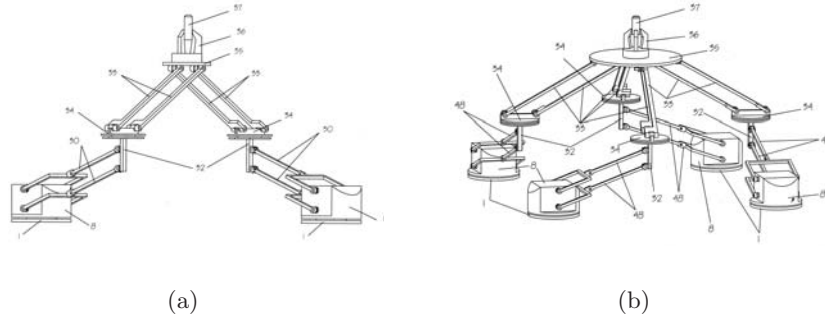


Figure 10: Two instances of parallel SMG with: (a) two legs, and (b) four legs

As a comparison, we compute the topological complexity of the H4. We first note that the parallelograms of this device are designed with self-aligning revolute, equivalent to the serial array of two R joints of intersecting axes. Hence, each II joint of the H4 has eight R joints. The total number of joints of the H4 is, thus, 40, and hence, its topological complexity is

$$K_t = 0.5(0) + 0.5(1 - e^{-(40-8)}) = 0.5 \quad (7)$$

### 2.1.2 The Actuation-sensing Subsystem

For our purposes, we consider the simplest sensing subsystem: joint encoders, for angular-displacement and joint-rate measurements, located at the motor shafts. Under these conditions, the morphology of this subsystem focuses only on the motors. We have the alternatives below:

- Physical principle: electric (AC or DC), hydraulic, pneumatic, or piezo-electric;
- power rating; and
- torque and rpm characteristics.

We assume that the physical actuation principle has already been determined, as well as the total power  $P_t$  required, while torque and rpm characteristics are to be decided on at a later stage. The only item to be decided on at the conceptual-level design stage is how the power will be distributed among all motors. If we have  $N_m$  motors, the  $i$ th being rated at a power  $P_i$ , the coefficient of variation  $C_m$  of the motors is, then, computed in terms of the power distribution. Here, in the absence of link dimensions and link material properties, we cannot assign specific percentages to the various motors. We thus use heuristic rules, based on an assumption of power distribution:

1. If the topology is serial, then the power requirement for each motor is monotonically decreasing from the proximal to the distal motor. Since all motors are rated at different power values, we assume here a maximum actuational complexity, namely,  $K_a = 1.0$ .
2. If the topology is hybrid, then we can have subsets of identical motors, which decreases the diversity (coefficient of variation), and hence, the complexity of the actuation-sensing subsystem. If two motors are identical, then  $K_a = 0.75$ ; if three motors are identical, then  $K_a = 0.5$ ; in the case of two pairs of identical motors,  $K_a = 0.25$ . All four motors cannot be identical in a hybrid robot.
3. If the topology is parallel, then we have subsets of identical motors, similar to the hybrid case, but now we can have all four motors identical, which yields an actuational complexity  $K_a = 0$ .

For example, industrial SCARA of the serial type have a  $K_a = 1.0$ , but the M-410iB and the ... ABB ..., with two identical motors, have a hybrid topology and hence, a  $K_a = 0.75$ . The hybrid robot of Fig. 7(a) has two pairs of identical motors each, and hence, a  $K_a = 0.25$ , while H4, a parallel robot, has a  $K_a = 0$ .

We describe below the conceptual design of an innovative family of SMG.

## 2.2 The Morphology of Choice

Based on the foregoing considerations, we chose a parallel morphology. We devised morphologies with two and four legs, as exemplified in Figs. 10(a)—(b).

For the four-legged morphology, the total number of joints is 16, and hence, the joint complexity of this morphology is  $K_J = 1 - e^{-(16-8)} = 0.9997$ , a rather large joint complexity. The two-legged version shows a joint complexity of 0, for it has the very minimum of joints. However, notice that the overall structure being overconstrained, nothing guarantees that, upon assembling each leg separately, the axes of the distal revolutes will be parallel, in light of manufacturing and assembly errors. For this reason, one additional revolute is needed, of axis normal to one of the foregoing two, which adds one extra joint, and hence, the joint complexity of the final morphology of choice is  $K_J = 1 - e^{-1} = 0.632$ .



Figure 11: Intermediate embodiment of the morphology of choice

## 2.3 Embodiment

Shown in Fig. 11 is an intermediate embodiment of the morphology of choice. In this morphology, each leg is of the RIIIR type, with the proximal II joint stronger than its distal counterpart. The former is displayed with two parallel plates of LTM 25 Carbon Fiber/Epoxy, a carbon-fibre composite, the latter with two tubes in composite either.

## 2.4 Conclusions

We have outlined the process behind the design of the morphology of a parallel Schönflies-motion generator. The main design decisions were based on complexity issues. We thus introduced three pertinent items: joint-type complexity; joint-number complexity; and actuational-sensorial complexity. After reviewing various possible alternatives, we zeroed-in on a parallel topology with two identical legs, using four identical motors of vertical axes.

### 3 Parameterization

#### 3.1 The Kinematics of the SMG

##### 3.1.1 Direct Kinematics

The kinematic chain of the SMG is shown in Figs. 12 and 13. We first introduce the notation which will be used throughout this report. For starters, all symbols with double subscripts, comprising one Roman and one Arabic numeral, refer to the leg,  $I$  or  $II$ , and to the corresponding item of the respective leg.

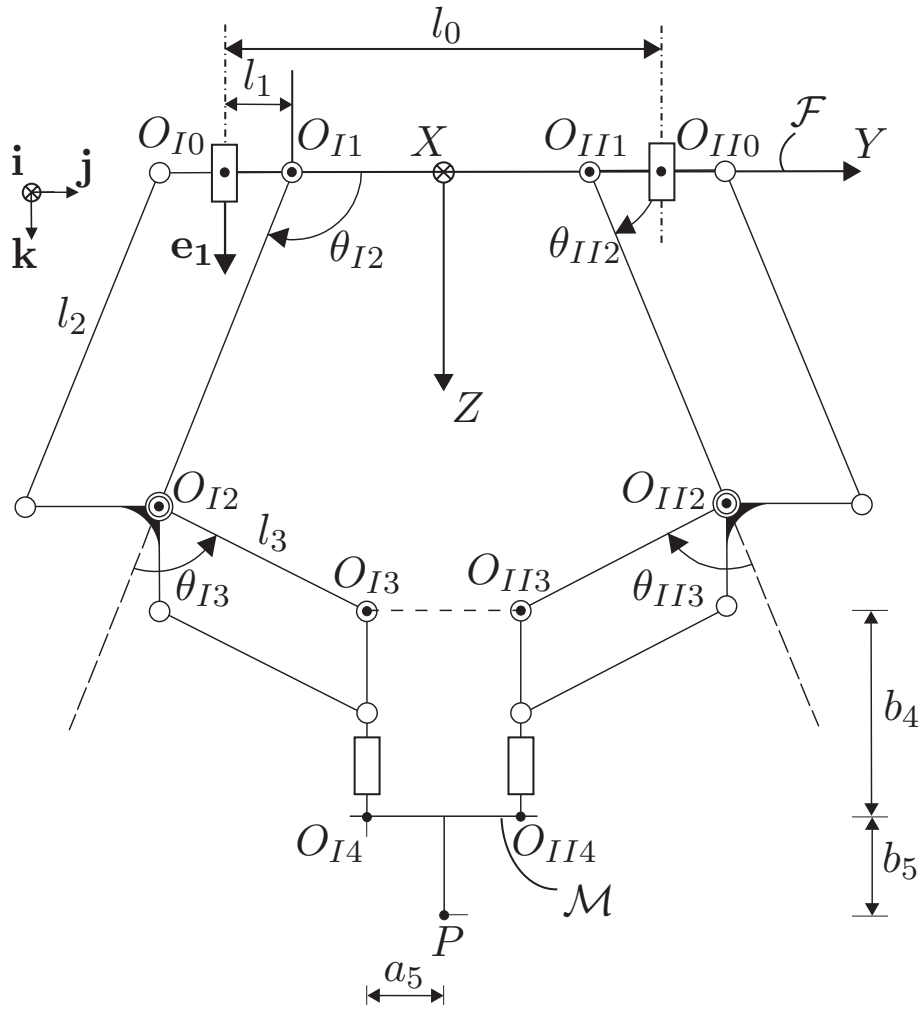


Figure 12: Kinematic chain of the parallel Schönflies-Motion Generator: front view

Notation	Description
$\{x, y, z\}$	the Cartesian coordinates of the operation point $P$ of the end-effector expressed in the coordinate frame $\mathcal{F}(O_{I0}, \mathbf{i}, \mathbf{j}, \mathbf{k})$
$\phi$	angle of rotation of the end-effector about the vertical axis
$\theta_{J_i}$	angle of rotation, measured according with the right-hand rule
$\mathbf{a}_{J_k}$	$\overrightarrow{O_{J(k-1)}O_{Jk}}$ , for $k = 1, 2, 3, 4$
$\mathbf{a}_{J_5}$	$\overrightarrow{O_{J4}P}$
$a_i$	the projection of $\mathbf{l}_{J_i}$ onto the $X - Y$ plane, for $i = 4, 5$

Next page

Notation	Description
Next...	
$b_i$	the projection of $\mathbf{l}_{Ji}$ onto the $Z$ axis, for $i = 4, 5$
$l_i$	$\ \mathbf{a}_{Ji}\ $
$R$	“radius” of the end effector, i.e. the distance between the operation point
$l_0$	distance between the two fixed bases (Drive-Units)

Table 1: Nomenclature

where  $J = I, II$  and  $i = 1, 2, 3, 4, 5$ .

We further define  $\theta_{I1}$ ,  $\theta_{I2}$ ,  $\theta_{II1}$ , and  $\theta_{II2}$  as the four actuated-joint angles, while  $\theta_{I3}$ ,  $\theta_{I4}$ ,  $\theta_{II3}$ , and  $\theta_{II4}$  are the four passive-joint angles. Correspondingly,  $\dot{\theta}_{I1}$ ,  $\dot{\theta}_{I2}$ ,  $\dot{\theta}_{II1}$ , and  $\dot{\theta}_{II2}$  are the four actuated-joint rates.

Then, from the geometric relationships shown in the above figures, we can obtain the geometric relations for leg  $I$ :

$$x = -(l_1 + l_2 \cos \theta_{I2} + l_3 \cos \theta_{I23} + a_4) \sin \theta_{I1} - R \sin \phi \quad (8a)$$

$$y = (l_1 + l_2 \cos \theta_{I2} + l_3 \cos \theta_{I23} + a_4) \cos \theta_{I1} + R \cos \phi \quad (8b)$$

$$z = l_2 \sin \theta_{I2} + l_3 \sin \theta_{I23} + b_4 + b_5 \quad (8c)$$

$$\phi = \theta_{I1} + \theta_{I4} \quad (8d)$$

where

$$\theta_{I23} \equiv \theta_{I2} + \theta_{I3}$$

Similarly, for leg  $II$ , we have:

$$x = (l_1 - l_2 \cos \theta_{II2} - l_3 \cos \theta_{II23} + a_4) \sin \theta_{II1} + R \sin \phi \quad (9a)$$

$$y = l_0 - (l_1 - l_2 \cos \theta_{II2} - l_3 \cos \theta_{II23} + a_4) \cos \theta_{II1} - R \cos \phi \quad (9b)$$

$$z = l_2 \sin \theta_{II2} + l_3 \sin \theta_{II23} + b_4 + b_5 \quad (9c)$$

$$\phi = \theta_{II1} + \theta_{II4} \quad (9d)$$

where

$$\theta_{II23} \equiv \theta_{II2} + \theta_{II3}$$

### 3.1.2 Inverse Kinematics

To compute the Inverse Kinematics of the manipulator, we used eqs. (8a—d) and (9a—d), and the Matlab *fsolve* function (Mathworks, 2002), which aims at solving nonlinear equations by a least-square method.

## 3.2 The Kinetostatic Design of the SMG

### 3.2.1 Jacobian Matrices

The kinematic chain of the SMG is shown in Figs. 12 and 14.

From Fig. 14, one readily derive

$$\mathbf{p}_I = \mathbf{a}_{I1} + \mathbf{a}_{I2} + \mathbf{a}_{I3} \quad (10a)$$

$$\mathbf{p}_{II} = \mathbf{a}_{II1} + \mathbf{a}_{II2} + \mathbf{a}_{II3} + l_0 \mathbf{j} \quad (10b)$$

where  $\mathbf{p}_I$  and  $\mathbf{p}_{II}$  denote the position vectors of point  $P_I$  and  $P_{II}$ , respectively. Moreover, notice that all vectors of the above equations must be expressed in the same frame; otherwise, the addition would not be possible. Upon differentiating both sides of eq. (10), we obtain

$$\dot{\mathbf{p}}_J = \mathbf{J}_J \dot{\theta}_J \quad , \quad J = I, II \quad (11)$$

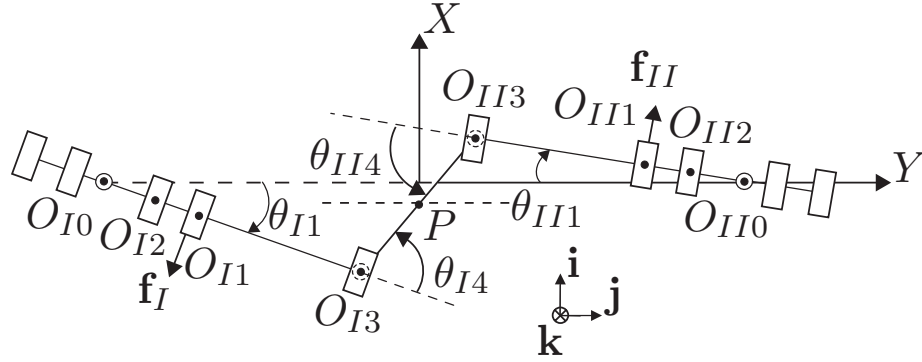


Figure 13: Kinematic chain of the parallel Schönflies-Motion Generator: top view

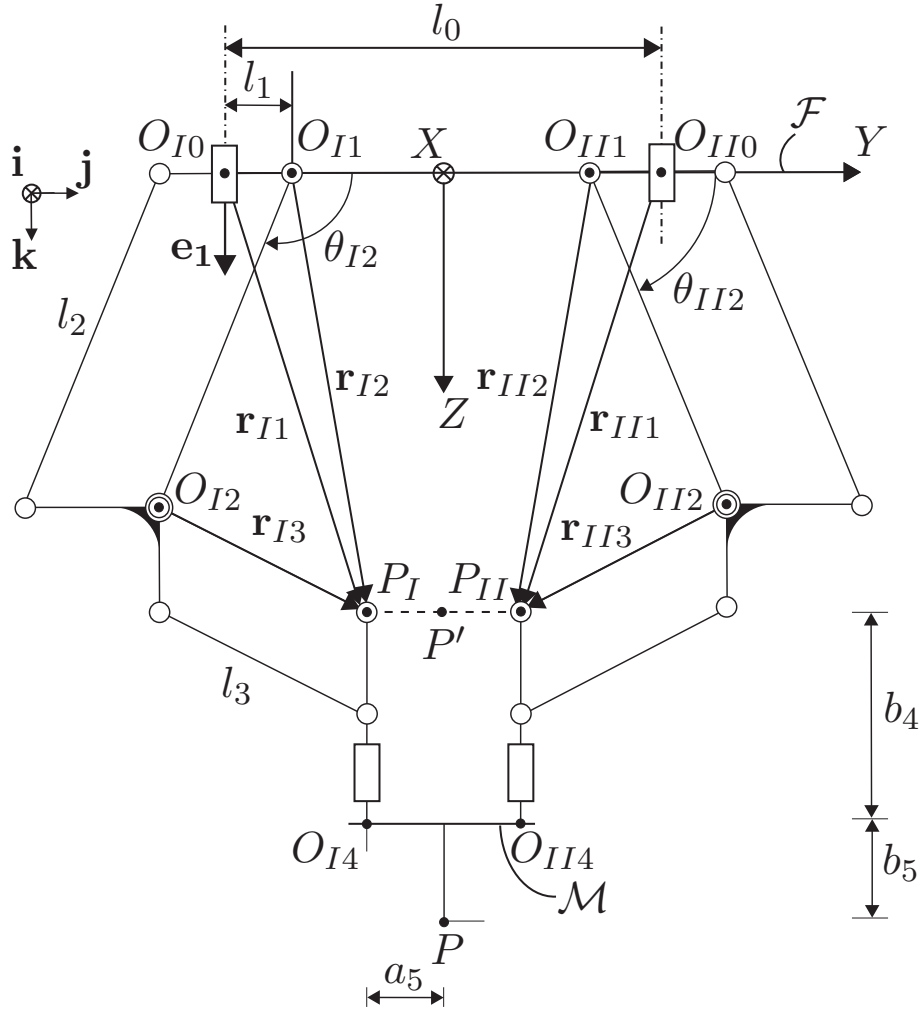


Figure 14: Vectors describing the kinematic chain of the parallel Schönflies-Motion Generator

where  $\dot{\theta}_J$  is the the 3-dimensional *joint-rate vector* of leg  $J$  defined as

$$\dot{\theta}_J = [\dot{\theta}_{J1} \ \dot{\theta}_{J2} \ \dot{\theta}_{J3}]^T \quad , \quad J = I, II \quad (12)$$



and  $\mathbf{J}_J$  is its *Jacobian matrix*, defined as the  $3 \times 3$  matrix shown below:

$$\mathbf{J}_J = [\mathbf{k} \times \mathbf{r}_{J1} \quad \mathbf{f}_J \times \mathbf{r}_{J2} \quad \mathbf{f}_J \times \mathbf{r}_{J3}] \quad , \quad J = I, II \quad (13)$$

where  $\mathbf{r}_{Ji} = \sum_{k=i}^3 \mathbf{a}_{Jki}$ ,  $i = 1, 2, 3$ , while  $\mathbf{k}$  is the unit vector associated with the first revolute joint of legs  $I$  and  $II$ , and  $\mathbf{f}_J$  is the unit vector associated with the  $\Pi$  joints of leg  $J$ ,  $J = I, II$ .

In order to get obtain a normalized expression of eq.(11), let us divide it by  $l_0$ , which is a *characteristic length*, as yet to be determined:

$$(\mathbf{k} \times \boldsymbol{\rho}_{J1}) \dot{\theta}_{J1} + (\mathbf{f}_J \times \boldsymbol{\rho}_{J2}) \dot{\theta}_{J2} + (\mathbf{f}_J \times \boldsymbol{\rho}_{J3}) \dot{\theta}_{J3} = \dot{\boldsymbol{\sigma}}_J \quad (14)$$

where

$$\boldsymbol{\rho}_{Ji} \equiv \frac{1}{l_0} \mathbf{r}_{Ji} \quad , \quad i = 1, 2, 3 \quad (15a)$$

$$\boldsymbol{\sigma}_J \equiv \frac{1}{l_0} \mathbf{p}_J \quad , \quad J = I, II \quad (15b)$$

In order to eliminate the passive joint rates  $\dot{\theta}_{J3}$ ,  $J = I, II$ , we cross-multiply both sides of eq.(14) by  $\mathbf{f}_J \times \boldsymbol{\rho}_{J3}$ , from the left, thereby obtaining

$$\mathbf{v}_J \dot{\theta}_{J1} + \Delta_J \mathbf{f}_J \dot{\theta}_{J2} = (\mathbf{f}_J \times \boldsymbol{\rho}_{J3}) \times \dot{\boldsymbol{\sigma}}_J \quad (16)$$

with

$$\begin{aligned} \mathbf{v}_J &\equiv [(\mathbf{f}_J \times \boldsymbol{\rho}_{J3}) \cdot \boldsymbol{\rho}_{J1}] \mathbf{k} - [(\mathbf{f}_J \times \boldsymbol{\rho}_{J3}) \cdot \mathbf{k}] \boldsymbol{\rho}_{J1} \\ &\equiv [\mathbf{f}_J, \boldsymbol{\rho}_{J3}, \boldsymbol{\rho}_{J1}] \mathbf{k} - [\mathbf{f}_J, \boldsymbol{\rho}_{J3}, \mathbf{k}] \boldsymbol{\rho}_{J1} \end{aligned} \quad (17)$$

and

$$\Delta_J \equiv [(\mathbf{f}_J \times \boldsymbol{\rho}_{J3}) \cdot \boldsymbol{\rho}_{J2}] \equiv [\mathbf{f}_J, \boldsymbol{\rho}_{J3}, \boldsymbol{\rho}_{J2}] \quad (18)$$

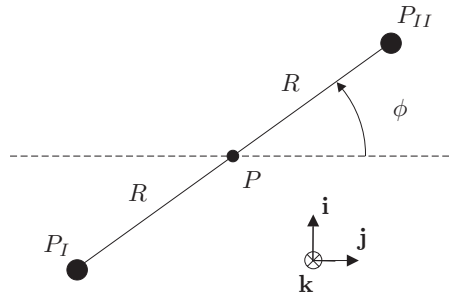


Figure 15: Top view of the moving plate in vector form

From Fig. 15,

$$\dot{\boldsymbol{\sigma}}_J = \dot{\boldsymbol{\sigma}} + \frac{1}{2} \dot{\phi} S(J) \mathbf{k} \times (\boldsymbol{\sigma}_I - \boldsymbol{\sigma}_{II}) \quad (19)$$

with

$$S(J) = \begin{cases} +1 & \text{if } J = I \\ -1 & \text{if } J = II \end{cases} \quad (20)$$

and

$$\boldsymbol{\sigma} = \frac{1}{l_0} \mathbf{p} \quad (21)$$

From eqs.(19) and (20), we obtain

$$\mathbf{v}_J \dot{\theta}_{J1} + \Delta_J \mathbf{f}_J \dot{\theta}_{J2} = (\mathbf{f}_J \times \boldsymbol{\rho}_{J3}) \times \left[ \dot{\boldsymbol{\sigma}} + \frac{1}{2} \dot{\phi} S(J) \mathbf{k} \times (\boldsymbol{\sigma}_I - \boldsymbol{\sigma}_{II}) \right] \quad (22)$$

which can be written in vector form

$$\mathbf{A}_J \mathbf{t} = \mathbf{B}_J \dot{\boldsymbol{\gamma}}_J, \quad J = I, II \quad (23)$$

with the definitions below:

$$\mathbf{A}_J \equiv \left[ \frac{1}{2} S(J) \boldsymbol{\Phi}_J [\mathbf{k} \times (\boldsymbol{\sigma}_I - \boldsymbol{\sigma}_{II})] \boldsymbol{\Phi}_J \right] \in \mathbb{R}^{3 \times 2}, \quad \mathbf{B}_J \equiv [\mathbf{v} \ \Delta_J \mathbf{f}_J] \in \mathbb{R}^{2 \times 4} \quad (24a)$$

$$\dot{\boldsymbol{\gamma}}_J \equiv \begin{bmatrix} \dot{\theta}_{J1} \\ \dot{\theta}_{J2} \end{bmatrix}, \quad \mathbf{t} \equiv \begin{bmatrix} \dot{\phi} \\ \dot{\boldsymbol{\sigma}} \end{bmatrix}, \quad \boldsymbol{\phi}_J \equiv \mathbf{f}_J \times \boldsymbol{\rho}_{J3} \quad (24b)$$

and  $\boldsymbol{\Phi}_J$  is the *cross-product matrix* of vector  $\boldsymbol{\phi}_J$  (Angeles, 2002).

Next, we consider both legs. Upon ‘‘stacking’’ the two corresponding kinematic relations derived from eq.(23), we obtain the kinematic relation for the whole system, namely,

$$\mathbf{A} \mathbf{t} = \mathbf{B} \dot{\boldsymbol{\theta}} \quad (25)$$

where the twist  $\mathbf{t}$  was defined in eq.(24), the vector of active joint rates  $\dot{\boldsymbol{\theta}}$ , the forward Jacobian  $\mathbf{A}$ , and the inverse Jacobian  $\mathbf{B}$  being defined, in turn, as

$$\dot{\boldsymbol{\theta}} \equiv [\ \dot{\gamma}_I \ \dot{\gamma}_{II} \ ] \in \mathbb{R}^4 \quad (26a)$$

$$\mathbf{A} \equiv \begin{bmatrix} \mathbf{A}_I \\ \mathbf{A}_{II} \end{bmatrix} \in \mathbb{R}^{6 \times 4} \quad (26b)$$

$$\mathbf{B} \equiv \begin{bmatrix} \mathbf{B}_I & \mathbf{O}_{32} \\ \mathbf{O}_{32} & \mathbf{B}_{II} \end{bmatrix} \in \mathbb{R}^{6 \times 4} \quad (26c)$$

with  $\mathbf{O}_{32}$  being the  $(3 \times 2)$  zero matrix. Notice that the kinematic model (25) is *redundant*, for it entails six equations for four independent variables. Redundancy is introduced here to add *robustness* to the model. Robustness is needed to avoid *formulation singularities* (??, ang).

### 3.2.2 Singularity Analysis

The SMG meets a singular configuration whenever the  $6 \times 4$  matrices  $\mathbf{A}$  or  $\mathbf{B}$  are rank-deficient. There are two types of singularities, namely, the *serial* singularities, and the *parallel* singularities. The former occurs when  $\mathbf{B}$  is rank-deficient. In the presence of these singularities, there is a direction along which no Cartesian velocity can be produced. From eq.(26c),  $\mathbf{B}$  is rank-deficient when either  $\mathbf{B}_I$  or  $\mathbf{B}_{II}$  are rank-deficient. As a matter of fact,  $\mathbf{B}_J$  loses rank if and only if

$$\mathbf{v}_J \parallel \mathbf{f}_J \quad (27a)$$

or

$$\Delta_J = 0 \quad (27b)$$

From eq.(17),  $\mathbf{v}_J$  lies the plane spanned by vectors  $\mathbf{k}$  and  $\boldsymbol{\rho}_{J1}$ , which is perpendicular to  $\mathbf{f}_J$ . Therefore, eq.(27a) holds if and only if

$$[\mathbf{f}_J, \boldsymbol{\rho}_{J3}, \boldsymbol{\rho}_{J1}] = 0 \quad (28a)$$

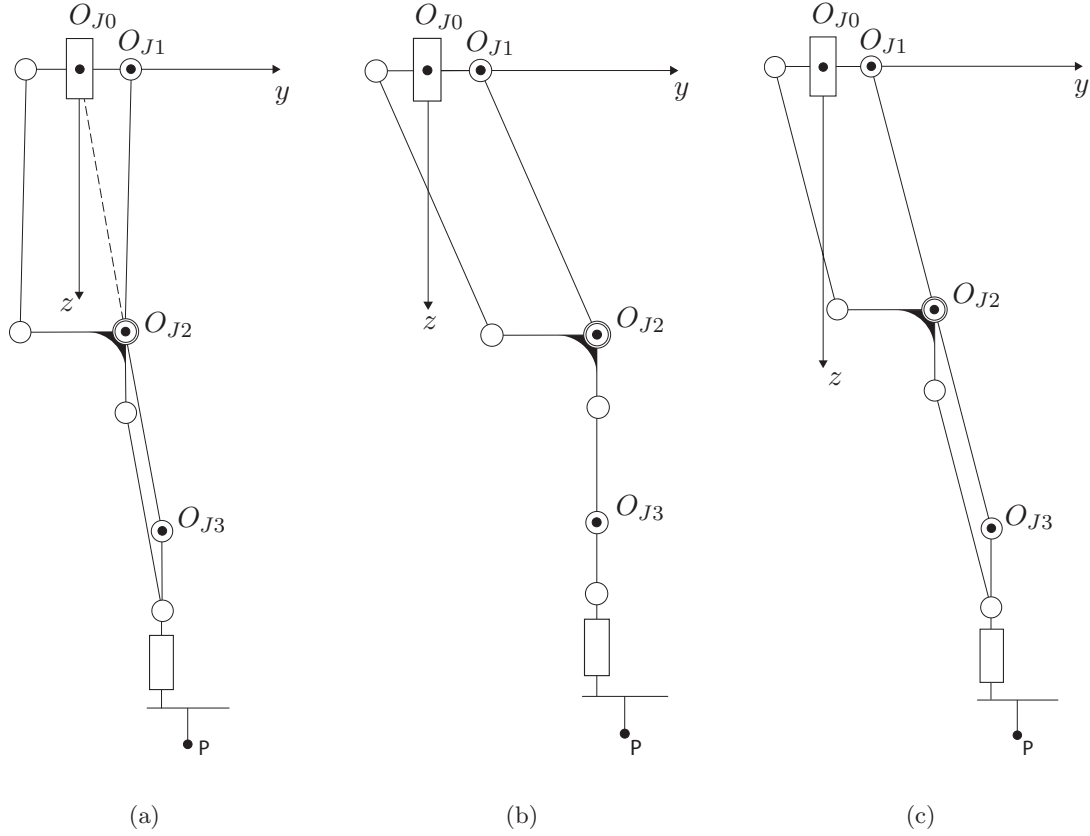


Figure 16: Three serial singular configurations

and

$$[\mathbf{f}_J, \boldsymbol{\rho}_{J3}, \mathbf{k}] = 0 \quad (28b)$$

On the one hand, eq.(28a) holds if  $\boldsymbol{\rho}_{J3}$  is parallel to  $\boldsymbol{\rho}_{J1}$ , i.e., if leg  $J$  is fully extended or fully retracted as depicted in Fig. 16(a). On the other hand, eq.(28b) holds if  $\boldsymbol{\rho}_{J3} \parallel \mathbf{k}$ , i.e., if the distal link of leg  $J$  is vertical as depicted in Fig. 16(b).

Moreover, from eq.(18), eq.(27b) holds if and only if  $\boldsymbol{\rho}_{J2}$  is parallel to  $\boldsymbol{\rho}_{J3}$ , i.e., leg  $J$  is fully extended, as illustrated in Fig. 16(c).

*Parallel* singularities, in turn, occur when  $\mathbf{A}$  is rank-deficient. In the presence of these singularities, it is possible to move locally the operation point  $P$  with the actuators locked, the system thus resulting not in an isostatic structure, which should be the case, but in a mechanism, which cannot resist arbitrary loads, thereby losing control. To avoid any performance deterioration, it is necessary to have a Cartesian workspace free of parallel singularities.

From eq.(26b),  $\mathbf{A}$  loses rank if and only if its four columns are linearly dependent. From eq.(24) this happens when the nullspace of  $\Phi_I$ ,  $\mathcal{N}(\Phi_I)$ , is linearly dependent with the nullspace of  $\Phi_{II}$ ,  $\mathcal{N}(\Phi_{II})$ , i.e., when

$$\phi_I = \pm \phi_{II} \quad (29)$$

From eq.(24e), eq.(29) is equivalent to

$$\mathbf{f}_I \times \boldsymbol{\rho}_{I3} = \pm \mathbf{f}_{II} \times \boldsymbol{\rho}_{II3} \quad (30)$$

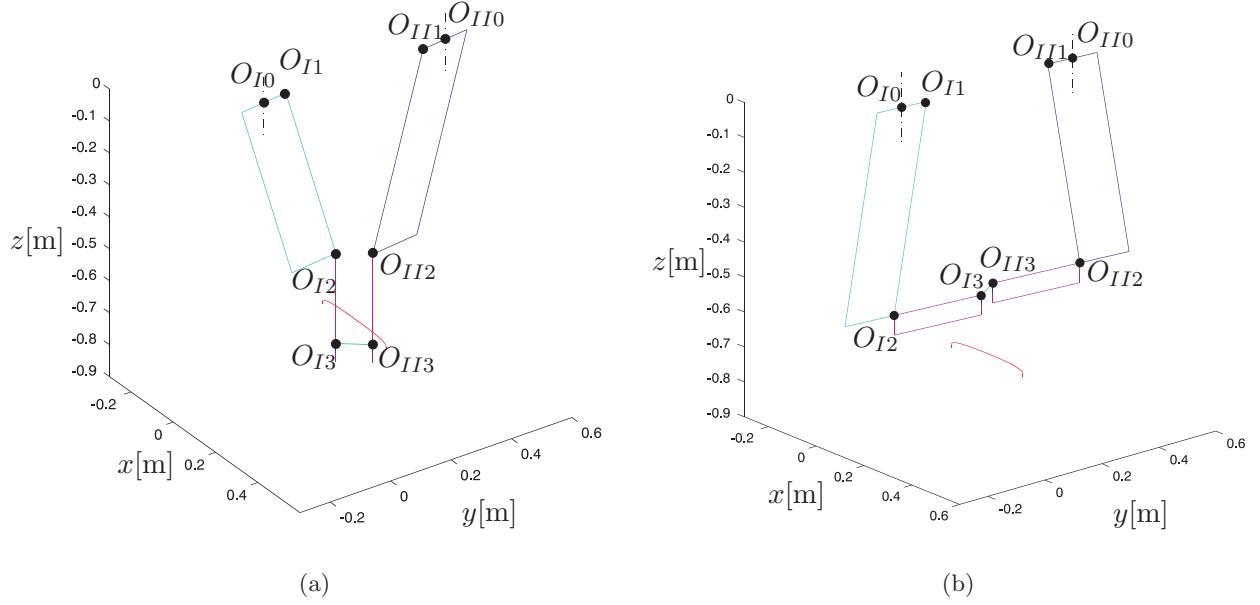


Figure 17: Two parallel singular configurations

In the case where the planes containing legs  $I$  and  $II$  are parallel to each other, i.e.,  $\mathbf{f}_I = -\mathbf{f}_{II}$ , eq.(30) holds if

$$\boldsymbol{\rho}_{I3} = \pm \boldsymbol{\rho}_{II3} \quad (31)$$

i.e., when the distal links of legs  $I$  and  $II$  are vertical or horizontal, as illustrated in Figs. 17(a) and 17(b), respectively.

### 3.3 Dynamics of the SMG

As the mass of the  $II$  joints is one to two orders of magnitude smaller than that of the links, it is assumed negligible in our model. Hence, the mathematical model sought is a system of four second-order differential equations (ODEs), of the form

$$\mathbf{I}(\boldsymbol{\theta})\ddot{\boldsymbol{\theta}} + \mathbf{C}(\boldsymbol{\theta}, \dot{\boldsymbol{\theta}})\dot{\boldsymbol{\theta}} = \boldsymbol{\tau} + \boldsymbol{\gamma} - \boldsymbol{\delta} \quad (32)$$

where  $\boldsymbol{\theta}$  is the four-dimensional vector of actuated joint variables, its first- and second- order time-rates of change being the vectors of actuated-joint velocities and accelerations, respectively, i.e.,

$$\boldsymbol{\theta} = \begin{bmatrix} \theta_{I1} \\ \theta_{I2} \\ \theta_{II1} \\ \theta_{II2} \end{bmatrix}, \quad \dot{\boldsymbol{\theta}} = \begin{bmatrix} \dot{\theta}_{I1} \\ \dot{\theta}_{I2} \\ \dot{\theta}_{II1} \\ \dot{\theta}_{II2} \end{bmatrix}, \quad \ddot{\boldsymbol{\theta}} = \begin{bmatrix} \ddot{\theta}_{I1} \\ \ddot{\theta}_{I2} \\ \ddot{\theta}_{II1} \\ \ddot{\theta}_{II2} \end{bmatrix} \quad (33)$$

Moreover,

$\boldsymbol{\tau}$  is the four-dimensional vector of actuated joint torques;

$\boldsymbol{\gamma}$  is the four-dimensional vector of gravity forces;

$\boldsymbol{\delta}$  is the four-dimensional vector of dissipative forces;

$\mathbf{I}(\boldsymbol{\theta})$  is the  $4 \times 4$  inertia matrix of the SMG, including the drive units;

$\mathbf{C}(\boldsymbol{\theta}, \dot{\boldsymbol{\theta}})$  is the  $4 \times 4$  matrix of Coriolis and centrifugal forces of the SMG, including the drive units.

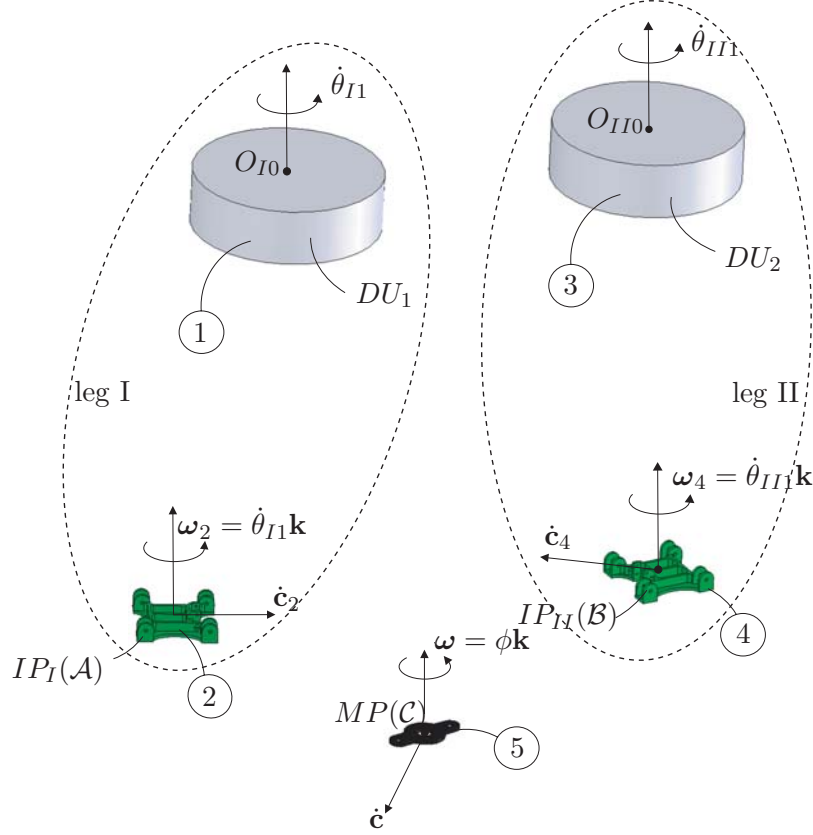


Figure 18: SMG  $\Leftrightarrow$  system of rigid bodies coupled by massless joints

We use throughout the Natural Orthogonal Complement (NOC) to derive the model. The key issue lies in deriving the  $\mathbf{I}(\boldsymbol{\theta})$  and  $\mathbf{C}(\boldsymbol{\theta}, \dot{\boldsymbol{\theta}})$  matrices. As a matter of fact, we have a system of rigid bodies coupled by massless joints, as depicted in Fig. 18, where  $MP$  is the moving platform,  $IP_I$  and  $IP_{II}$  are the intermediate platforms of legs I and II, and  $DU_I$  and  $DU_{II}$  are the drive units of legs I and II.

All five bodies move with displacements belonging to the Schönflies subgroup with rotations about a vertical axis.  $DU_I$  and  $DU_{II}$  undergo pure rotations of rates  $\dot{\theta}_{I1}$  and  $\dot{\theta}_{II1}$ , respectively, about vertical axes.  $IP_I$  and  $IP_{II}$  undergo translations on the surfaces of identical spheres of centres  $O_{I0}$  and  $O_{II0}$  and radius  $l_1$ , where  $l_1$  is the length of the links of the II joints, plus rotations about a vertical axis identical to those of their respective drive units. Therefore,  $MP$  undergoes full Schönflies motions with rotations about a vertical axis.

As the dynamics of the drive units needs a special treatment, we will first study the dynamics of the parallel SMG, and then the dynamics of the drive units. Besides, for conciseness,  $IP_I$ ,  $IP_{II}$ , and  $MP$  are called  $\mathcal{A}$ ,  $\mathcal{B}$ , and  $\mathcal{C}$ , respectively.

### 3.3.1 Inverse Dynamics of the parallel SMG

In this part, we consider bodies  $\mathcal{A}$ ,  $\mathcal{B}$ , and  $\mathcal{C}$  to obtain *tilt* and *pan* torques needed to drive the SMG as specified by  $\boldsymbol{\theta}$ ,  $\dot{\boldsymbol{\theta}}$ , and  $\ddot{\boldsymbol{\theta}}$ .

The trajectory to be followed by the end-effector is completely defined with:

$x(t), y(t), z(t)$ : the Cartesian coordinates of path  $\mathcal{P}$ , expressed in the base coordinate frame  $(O_{I0}, \mathbf{i}, \mathbf{j}, \mathbf{k})$  as functions of time;

$\phi(t)$ : the orientation of the end-effector as a function of time;

$\mathbf{t}_{\mathcal{P}} = [\dot{\phi}(t), \dot{x}(t), \dot{y}(t), \dot{z}(t)]^T$ : the four-dimensional twist of the end-effector along  $\mathcal{P}$ .

$\dot{\mathbf{t}}_{\mathcal{P}} = [\ddot{\phi}(t), \ddot{x}(t), \ddot{y}(t), \ddot{z}(t)]^T$ : the four-dimensional twist-rate of change of the end-effector along  $\mathcal{P}$ .

Let  $\mathbf{t}_{\mathcal{A}}$ ,  $\mathbf{t}_{\mathcal{B}}$ , and  $\mathbf{t}_{\mathcal{C}}$  be the twists of bodies  $\mathcal{A}$ ,  $\mathcal{B}$ , and  $\mathcal{C}$ , respectively, i.e.,

$$\mathbf{t}_{\mathcal{A}} = [\mathbf{T}_{\mathcal{A}42} \mathbf{O}_{42}] \dot{\boldsymbol{\theta}} = \mathbf{T}_{\mathcal{A}} \dot{\boldsymbol{\theta}} \quad (34a)$$

$$\mathbf{t}_{\mathcal{B}} = [\mathbf{O}_{42} \mathbf{T}_{\mathcal{B}42}] \dot{\boldsymbol{\theta}} = \mathbf{T}_{\mathcal{B}} \dot{\boldsymbol{\theta}} \quad (34b)$$

$$\mathbf{t}_{\mathcal{C}} = \mathbf{t}_{\mathcal{P}} = \mathbf{T}_{\mathcal{C}} \dot{\boldsymbol{\theta}} \quad (34c)$$

where

$\mathbf{T}_{\mathcal{A}42}$  is the  $4 \times 2$  *twist shaping matrix* of body  $\mathcal{A}$ , which depends only on variables  $\theta_{I1}$  and  $\theta_{I2}$ :

$$\mathbf{T}_{\mathcal{A}42} = \begin{bmatrix} 1 & 0 \\ -l_2 c_{I1} c_{I2} & l_2 s_{I1} s_{I2} \\ -l_2 s_{I1} c_{I2} & -l_2 c_{I1} s_{I2} \\ 0 & l_2 c_{I2} \end{bmatrix} \quad (35)$$

$\mathbf{T}_{\mathcal{B}42}$  is the  $4 \times 2$  *twist shaping matrix* of body  $\mathcal{B}$ , which depends only on variables  $\theta_{II1}$  and  $\theta_{II2}$ :

$$\mathbf{T}_{\mathcal{B}42} = \begin{bmatrix} 1 & 0 \\ -l_2 c_{II1} c_{II2} & l_2 s_{II1} s_{II2} \\ -l_2 s_{II1} c_{II2} & -l_2 c_{II1} s_{II2} \\ 0 & l_2 c_{II2} \end{bmatrix} \quad (36)$$

$\mathbf{T}_{\mathcal{C}}$  is the  $4 \times 4$  *twist shaping matrix* of body  $\mathcal{C}$ , which is the Jacobian matrix of the manipulator:

$$\mathbf{T}_{\mathcal{C}} = \mathbf{J}_{SMG} = \mathbf{A}^{-1} \mathbf{B} \quad (37)$$

$\mathbf{O}_{42}$  is the  $4 \times 2$  zero matrix.

Furthermore, the time-rate of change of the twist-shaping matrix of body  $\mathcal{A}$  can be readily evaluated as we know  $\theta_{I1}$ ,  $\theta_{I2}$ ,  $\dot{\theta}_{I1}$ , and  $\dot{\theta}_{I2}$  from Subsection 3.1.2, and hence,

$$\dot{\mathbf{T}}_{\mathcal{A}} = \frac{\partial \mathbf{T}_{\mathcal{A}}}{\partial \boldsymbol{\theta}_I} \dot{\boldsymbol{\theta}}_I \quad (38a)$$

where  $\boldsymbol{\theta}_I = [\theta_{I1}, \theta_{I2}]^T$ . Likewise, the time-rate of change of the twist-shaping matrix of body  $\mathcal{B}$  can be readily evaluated, as we know  $\theta_{II1}$ ,  $\theta_{II2}$ ,  $\dot{\theta}_{II1}$ , and  $\dot{\theta}_{II2}$

$$\dot{\mathbf{T}}_{\mathcal{B}} = \frac{\partial \mathbf{T}_{\mathcal{B}}}{\partial \boldsymbol{\theta}_{II}} \dot{\boldsymbol{\theta}}_{II} \quad (38b)$$

with a similar definition for  $\boldsymbol{\theta}_{II}$ . Finally, by differentiating eq.(34c), we obtain

$$\dot{\mathbf{T}}_{\mathcal{C}} \dot{\boldsymbol{\theta}} = \dot{\mathbf{t}}_{\mathcal{C}} - \mathbf{T}_{\mathcal{C}} \ddot{\boldsymbol{\theta}} \quad (38c)$$

which can be readily evaluated since  $\dot{\mathbf{t}}_{\mathcal{C}}$ ,  $\mathbf{T}_{\mathcal{C}}$ , and  $\ddot{\boldsymbol{\theta}}$  are known.

From eq.(32) we can write the equations of motion of the SMG:

$$\mathbf{I}_{SMG}(\boldsymbol{\theta}) \ddot{\boldsymbol{\theta}} + \mathbf{C}_{SMG}(\boldsymbol{\theta}, \dot{\boldsymbol{\theta}}) \dot{\boldsymbol{\theta}} = \boldsymbol{\tau} + \boldsymbol{\gamma}_{SMG} - \boldsymbol{\delta}_{SMG} \quad (39)$$

where

$\mathbf{I}_{SMG}$  is the  $4 \times 4$  inertia matrix of the SMG;

$\mathbf{C}_{SMG}$  is the  $4 \times 4$  matrix of Coriolis and centrifugal forces of the SMG;

$\boldsymbol{\theta}$  is the four-dimensional vector of actuated-joint variables;

$\boldsymbol{\tau}$  is the four-dimensional vector of actuated-joint torques;

$\boldsymbol{\gamma}_{SMG}$  is the four-dimensional vector of gravity forces of the SMG;

$\boldsymbol{\delta}$  is the four-dimensional vector of dissipative forces, which are neglected.

As a matter of fact, the  $4 \times 4$  inertia matrix  $\mathbf{I}_{SMG}$  of the SMG is the sum of the inertia matrices of bodies  $\mathcal{A}$ ,  $\mathcal{B}$ , and  $\mathcal{C}$ , respectively.

$$\mathbf{I}_{SMG} = \mathbf{I}_{\mathcal{A}} + \mathbf{I}_{\mathcal{B}} + \mathbf{I}_{\mathcal{C}} \quad (40a)$$

where

$$\mathbf{I}_{\mathcal{A}} = \mathbf{T}_{\mathcal{A}}^T \mathbf{M}_{\mathcal{A}} \mathbf{T}_{\mathcal{A}} \quad (40b)$$

$$\mathbf{I}_{\mathcal{B}} = \mathbf{T}_{\mathcal{B}}^T \mathbf{M}_{\mathcal{B}} \mathbf{T}_{\mathcal{B}} \quad (40c)$$

$$\mathbf{I}_{\mathcal{C}} = \mathbf{T}_{\mathcal{C}}^T \mathbf{M}_{\mathcal{C}} \mathbf{T}_{\mathcal{C}} \quad (40d)$$

with

$\mathbf{T}_i$  the  $4 \times 4$  twist-shaping matrix of body  $i$  for  $i = \mathcal{A}, \mathcal{B}, \mathcal{C}$ ;

$\mathbf{M}_i$  the  $4 \times 4$  mass dyad of body  $i$ , namely,

$$\mathbf{M}_i = \begin{bmatrix} I_i & \mathbf{0}_3^T \\ \mathbf{0}_3 & m_i \mathbf{1} \end{bmatrix}, \quad i = \mathcal{A}, \mathcal{B}, \mathcal{C} \quad (41)$$

$I_i$  is the ‘‘polar’’ moment of inertia of body  $i$  about its mass centre;

$m_i$  is the mass of body  $i$ ;

$\mathbf{0}_3$  is the 3-dimensional zero vector;

$\mathbf{1}$  is the  $3 \times 3$  identity matrix.

Likewise, the  $4 \times 4$  matrix of Coriolis and centrifugal forces of the SMG model can be derived from:

$$\mathbf{C}_{SMG}(\boldsymbol{\theta}, \dot{\boldsymbol{\theta}}) = \sum_{i=\mathcal{A}, \mathcal{B}, \mathcal{C}} \mathbf{C}_i(\boldsymbol{\theta}, \dot{\boldsymbol{\theta}}) \quad (42a)$$

where the general expression of  $\mathbf{C}_i(\boldsymbol{\theta}, \dot{\boldsymbol{\theta}})$ , as pertaining to body  $i$ , is defined as:

$$\mathbf{C}_i(\boldsymbol{\theta}, \dot{\boldsymbol{\theta}}) = \mathbf{T}_i^T (\mathbf{W}_i \mathbf{M}_i \mathbf{T}_i + \mathbf{M}_i \dot{\mathbf{T}}_i), \quad i = \mathcal{A}, \mathcal{B}, \mathcal{C} \quad (42b)$$

As bodies  $\mathcal{A}$ ,  $\mathcal{B}$ , and  $\mathcal{C}$  undergo Schönflies displacements, we have

$$\mathbf{T}_i^T \mathbf{W}_i \mathbf{M}_i \mathbf{T}_i = \mathbf{O}_{44}, \quad i = \mathcal{A}, \mathcal{B}, \mathcal{C} \quad (43)$$

Therefore, eq.(42b) becomes

$$\mathbf{C}_i(\boldsymbol{\theta}, \dot{\boldsymbol{\theta}}_i) = \mathbf{T}_i^T \mathbf{M}_i \dot{\mathbf{T}}_i, \quad i = \mathcal{A}, \mathcal{B}, \mathcal{C} \quad (44)$$

and the second term of eq.(39) is equal to:

$$\mathbf{C}_{SMG}(\boldsymbol{\theta}, \dot{\boldsymbol{\theta}})\dot{\boldsymbol{\theta}} = \mathbf{T}_A^T \mathbf{M}_A \dot{\mathbf{T}}_A \dot{\boldsymbol{\theta}} + \mathbf{T}_B^T \mathbf{M}_B \dot{\mathbf{T}}_B \dot{\boldsymbol{\theta}} + \mathbf{T}_C^T \mathbf{M}_C \dot{\mathbf{T}}_C \dot{\boldsymbol{\theta}} \quad (45)$$

which can be evaluated by means of eqs.(38a–c) and the  $\dot{\boldsymbol{\theta}}$  values found in Subsection 3.1.2.

Moreover,  $\gamma_{SMG}$  depends on the masses of bodies  $\mathcal{A}$ ,  $\mathcal{B}$ ,  $\mathcal{C}$ , namely,

$$\gamma_{SMG} = \sum_{i=\mathcal{A}, \mathcal{B}, \mathcal{C}} \mathbf{T}_i^T \mathbf{w}_i^G \quad (46a)$$

with

$$\mathbf{w}_i^G = \begin{bmatrix} \mathbf{0}_3 \\ m_i g \end{bmatrix}, \quad i = \mathcal{A}, \mathcal{B}, \mathcal{C} \quad (46b)$$

and  $g$  is the gravity acceleration.

Therefore, the four-dimensional vector  $\boldsymbol{\tau}$  of actuated joint torques is computed from eq.(39). Thus, the torques required from the motors can be evaluated as described in section 3.4.

### 3.4 The Drive Units

The drive units of the robot deserve special attention, as their inertia plays a major role.

Each of the two identical units is to provide two independent motions, pan and tilt of the parallelogram links, and hence, independent rotations, one about a vertical axis, the pan, the other about a horizontal axis, the tilt. We want to produce each of these motions by the concurrent action of the two motors, in order to best distribute the load, and hence, minimize the actuation-sensor complexity.

The drive units of the SMG are based on an innovative drive for the production of pan and tilt motions of a robotic link. The *Pan-Tilt Drive*, as drive units are referred to, is made up of one epicyclic gear train, which is driven by two grounded motors. Besides producing the *pan* motion through the rotation of the planet-carrier, two of their three planets are used to produce the *tilt* motion.

We could therefore use one motor in order to produce the pan motion and another one to produce the tilt motion. However, it is possible to use both motors again to produce the tilt motion. This can be achieved through the use of a differential gear train. As a result, with a suitable design, it is possible to use the full power of both motors for the two independent motions.

#### 3.4.1 Description

Figures 19(a) and 19(b) depict a schematic drawing and a 3D view of one of the two drive units of the manipulator, respectively. The drive units consist of the elements described below:

- The two motors  $M_A$  and  $M_B$ , mounted on a fixed frame (not shown on the figure) and driving gears 1 and 2, respectively, by means of the speed reducers  $SR_1$  and  $SR_2$ ;
- gear 1, meshing with gear 3, while gear 2 meshes with gear 4;
- a epicyclic train driven by the two motors: motor A drives the sun gear 5 while motor B drives the internal ring gear 7, these two gears meshing with the planets 6; when rotating about axis  $\mathcal{A}_1$ , these planets drive a planet carrier 8 rigidly attached to the housing of the whole mechanism and not included in the figures. The planet-carrier 8 produces the pan motion;
- two of the three identical planets, when rotating about their own axes of symmetry, produce the tilt motion;



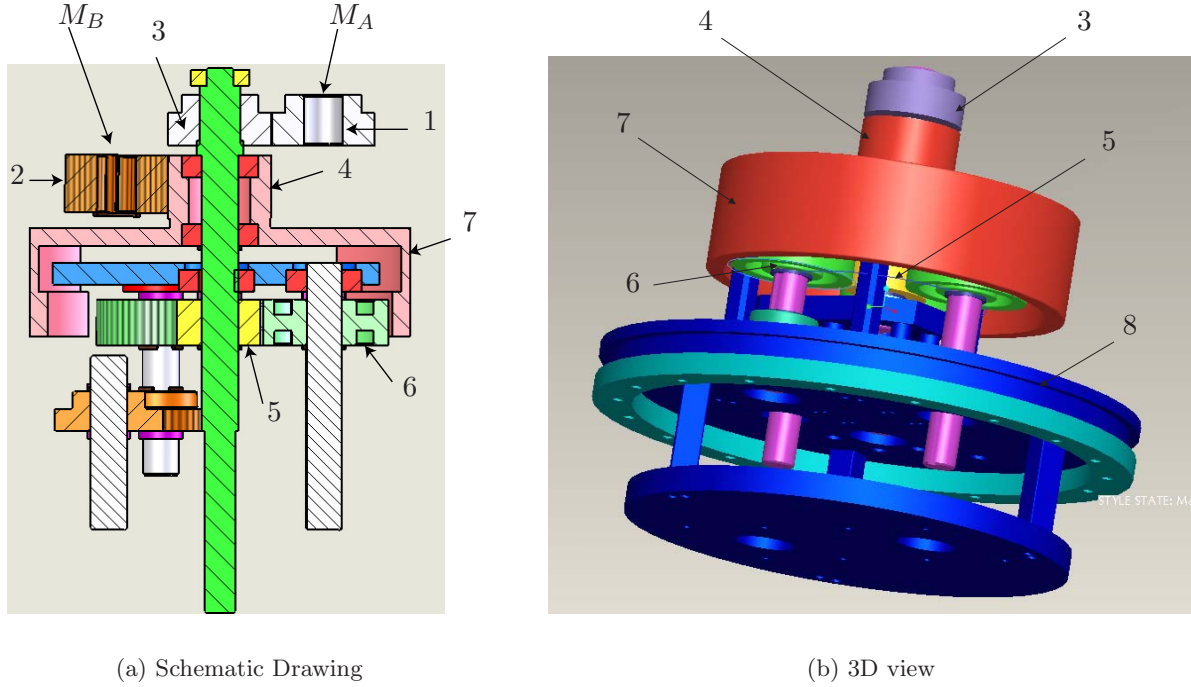


Figure 19: Drive Unit

### 3.4.2 Mechanism Kinematics

The relations among angular velocities are described by means of the notation below:

- $N_i$ , number of teeth of the  $i^{\text{th}}$  gear, for  $i = 1, \dots, 6$
- $r_{3,1} = N_3/N_1 = N_4/N_2$ , the gear ratio between gears 3 and 1, and between gears 4 and 2;
- $r_0$ , the reduction ratio from motor A (B) to gear 1 (2) through the gear head  $GH_1$  ( $GH_2$ );
- $r = r_0 r_{3,1}$ , the total reduction ratio from the motors to the driven sun and ring gears;
- $r_{6,5} = N_6/N_5$ , the gear ratio between the planets 6 and the sun gear 5;
- $\omega_i$ , angular velocity of the corresponding gears, planet-carriers, or motors, for  $i = 1, \dots, 6$ ;
- $\omega_p$ , angular velocity of the pan motion;
- $\omega_t$ , angular velocity of the tilt motion.

**Forward Kinematics.** We obtain here all the necessary relations between meshing gears, starting with the motors and ending with the relative velocity between the planet-carrier and the planets.

From the motors to the driven gears of the epicyclic train,

$$\omega_5 = -\frac{1}{r}\omega_A \quad (47a)$$

$$\omega_7 = -\frac{1}{r}\omega_B \quad (47b)$$

Inside the gear train, we have the well-known relations ([Juvinal and Marshek, 2000](#))

$$\omega_8(N_5 + N_6) - \omega_6 N_6 = \omega_5 N_5 \quad (48a)$$

$$\omega_7(N_5 + 2N_6) = \omega_8(N_5 + N_6) + \omega_6 N_6 \quad (48b)$$

Dividing both sides of the above equations by  $N_5$  and solving for  $\omega_6$  and  $\omega_8$ , we obtain

$$\omega_6 = \frac{1}{2r_{6,5}}[-\omega_5 + (1 + 2r_{6,5})\omega_7] \quad (49a)$$

$$\omega_8 = \frac{1}{2(1 + r_{6,5})}[\omega_5 + (1 + 2r_{6,5})\omega_7] \quad (49b)$$

Substituting eqs.(47a) and (47b) into eqs.(49a) and (49b), while noticing that  $\omega_p = \omega_8$  and  $\omega_t = \omega_6 - \omega_8$  yields

$$\omega_p = -\frac{1}{2r(1 + r_{6,5})}[\omega_A + (1 + 2r_{6,5})\omega_B] \quad (50a)$$

$$\omega_t = \frac{1 + 2r_{6,5}}{2rr_{6,5}(1 + r_{6,5})}(\omega_A - \omega_B) \quad (50b)$$

Let us finally define  $\boldsymbol{\omega}_{in}$  and  $\boldsymbol{\omega}_{out}$  by

$$\boldsymbol{\omega}_{in} = \begin{bmatrix} \omega_A \\ \omega_B \end{bmatrix}, \boldsymbol{\omega}_{out} = \begin{bmatrix} \omega_p \\ \omega_t \end{bmatrix}$$

which are related by the Jacobian  $\mathbf{J}_D$ , namely,

$$\boldsymbol{\omega}_{out} = \mathbf{J}_D \boldsymbol{\omega}_{in} \quad (51a)$$

where  $\mathbf{J}_D$  is defined as:

$$\mathbf{J}_D = \begin{bmatrix} J_{D11} & J_{D12} \\ J_{D21} & J_{D22} \end{bmatrix} \quad (51b)$$

with

$$J_{D11} = \frac{-1}{2r(1 + r_{6,5})} \quad (51c)$$

$$J_{D12} = \frac{-(1 + 2r_{6,5})}{2r(1 + r_{6,5})} \quad (51d)$$

$$J_{D21} = \frac{1 + 2r_{6,5}}{2rr_{6,5}(1 + r_{6,5})} \quad (51e)$$

$$J_{D22} = \frac{-(1 + 2r_{6,5})}{2rr_{6,5}(1 + r_{6,5})} \quad (51f)$$

**Inverse Kinematics.** Regarding the control of the whole robot, a robot gesture is specified, from which the angular velocities of the two motors are required. These are readily obtained from the forward-kinematics relations, derived from eqs.(51a–f).

Matrix  $\mathbf{J}_D$  is invertible, its inverse being

$$\mathbf{J}_D^{-1} = -r \begin{bmatrix} 1 & -r_{6,5} \\ 1 & \frac{r_{6,5}}{1 + 2r_{6,5}} \end{bmatrix} \quad (52)$$

thereby deriving the inverse kinematics of the drive unit, namely,

$$\boldsymbol{\omega}_{in} = \mathbf{J}_D^{-1} \boldsymbol{\omega}_{out} \quad (53)$$

### 3.4.3 Dynamics of the Drive Units

Knowing the four-dimensional vector of actuated joint torques, i.e., the torques applied to the active planets and the planet-carrier of the drive-units, this part aims at studying the dynamics of the drive-units in order to compute the torques required from the motors.

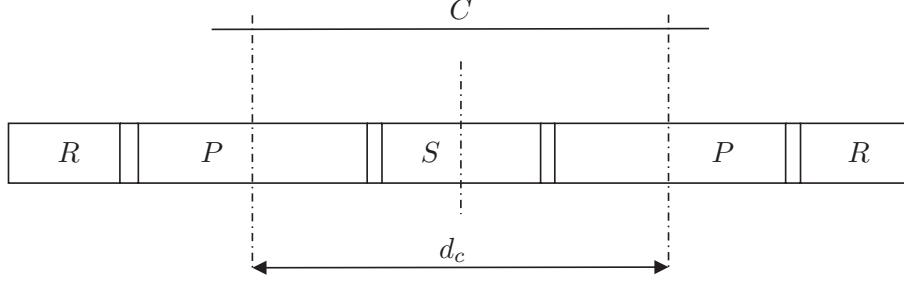


Figure 20: Schematic drawing of the drive-units

Figure 20 depicts a layout of the drive units of the SMG. Each drive unit is composed of a sun  $S$ , three planets  $P$ , a ring gear  $R$ , and a planet carrier  $C$ , whose diameter is  $d_C$ .

Here, we use the Lagrange equations to study the dynamics of the drives. The kinetic energy  $T$  of the drives depends on the inertia properties of their components, and their corresponding velocity.

$$T = \frac{1}{2}I_S\omega_S^2 + \frac{1}{2}I_R\omega_R^2 + \frac{1}{2}I_C\omega_C^2 + \frac{3}{2}I_P\omega_P^2 + \frac{3}{2}m_P\left(\frac{d_C}{2}\omega_C\right)^2 \quad (54)$$

where

$I_S$ ,  $I_P$ ,  $I_R$ , and  $I_C$ , are the “polar” moments of inertia of the sun, the planets, the ring gear, and the carrier, respectively;

$\omega_S$ ,  $\omega_P$ ,  $\omega_R$ , and  $\omega_C$ , are the absolute angular velocities of the sun, the planets, the ring gear, and the carrier, respectively;

$m_P$  is the mass of one planet;

$d_C$  is the diameter of the planet-carrier.

Moreover, as depicted in eq.(51a), the Jacobian matrix  $\mathbf{J}_D$  of the drives allows us to know the relation between their input and their output

$$\begin{bmatrix} \omega_C \\ \bar{\omega}_P \end{bmatrix} = \mathbf{J}_D \begin{bmatrix} \omega_S \\ \omega_R \end{bmatrix} \quad (55a)$$

$\bar{\omega}_P$  being the relative angular velocity of the planets, namely,

$$\omega_P = \bar{\omega}_P + \omega_C \quad (55b)$$

As no part of the drives moves along the  $z$  axis, their potential energy is constant, and the Lagrange equations of the drives become:

$$\frac{d}{dt} \frac{\partial T}{\partial \dot{q}_i} - \frac{\partial T}{\partial q_i} = \tau_{SR} - \mathbf{J}_D^T \tau_{CP}, \quad i = 1, 2 \quad (56a)$$

with

$$\mathbf{q} = [q_1 \ q_2]^T = [\theta_S \ \theta_R]^T \quad (56b)$$

$$\dot{\mathbf{q}} = [\dot{q}_1 \ \dot{q}_2]^T = [\omega_S \ \omega_R]^T \quad (56c)$$

$$\boldsymbol{\tau}_{SR} = [\tau_S \ \tau_R]^T \quad (56d)$$

$$\boldsymbol{\tau}_{CP} = [\tau_C \ \tau_P]^T \quad (56e)$$

where

$\theta_S$  is the angle of rotation of the sun;

$\theta_R$  is the angle of rotation of the ring gear;

$\tau_S$  is the torque applied to their sun;

$\tau_R$  is the torque applied to their ring gear;

$\tau_C$  is the torque applied to their carrier, which is equivalent to the pan torque  $\tau_{Pan}$ ;

$\tau_P$  is the torque applied to their active planets, which is equivalent to the tilt torque  $\tau_{Tilt}$ .

Therefore, from eq.(56a), we obtain the expressions for the torques that have to be applied to the sun and the ring gears of the drives:

$$\boldsymbol{\tau}_{SR} = \mathbf{I}_D \ddot{\mathbf{q}} + \mathbf{J}_D^T \boldsymbol{\tau}_{CP} \quad (57a)$$

with

$$\mathbf{I}_D = \begin{bmatrix} I_{D11} & I_{D12} \\ I_{D21} & I_{D22} \end{bmatrix} \quad (57b)$$

$$I_{D11} = I_S + \left( I_C + \frac{3}{4} m_P d_C^2 + 3I_P \right) J_{D11}^2 + 6I_P J_{D11} J_{D21} + 3I_P J_{D21}^2 \quad (57c)$$

$$I_{D12} = I_{D21} = 3I_P (J_{D11} + J_{D21})(J_{D12} + J_{D22}) + \left( I_C + \frac{3}{4} m_P d_C^2 \right) J_{D11} J_{D12} \quad (57d)$$

$$I_{D22} = I_R + \left( I_C + \frac{3}{4} m_P d_C^2 + 3I_P \right) J_{D12}^2 + 6I_P J_{D12} J_{D22} + 3I_P J_{D22}^2 \quad (57e)$$

$$\ddot{\mathbf{q}} = [\ddot{q}_1 \ \ddot{q}_2]^T = [\gamma_S \ \gamma_R]^T \quad (57f)$$

where

$\gamma_S$  is the angular acceleration of the sun;

$\gamma_R$  is the angular acceleration of the ring gear.

## 3.5 The Right Angle Gear Boxes (RAGB)

### 3.5.1 Description

The Right Angle Gear Boxes are installed between the drives and the II joints of the SMG. Their main function is the generation of Pan and Tilt motions from the relative rotations of the planets and the planet carrier. It turns out that the Jacobian matrix of the system is the  $4 \times 4$  identity matrix. As a matter of fact, the gear ratio of the RAGB is equal to one. The RAGB do not have any effect on the kinematics of the system. However, their dynamics has to be taken into account as these parts are made up of steel.

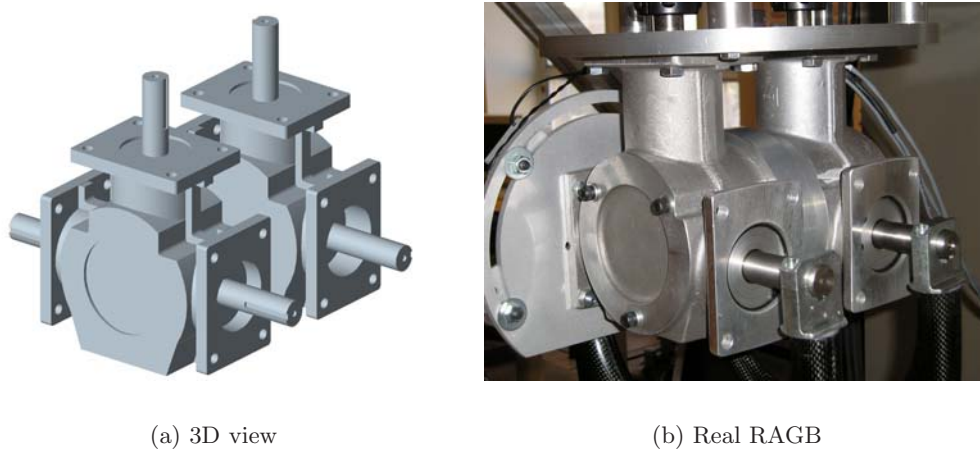


Figure 21: The RAGB of the SMG

### 3.5.2 Dynamics of RAGB

Knowing the Pan and Tilt torques applied to the legs of the SMG, this part aims at studying the dynamics of the RAGB in order to compute the torques required from the Drive Units.

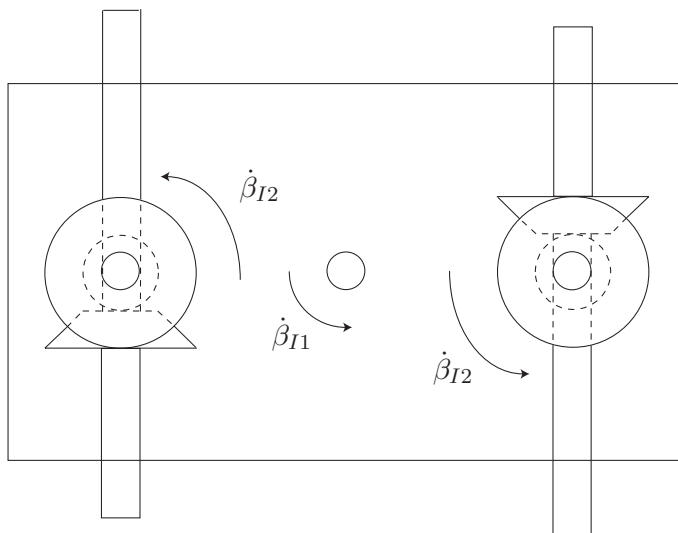


Figure 22: Schematic drawing of RAGB

Figure 22 depicts a layout of the RAGB of the SMG. Each RAGB is composed of a Housing  $H$ , two Vertical Gears *Inputs*, and two Horizontal Gears *Outputs*.

Here, the dynamics of the drives is studied by means of the Lagrange equations. The kinetic energy  $T$  of the RAGB depends on the inertia properties of their components, and their corresponding velocity.

$$T_{input} = 2 \left[ \frac{1}{2} I_{in} (\dot{\beta}_{I1}^2 + \dot{\beta}_{I2}^2) + \frac{1}{2} m_{in} \dot{\mathbf{c}}_{in}^2 \right] \quad (58a)$$

$$T_{output} = 2 \left[ \frac{1}{2} I_{out} \dot{\beta}_{I2}^2 + \frac{1}{2} I_{out} \dot{\beta}_{I1}^2 + \frac{1}{2} m_{out} \dot{\mathbf{c}}_{out}^2 \right] \quad (58b)$$

$$T_I = \frac{1}{2} I_H \dot{\beta}_{I1}^2 + T_{input} + T_{output} \quad (58c)$$

where

$I_H$ ,  $I_{in}$  and  $I_{out}$ , are the ‘‘polar’’ moments of inertia of the Housing, the Vertical Gears, and the Horizontal Gears respectively;

$\dot{\beta}_{I1}$  and  $\dot{\beta}_{I2}$  are the angular velocities of the planet carrier and the planets, respectively, i.e, the Pan and Tilt rates.

$m_{in}$  and  $m_{out}$  are the masses of the vertical and horizontal gears, respectively;

$\dot{\mathbf{c}}_{in}$  and  $\dot{\mathbf{c}}_{out}$  are the velocities of the mass centers of the vertical and horizontal gears :

$$\dot{\mathbf{c}}_{in}^2 = (d_{cin} \dot{\beta}_1)^2 \quad (59a)$$

$$\dot{\mathbf{c}}_{out}^2 = (d_{cout} \dot{\beta}_1)^2 \quad (59b)$$

Likewise, the kinetic energy  $T_{II}$  of the RAGB of the second Leg is expressed with respect to  $\dot{\beta}_{II1}$  and  $\dot{\beta}_{II2}$ .

The Jacobian matrix of the two RAGB,  $\mathbf{J}_{RAGB}$ , is the  $4 \times 4$  identity matrix.

As none part of the RAGB moves along  $z$  axis, their potential energy is null, and the Lagrange equations of the drives are written:

$$\frac{d}{dt} \frac{\partial T}{\partial \dot{\boldsymbol{\beta}}} - \frac{\partial T}{\partial \boldsymbol{\beta}} = \boldsymbol{\tau}_{Drives} - \mathbf{J}_{RAGB}^T \boldsymbol{\tau}_{Pan-Tilt} \quad (60a)$$

with

$$\boldsymbol{\beta} = [\beta_1 \beta_2 \beta_3 \beta_4]^T \quad (60b)$$

$$\boldsymbol{\tau}_{Drives} = [\tau_{C_I} \tau_{P_I} \tau_{C_{II}} \tau_{P_{II}}]^T \quad (60c)$$

$$\boldsymbol{\tau}_{Pan-Tilt} = [\tau_{Pan_I} \tau_{Tilt_I} \tau_{Pan_{II}} \tau_{Tilt_{II}}]^T \quad (60d)$$

where

$\tau_{Pan}$  is the Pan torque applied to SMG;

$\tau_{Tilt}$  is the Tilt torque applied to the SMG;

$\tau_C$  is the torque applied to the carrier;

$\tau_P$  is the torque applied to the active planets.

Therefore, from eq. (60a), we obtain the expressions of the torques, which have to be applied to the RAGB:

$$\boldsymbol{\tau}_{Drives} = \mathbf{I}_{RAGB} \ddot{\boldsymbol{\beta}} + \mathbf{J}_{RAGB}^T \boldsymbol{\tau}_{Pan-Tilt} \quad (61a)$$

where  $\mathbf{I}_{RAGB}$  is the  $4 \times 4$  global inertia matrix of the two RAGB, obtained from eq. (60a).

$$\mathbf{I}_{RAGB} = \begin{bmatrix} \mathbf{I}_{RAGB_I} & \mathbf{O}_{22} \\ \mathbf{O}_{22} & \mathbf{I}_{RAGB_{II}} \end{bmatrix} \quad (61b)$$

## 3.6 Dimensioning

The dynamics of the manipulator is studied with knowledge of the trajectory that its end-effector has to follow. In order to select the motors, the gear heads and the optimum design parameters of the architecture of the manipulator and those of the drive units, we follow the procedure depicted in Fig. 23 and explained in detail in the subsections below.

### 3.6.1 Trajectory-Planning

The SMG is designed for pick-and-place operations based on the path defined to test the performance of SCARA robots, as depicted in Fig. 24. Moreover, the path location is defined with the parameters shown in Fig. 25, where

$\beta$  is the orientation of the trajectory with respect to the normal plane;

$\phi_{factor}$  is the EE rotation sweep coefficient, defined as  $\phi_{factor} = 1 : \text{sweep} = 180^\circ$ ,  $\phi_{factor} = 0.5 : \text{sweep} = 90^\circ$ ;

$\phi_{offset}$  is the orientation offset of the EE at the start point;

offset is the path offset in the radial direction of the path (positive towards leg II).

As a matter of fact, the end-effector has to move from point  $A$  to point  $D$  through points  $B$  and  $C$  with a rotation of  $180^\circ$  and back in less than 500 ms, with a payload of 5.5 kg. Figure 24 depicts the path with the simplest geometry:  $AB$  is pick path,  $BC$  is shift, and  $CD$  is place.

However, this path exhibits some discontinuities at points  $B$  and  $C$  where the end-effector has to decelerate, to rest, and to accelerate again. To overcome this issue, a new path was generated by means of a 4–5–6–7 polynomial distribution in order to obtain continuous curvature distribution (Malik, 2005), as illustrated in Fig. 26. A 4-5-6-7 polynomial (Angeles, 2002) is employed for the displacement programs of the various segments of the trajectory, given in Fig. 24. A characteristic of this polynomial is that it provides zero jerk at the start and the end of the motion, which means that the polynomial is continuous up to the third derivative. The polynomial is reproduced here for quick reference:

$$s(\tau) = -20\tau^7 + 70\tau^6 - 84\tau^5 + 35\tau^4 \quad (62a)$$

$$s'(\tau) = (1/T)(-140\tau^6 + 420\tau^5 - 420\tau^4 + 140\tau^3) \quad (62b)$$

$$s''(\tau) = (1/T^2)(-840\tau^5 + 2100\tau^4 - 1680\tau^3 + 420\tau^2) \quad (62c)$$

$$\tau = \frac{t}{T} \quad (62d)$$

where  $s(\tau)$  is a non-dimensional displacement function, with  $\tau$  as a non-dimensional time parameter,  $t$  is time and  $T$  is time elapsed between the ends of the trajectory. Here,  $s'(\tau)$  and  $s''(\tau)$  are the first two derivatives of  $s(\tau)$  with respect to  $\tau$ .

To produce an actual displacement program for this non-dimensional function, we need initial and final displacement conditions. Here, we need only the initial orientation and position of the EE at point  $A$ , the final position then being an outcome of the path geometry itself. Determining the initial pose of the EE depends on the path placement inside the workspace of the manipulator, which insures that the EE moves through this path without hitting a singularity.

This displacement program is applied to a total EE rotation of  $135^\circ$  because a rotation of  $180^\circ$  is impossible to reach with a parallel architecture. Likewise, for the trajectory placement in the pan plane, the manipulator becomes singular if the end-effector orientation  $\phi$  is equal to  $90^\circ$  or  $270^\circ$ , with point  $P$  of the EE anywhere along the pan-normal axis. For maximum dexterity (lowest condition number of the forward Jacobian), a mid-range motion is chosen, which prevents the robot from going through

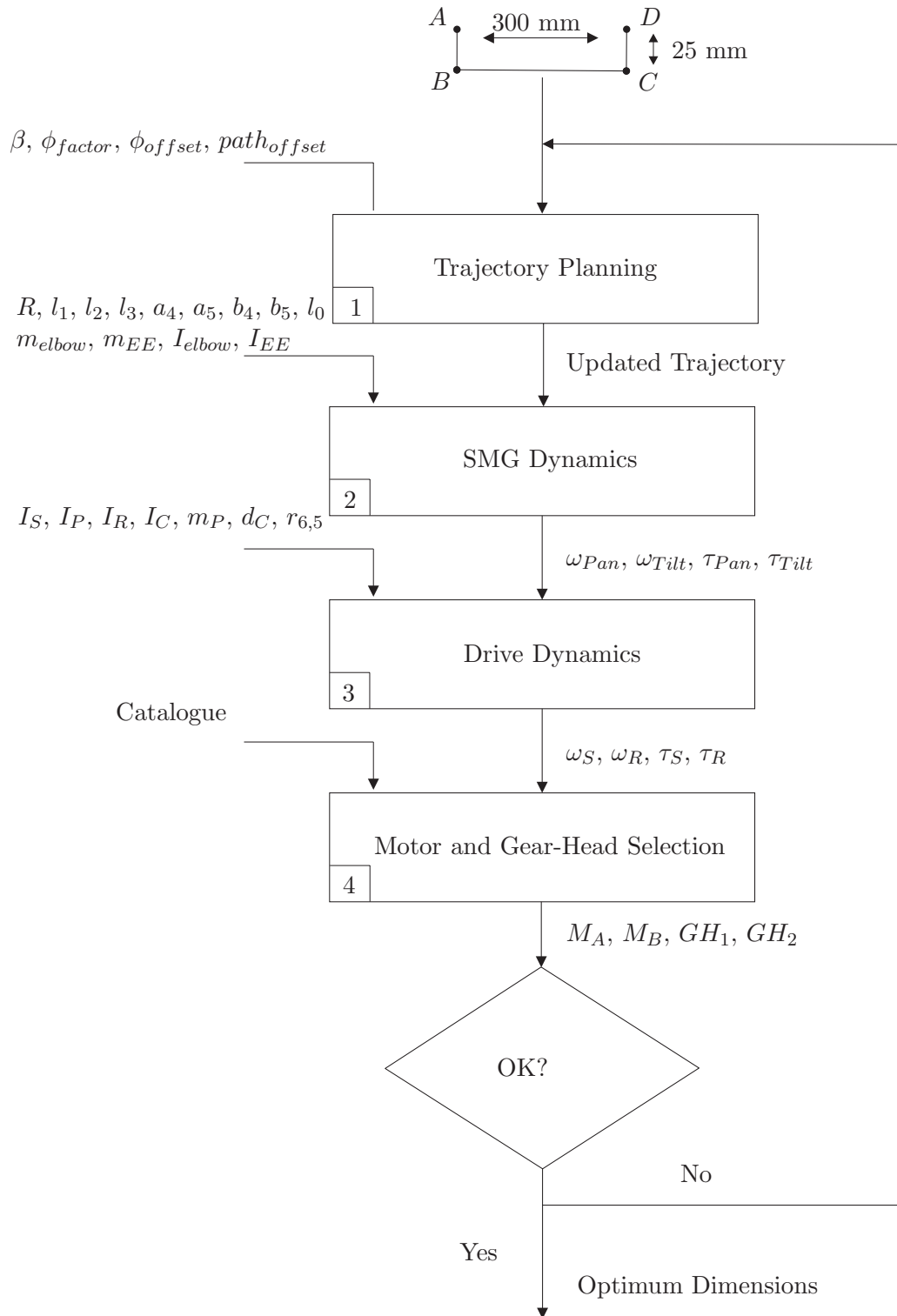


Figure 23: SMG dimensioning procedure

singularities. Thus, the path depicted in Fig. 26 is shaped by plotting the  $Y$  and  $Z$  paths generated by the 4-5-6-7 polynomial.



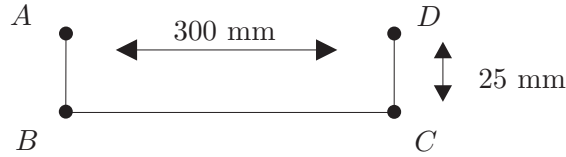


Figure 24: Path adopted for the manipulator design

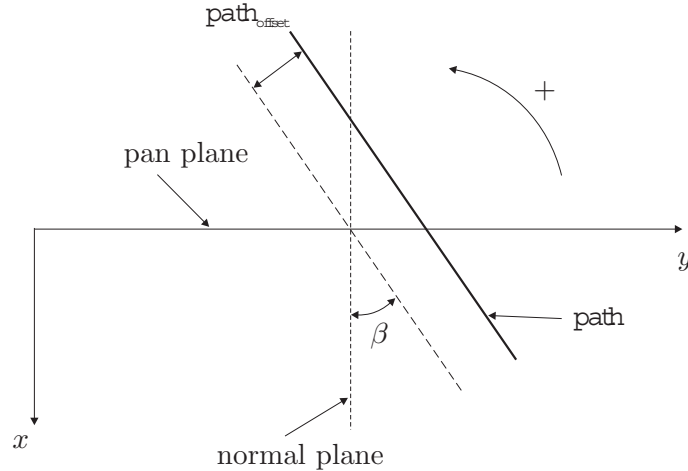


Figure 25: Path location

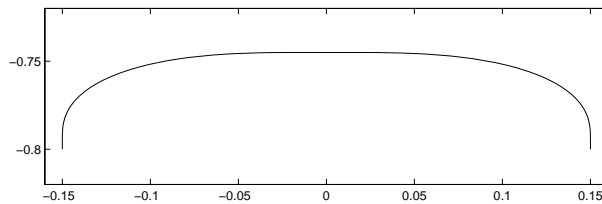


Figure 26: Path generated using a 4-5-6-7 polynomial displacement program

In the  $Y$ -direction, however, the 4-5-6-7 polynomial distribution starts after the retract ( $A_s B_s$ ) segment (pure vertical pick manoeuvre, described by let say the length of pins of IC to be picked to be cleared from its pallet) is covered by the end-effector and ends before start of insertion ( $D_s E_s$ ) segment (pure vertical place manoeuvre, to fix the IC in its position of circuit board). For simplicity, these distances are equal to each other and are of 5 mm height out of total vertical motion of 25 mm.

Figure 27 shows the displacement program for either  $X$  or  $Y$  direction based on whether the path is placed in the pan or in the normal plane, respectively. All the plots, except for the half the path plot are vs. time, with time step of 0.0001 sec (one tenth of a millisecond), called resolution. Also, from this plot, we see that the EE has zero velocity in the  $X$  and  $Y$  directions at the start and at the end of the half cycle (pick and place) for some time. It is equal to the time for which the EE takes to reach the height of 5 mm (retract segment, or insertion segment), with respect to 4-5-6-7 polynomial distribution in  $Z$  direction. Figure 28 shows the displacement program in the  $Z$  coordinate, where the EE goes up (in the negative direction of the  $Z$  axis) and comes down (in the positive direction of the  $Z$  axis).

Figure 29 shows the displacement program for the orientation of the EE, in which it is also obvious that the EE starts to change its orientation after retracts and ends before insertion. It is obvious from all the three figures of displacement programs that the initial conditions for the velocities in  $X$  or  $Y$  (depends on whether the path is in the pan plane ( $\beta = 0^\circ$ ) or the normal plane ( $\beta = 90^\circ$ ), respectively),  $Z$  and  $\phi$

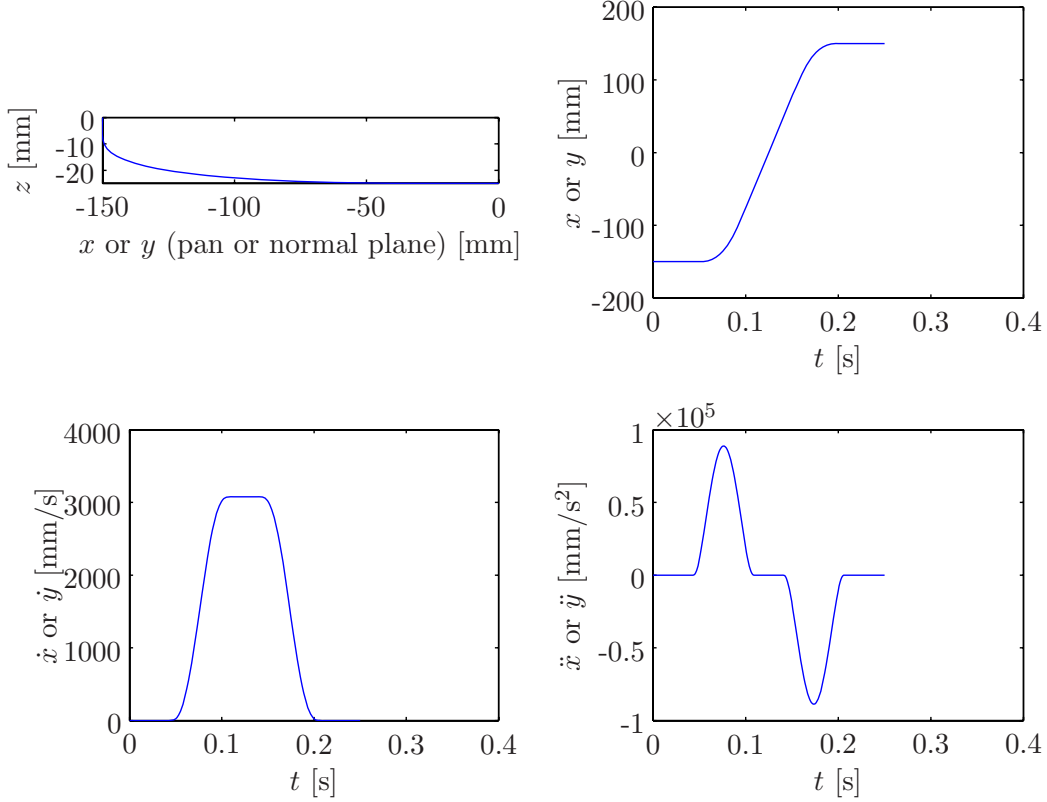


Figure 27: Displacement program in the  $X$  or  $Y$  directions

coordinates  $P$  are zero. Finally, Table 2 sums up the optimum values of the trajectory parameters.

Table 2: Trajectory parameters

$\beta$ [deg]	$\phi_{factor}$	$\phi_{offset}$ [deg]	$path_{offset}$ [m]
0	0.75	0	0

In parallel robots, every point of the positioning workspace involves a singularity, which is reached upon giving a specific orientation to the EE about that point.

### 3.6.2 SMG Dynamics

After some iterations of the dimensioning procedure displayed in Fig. 23, we found the optimum values of the parameters of the SMG architecture that are recorded in Tables 3 and 4.

Table 3: Optimum manipulator parameters

$l_1$ [mm]	$l_2$ [mm]	$l_3$ [mm]	$a_4$ [mm]	$b_4$ [mm]	$a_5$ [mm]	$b_5$ [mm]	$R$ [mm]	$l_0$ [mm]
80	600	300	0	0	50	0	50	600

With knowledge of the trajectory to be followed by the EE, the dimensions and the inertia properties of the manipulator, the velocities and the torques required at the output of the drive units can be computed. On the one hand, the pan and tilt rates of each leg are computed from eq.(??) and are illustrated in Figs. 30(a)—(b), where  $\omega_{panI} = \dot{\theta}_{I1}$ ,  $\omega_{panII} = \dot{\theta}_{II1}$ ,  $\omega_{tiltI} = \dot{\theta}_{I2}$ , and  $\omega_{tiltII} = \dot{\theta}_{II2}$ . On the

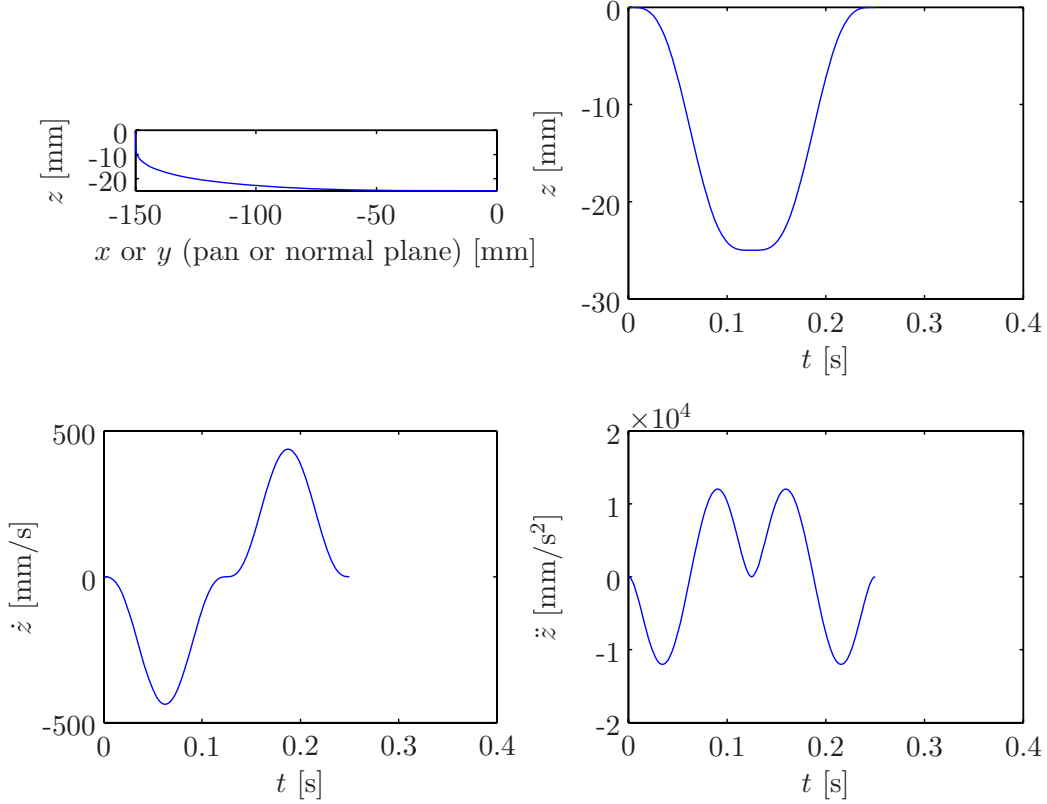


Figure 28: Displacement program in the  $Z$  direction

Table 4: Inertia properties of the manipulator

$m_{elbow}$ [kg]	$m_{EE}$ [kg]	$I_{elbow}$ [kgm <sup>2</sup> ]	$I_{EE}$ [kgm <sup>2</sup> ]	$gravity$ [ms <sup>-2</sup> ]
0.588	2.5	$4.054 \cdot 10^{-4}$	$\frac{1}{2}m_{EE} \times 0.025^2$	9.806

other hand, the pan and tilt torques are computed by means of eq.(39), as illustrated in Figs. 31(a)—(b).

Moreover, Figs. 32(a) and 32(b) show that the manipulator does not meet any singularity when the EE follows the path depicted in Fig. 26. Indeed, the inverse condition numbers of  $\mathbf{A}$  and  $\mathbf{B}$ , i.e.  $\kappa^{-1}(\mathbf{A})$  and  $\kappa^{-1}(\mathbf{B})$ , never vanish when the EE follows this path.

### 3.6.3 Drive Dynamics

With knowledge of the drive-unit parameters and the rates and torques at their output, i.e.  $\omega_{panI}$ ,  $\omega_{panII}$ ,  $\omega_{tiltI}$ ,  $\omega_{tiltII}$ ,  $\tau_{panI}$ ,  $\tau_{panII}$ ,  $\tau_{tiltI}$ , and  $\tau_{tiltII}$ , the rates and torques required at their input can be computed from eq.(57a).

Table 5: Drive unit parameters

$I_{sun}$ [kgm <sup>2</sup> ]	$I_{planet}$ [kgm <sup>2</sup> ]	$I_{ring}$ [kgm <sup>2</sup> ]	$I_{carrier}$ [kgm <sup>2</sup> ]	$m_{planet}$ [kg]	$\mathcal{O}_{PC}$ [m]	$r_{6,5}$
$4.921 \cdot 10^{-4}$	$9.852 \cdot 10^{-3}$	$5.146 \cdot 10^{-2}$	$3.42 \cdot 10^{-2}$	4.777	0.186	1.5

Consequently, Table 5 depicts the optimum drive-unit parameters, while Figs. 33(a)—(b) and 34(a)—(b) illustrate the rates and torques to be applied to the sun and ring gears of the drive units.

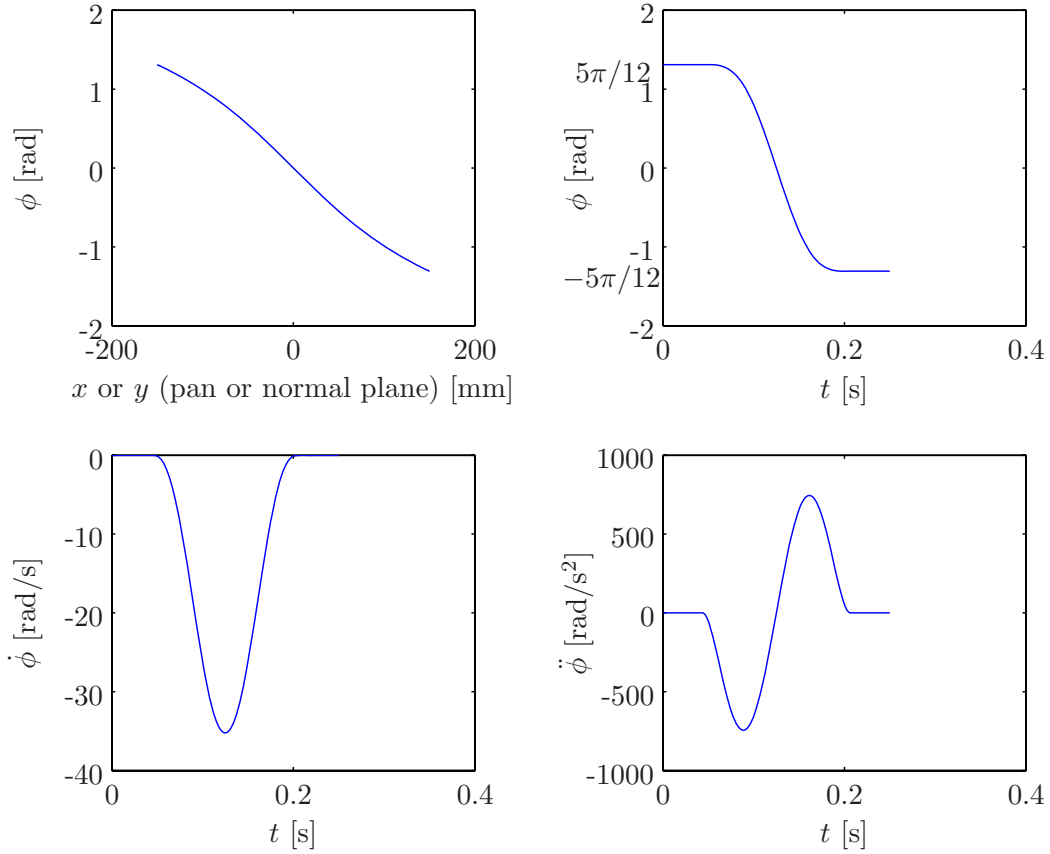
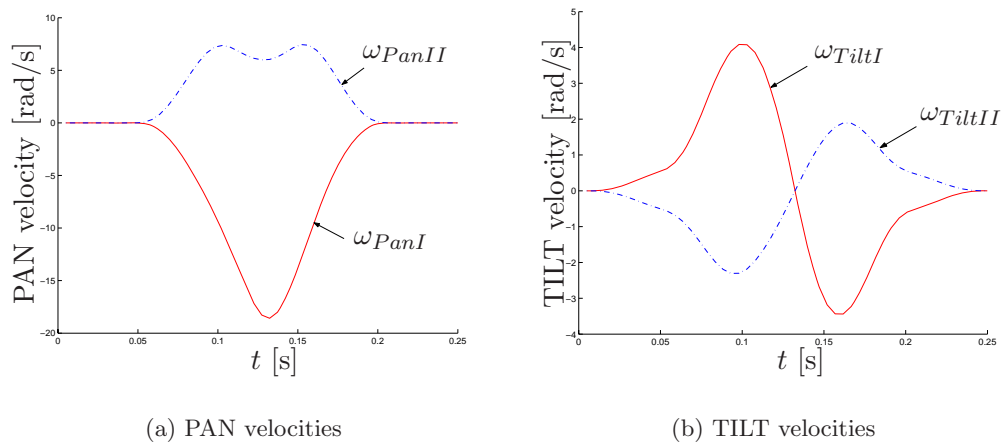


Figure 29: Displacement program for the EE orientation

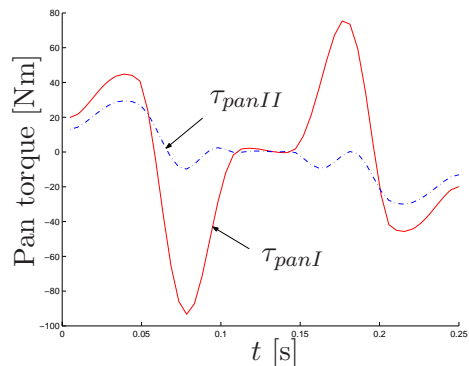


(a) PAN velocities

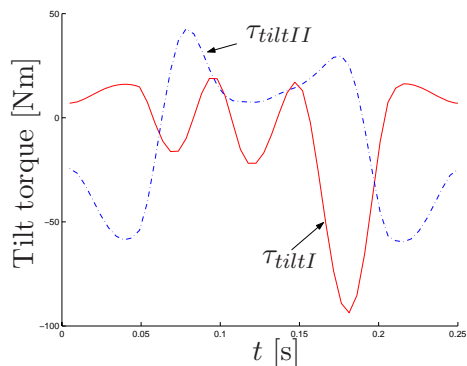
(b) TILT velocities

Figure 30: Actuated joint velocities

Besides, the gear ratio between the planets and the sun gear of the drive units is equal to 1.5 in order to minimize the condition number of  $\mathbf{J}_D$  defined in eq.(51b) and plotted in Fig. 35, and to avoid harmonics, which appear when  $r_{6,5}$  is an integer.

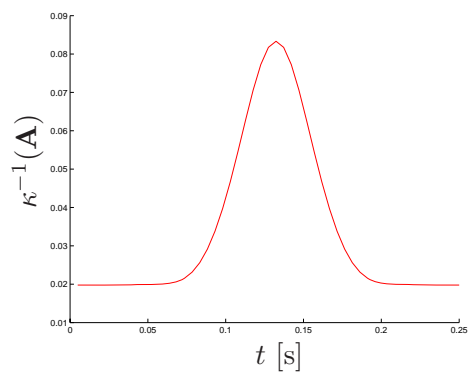


(a) PAN torques

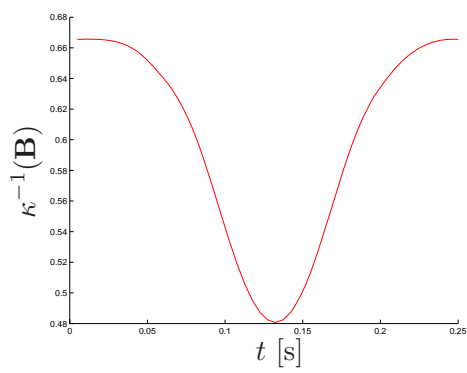


(b) TILT torques

Figure 31: Actuated joint torques

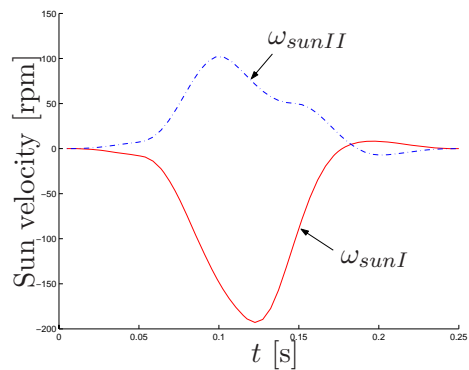


(a)

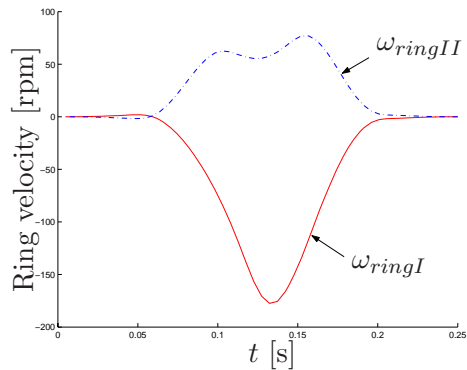


(b)

Figure 32: Inverse condition number of: (a) the forward Jacobian  $\mathbf{A}$ , and (b) the inverse Jacobian  $\mathbf{B}$



(a)



(b)

Figure 33: Angular velocities of: (a) sun gears; and (b) ring gears

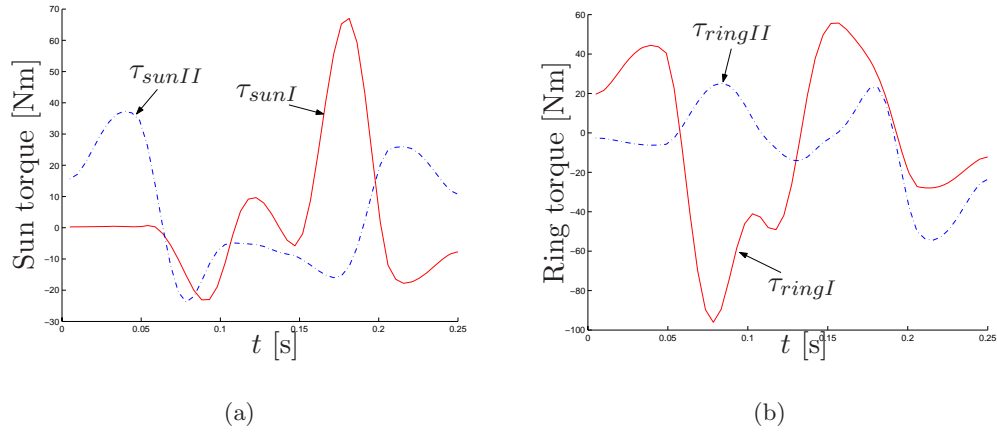


Figure 34: Torques of: (a) sun gears; and (b) ring gears

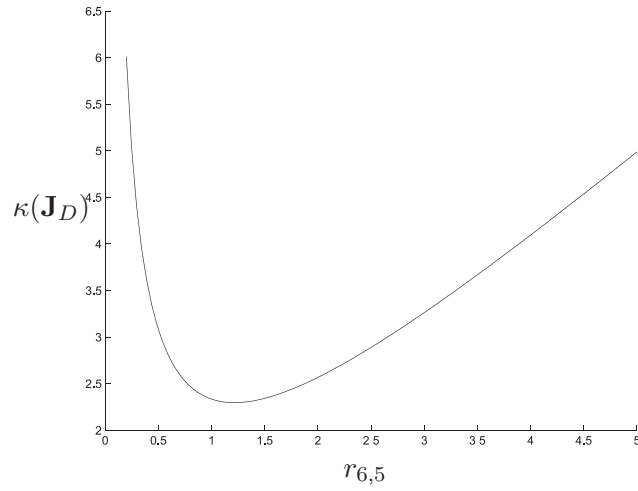


Figure 35: Condition number of  $\mathbf{J}_D$  vs.  $r_{6,5}$

Table 6: Peak requirements

$\bar{\omega}_S$ [rpm]	$\bar{\tau}_S$ [Nm]	$\bar{\omega}_R$ [rpm]	$\bar{\tau}_R$ [Nm]
192	72	179	84

### 3.6.4 Motor and Gear-Head Selection

The peak requirements of sun and ring gears rates and torques are determined from Figs. 33(a) & (b) and 34(a) & (b) as displayed in Table 6.

Table 7: Motor and gear head selection

Gear head ratio	$\bar{\omega}_{MA}$ [rpm]	$\bar{\tau}_{MA}$ [Nm]	$\bar{P}_{MA}$ [Watt]	$\bar{\omega}_{MB}$ [rpm]	$\bar{\tau}_{MB}$ [Nm]	$\bar{P}_{MB}$ [Watt]
20	3840	3.6	635	3580	4.2	810

Assuming that the gear-head ratio is equal to 20, the rates and torques required by the motors are computed as shown in Table 7.

Finally, the specifications of the motors chosen from the catalogue are summarized in Table 8, where

Table 8: Motor specifications

$\bar{\omega}_M$ [rpm]	$\bar{\tau}_M$ [Nm]
5000	7.1

$\bar{\omega}_M$  and  $\bar{\tau}_M$  are the maximum rate and torque that they can deliver.

## 4 Control of the McGill SMG

### 4.1 Interfacing

#### 4.1.1 SMG Control box

The SMG is equipped with four Servomotors delivering up to 7.2 N.m each ([Yaskawa Electric America, Inc., 2005](#)). The servomotors include encoders and a braking system. The Servomotor ratings and specifications are:

Name	Description
Model	Yaskawa SGMAH 08AAF4C
Voltage	200 – 240 VAC single phase
Capacity	750 W
Encoder	13 bit incremental encoder
Rated Torque	2.39 N.m
Peak Torque	7.2 N.m
Rated speed	3000 rpm (max 5000 rpm)
Moment of Inertia	$0.672 \cdot 10^{-4}$ Kg.m <sup>2</sup>

Each Servomotor is controlled by a Servo Amplifier placed in the Control Box . The specifications of the servo Amplifier are ([Yaskawa Electric America, Inc., 2005](#)):

Name	Description
Model	Yaskawa SGDH 08AE-S
Voltage	200 – 240 VAC single phase
Capacity	750 W
Rated current Output	4.4 Arms
Max current Output	13.4 Arms
Torque ref Input	up to $\pm 10$ Vdc (max $\pm 12$ Vdc)

The communication between the control system and the motors is made through the Servo Amplifiers. There are two ways of realizing the connection:

- ✓ Via an RS 232 serial port connected to Windows system, this method is used only to set the parameters of the servo amplifiers, for example to switch between Torque, Speed and Position Control Mode.
- ✓ Via a proprietary port named CN1, installed on the Servo Amplifiers, connected to I/O Controller PCI-Board. The board receives the digital signals from the encoders and the sensors and transmits analogue commands for Torque Control Mode. This board is housed on the “Slave” Computer running QNX. This computer is directly controlled by a Windows PC Computer running Matlab and OPAL-RT’s RT-Lab.

#### 4.1.2 Rt-Lab Interface

The control of the SMG is conducted by means of OPAL-RT’s RT-Lab ([Opal-RT, 2004](#)) : Hardware-in-the-loop simulation (H.I.L) for model-based design, plant simulation and control prototyping. It works in conjunction with *MATLAB Simulink<sup>TM</sup>* diagramming tools ([Mathworks-Simulink, 2002](#)). RT-Lab communicates via Ethernet with a second QNX equipped computer. This second computer houses a Sensoray 626 Mixed I/O PCI Control board, which interfaces to the Servo Amplifiers and motor hardware.

Rt-Lab has its own MATLAB Simulink specific functions which can be implemented in the global Simulink Control diagram. This diagram is compiled with Rt-Lab to “C” code on a first computer



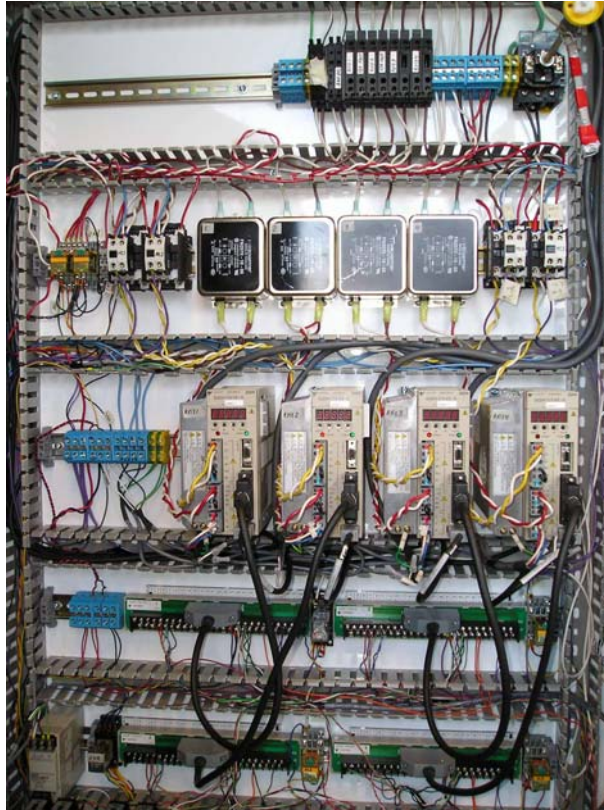


Figure 36: Control Box of the SMG

(running Windows) named “Control Computer”. Then, the C code is loaded to a second computer (with QNX system) named “Master Computer”, this computer execute the C code in order to control the robot in real time, and to save data received from the encoders/sensors.

#### 4.1.3 Sensors

**Assembly** The McGill SMG has twelve limit switches. They are used to limit the workspace and define the home configuration of the manipulator. Three switches for the *Tilt* motion and three for the *Pan* motion are used per leg, as illustrated in Fig. 37.

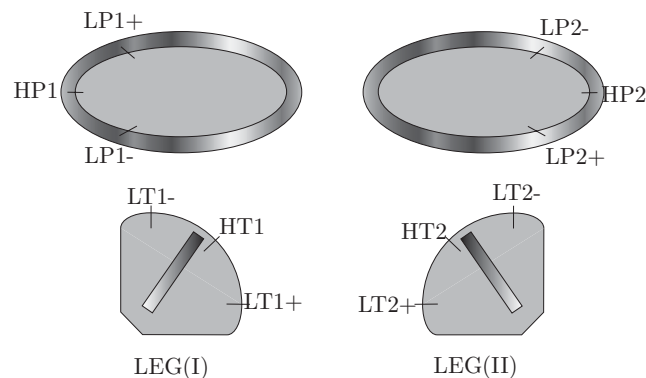


Figure 37: Sensors positioning:(L=Leg; P=Pan; T=Tilt; H=Home)

Sensors are HAMLIN 59085, which are activated when ferrous vane passes trough its slot. In fact,

a magnetic field between the frameworks keeps the circuit closed until a ferrous vane passes through its slot.//

**Tests** The sensors are connected to the Digital Input of the Sensoray I/O board, and are supplied with external 5 VDC power supply (5 Watts max). The diagram depicted in Fig. 38 shows the connections made for one sensor.

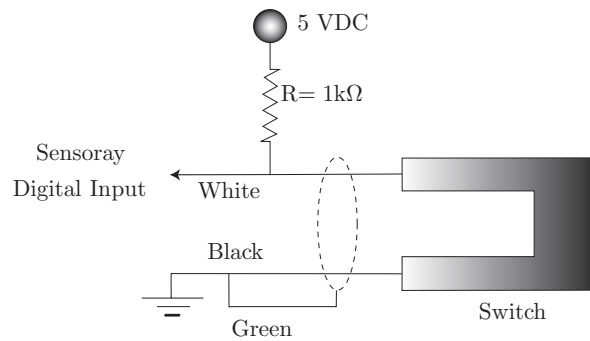


Figure 38: Sensor connections

The board shown in Fig. 39 is used to connect all the sensors to the Rt-Lab interface. The Simulink/Rt-lab interface receives a digital signal equal to 5V when the sensor operates and 0V when it does not. It is readily implemented in the global control diagram.

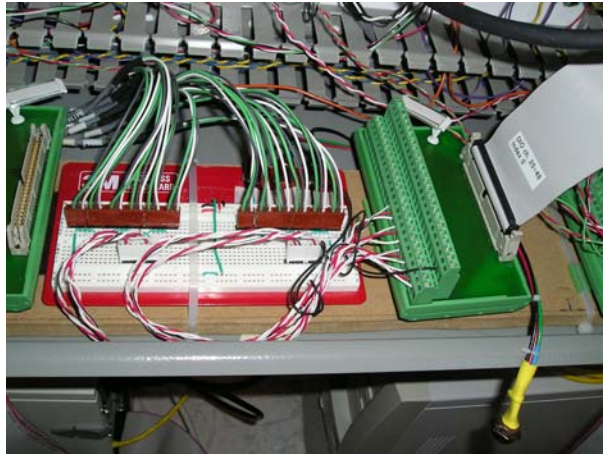


Figure 39: Sensors board

#### 4.1.4 Encoders

**Assembly** The encoders are directly connected and supplied by the servo-amplifiers, only four signals (A, A/, B,B/) are connected to the Sensoray I/O board. The encoders signals have some noise associated with the ground reference. In order to protect the Sensoray I/O board, we use opto-isolators (BEI, 2002) to separate the signal of the servo-amplifiers from the input of the Sensoray Encoder. Each opto-isolator must be supplied with 5 VDC (25 mA). To this end, we can use the Sensoray 5 VDC output as shown in Fig. 40.

**Tests** Initial tests of the encoders showed poor thresholding in the encoders isolators. This was solved by changing input resistors in the isolators (these changes, including resistor values, are indicated on the isolators)

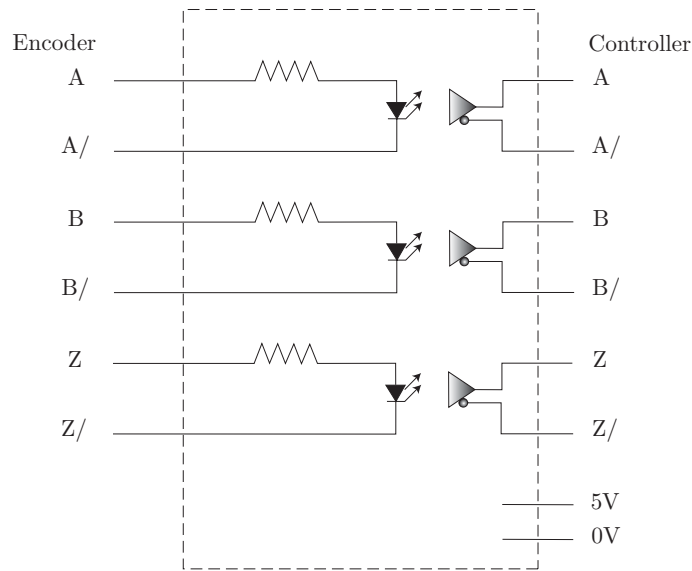


Figure 40: Opto-isolator sketch

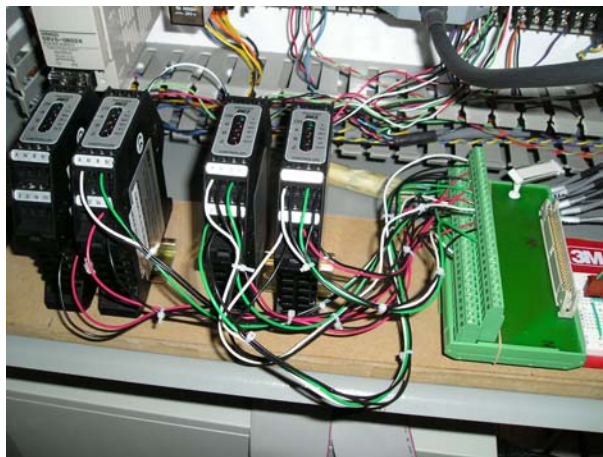


Figure 41: Encoders interface

#### 4.1.5 Analogue Input Circuit

Analog signals are either speed or torque reference signals with the following impedance:

- ✓ Speed reference input: about  $14k\Omega$
- ✓ Torque reference input: about  $14k\Omega$

The maximum allowable voltage from input signals to the servo amplifiers is equal to  $12V$ .

Analogue signals are generated in real time by the Sensoray I/O board as controlled by the control algorithm running on the “Master” Computer. In Torque Control Mode, the Servo Amplifiers regulate the motor current, since it is ideally proportional to the applied motor torque. The gain between the analogue signal and the torque is specified during the setup of the Servo Amplifiers parameters.

## 4.2 Control Algorithm

The proposed control topology of the SMG is depicted in Fig. 42. The SMG has four encoders which give us the actuation space vector  $\mathbf{q}$ . The desired trajectory of the motors in this joint space,  $\mathbf{q}_d$ , is calculated by means of the Inverse Kinematics described in section. 3.1.2.

The signal received from the encoders is a discrete signal. To obtain its derivative, we use a transfer function  $\mathcal{H}_d$

$$\mathcal{H}_d(s) = \frac{1}{1 + \frac{s}{f_0}} \quad (63)$$

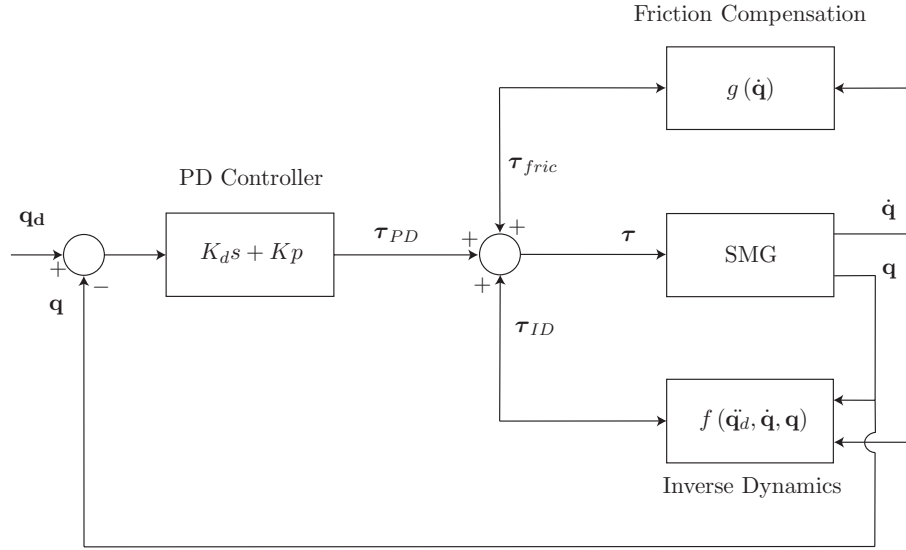


Figure 42: Control Topology

### 4.2.1 PD linear Controller

This controller generates the motors torque command  $\tau_{PD}$  from the tracking error  $\mathbf{e} = \mathbf{q}_d - \mathbf{q}$ , namely:

$$\tau_{PD} = \mathbf{K}_p (\mathbf{q}_d - \mathbf{q}) + \mathbf{K}_d (\dot{\mathbf{q}}_d - \dot{\mathbf{q}}) \quad (64)$$

where  $\mathbf{K}_p$  and  $\mathbf{K}_d$  are  $4 \times 4$  diagonal gain matrices that have to be tuned in order to achieve the desired performance.

### 4.2.2 Inverse Dynamics controller

This part aims at linearizing the non linear dynamics of the SMG in the feedback loop. Notice that since the acceleration of the motors is not measured, the inverse dynamics is based on  $f(\ddot{\mathbf{q}}_d, \dot{\mathbf{q}}, \mathbf{q})$ , which means that the inverse dynamics controller is evaluated at the desired motion acceleration  $\ddot{\mathbf{q}}_d$  that is obtained from the desired trajectory. However, instantaneous joint space position and velocity  $\mathbf{q}$  and  $\dot{\mathbf{q}}$  are obtained from the encoders.

By using equations (39), (61a) and (57a), we obtain

$$\boldsymbol{\tau}_{Pan-Tilt} = \mathbf{I}_{SMG}(\mathbf{q})\mathbf{J}_{RAGB}\mathbf{J}_{Drives}\mathbf{J}_{Gear}\mathbf{J}_{GH}\ddot{\mathbf{q}}_d \quad (65a)$$

$$+ \mathbf{C}_{SMG}(\mathbf{q}, \dot{\mathbf{q}})\mathbf{J}_{RAGB}\mathbf{J}_{Drives}\mathbf{J}_{Gear}\mathbf{J}_{GH}\dot{\mathbf{q}} - \boldsymbol{\gamma}_{Gravity}(\mathbf{q})$$

$$\boldsymbol{\tau}_{Drives} = \mathbf{I}_{RAGB}\mathbf{J}_{Drives}\mathbf{J}_{Gear}\mathbf{J}_{GH}\ddot{\mathbf{q}}_d + \mathbf{J}_{RAGB}^T \boldsymbol{\tau}_{Pan-Tilt} \quad (65b)$$

$$\boldsymbol{\tau}_{Sun-Ring} = \mathbf{I}_{Drives}\mathbf{J}_{Gear}\mathbf{J}_{GH}\ddot{\mathbf{q}}_d + \mathbf{J}_{Drives}^T \boldsymbol{\tau}_{Drives} \quad (65c)$$

$$\boldsymbol{\tau}_{GH} = \mathbf{I}_{Gear}\mathbf{J}_{GH}\ddot{\mathbf{q}}_d + \mathbf{J}_{Gear}^T \boldsymbol{\tau}_{Sun-Ring} \quad (65d)$$

$$\boldsymbol{\tau}_{Motors} = \mathbf{I}_{GH}\ddot{\mathbf{q}}_d + \mathbf{J}_{GH}^T \boldsymbol{\tau}_{GH} \quad (65e)$$

where

$$\mathbf{J}_{Gear} = - \begin{bmatrix} 1 & 0 & 0 & 0 \\ 0 & 1 & 0 & 0 \\ 0 & 0 & 1 & 0 \\ 0 & 0 & 0 & 1 \end{bmatrix} \quad (65f)$$

$$\mathbf{J}_{GH} = \frac{1}{r} \begin{bmatrix} 1 & 0 & 0 & 0 \\ 0 & 1 & 0 & 0 \\ 0 & 0 & 1 & 0 \\ 0 & 0 & 0 & 1 \end{bmatrix} \quad (65g)$$

$$\mathbf{I}_{GH} = I_{Bayside} \begin{bmatrix} 1 & 0 & 0 & 0 \\ 0 & 1 & 0 & 0 \\ 0 & 0 & 1 & 0 \\ 0 & 0 & 0 & 1 \end{bmatrix} \quad (65h)$$

$I_{Bayside}$  being equal to  $8.486e-6$  Kg.m<sup>2</sup>, ([Bayside Controls, Inc.](#), [Bayside Controls, Inc.](#)).

### 4.2.3 Friction/Stiction Compensation

To improve the closed loop performance of the system, we applied a friction-compensation algorithm ([Taghirad and Blanger, 1998](#)). The Coulomb and viscous friction model is used. Friction parameters are identified from experiments. The equation governing the friction can be written as ([Taghirad and Blanger, 1996](#)):

$$\begin{aligned} \tau_{fric}(\dot{q}) &= \tau_{v_n} u(-\dot{q})\dot{q} + \tau_{v_p} u(\dot{q})\dot{q} \\ &+ \tau_{s_n} u(-\dot{q})\text{sign}(\dot{q}) + \tau_{s_p} u(\dot{q})\text{sign}(\dot{q}) \end{aligned} \quad (66a)$$

where

$$u(x) = \begin{cases} 1 & \text{if } x > 0 \\ 0 & \text{if } x \leq 0 \end{cases} \quad (66b)$$

$\tau_{v_n}$  and  $\tau_{v_p}$  are the viscous friction coefficients depending on the direction of the velocity,  $\tau_{s_n}$  and  $\tau_{s_p}$  are the Coulomb friction coefficients as illustrated in Fig. 43 ([Taghirad, 1997](#)).

The idea of friction compensation is to estimate the friction torque at each instant from the measured velocity of the system, and to increase the reference command to the servo amplifier corresponding to the estimated friction. Ideally, the estimated friction should be equal to the actual friction; however, the magnitude of friction depends on the operating conditions, and special care must be taken so that over-compensation does not occur, which may introduce instability in the system.

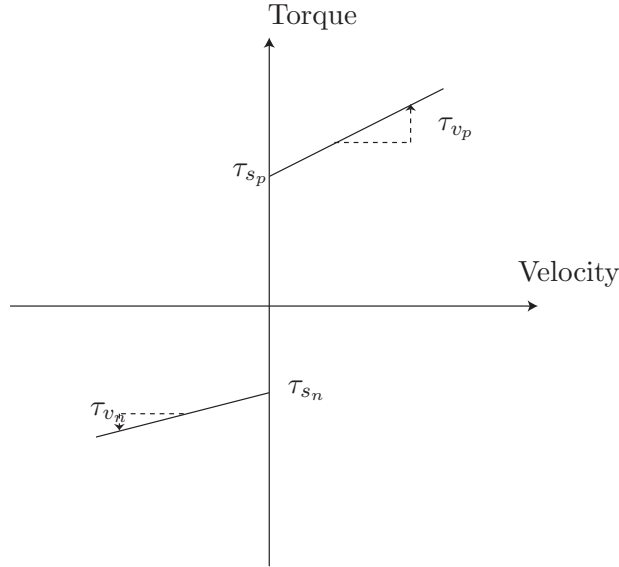


Figure 43: Coulomb and viscous friction

## 4.3 Experiments

### 4.3.1 Parameters settings

For the first tests, the gains of the servo amplifiers are set lower than the standard values.

Code	Description	Actual	Standard	Units
Pn400	Torque Reference Input Gain	100	30	$0.1V/\tau_{rated}$
Pn402	Forward Torque Limit	20	800	%
Pn403	Reverse Torque Limit	20	800	%
Pn407	Speed Limit in Torque Control	100	10000	$\text{min}^{-1}$

This means that with a 10V signal (maximum voltage supported by servo amplifiers), we obtain  $\tau = \tau_{rated} = 2.39$  N.m. Also, the test is carried without the legs, so the dynamics are different from the previous sections.

### 4.3.2 First Test

This was the first test in torque control mode. It was carried in open loop, a sinusoidal signal (magnitude 1V, Frequency 0.5Hz) is sent directly to one servo amplifier. The encoder and command signals are depicted in Fig.44

We notice that the encoder signal is not completely sinusoidal. It does not vary when the command signal is close to zero. It should be because of the friction in the drive and the RAGB (Coulomb friction in this case).

### 4.3.3 PD controller tests

First, we have to calculate online the time-derivative of the encoder signal. To this end, we used the transfer function  $\mathcal{H}_d$  : eq. (63). For two different values of  $f_0$ , we obtain the graphs depicted in Fig. 45 and Fig.46

The encoder signal is a discrete function of time, the direct time-derivative leads to a very noisy command signal (high frequencies) which may damage the motors or the structure of the robot. The

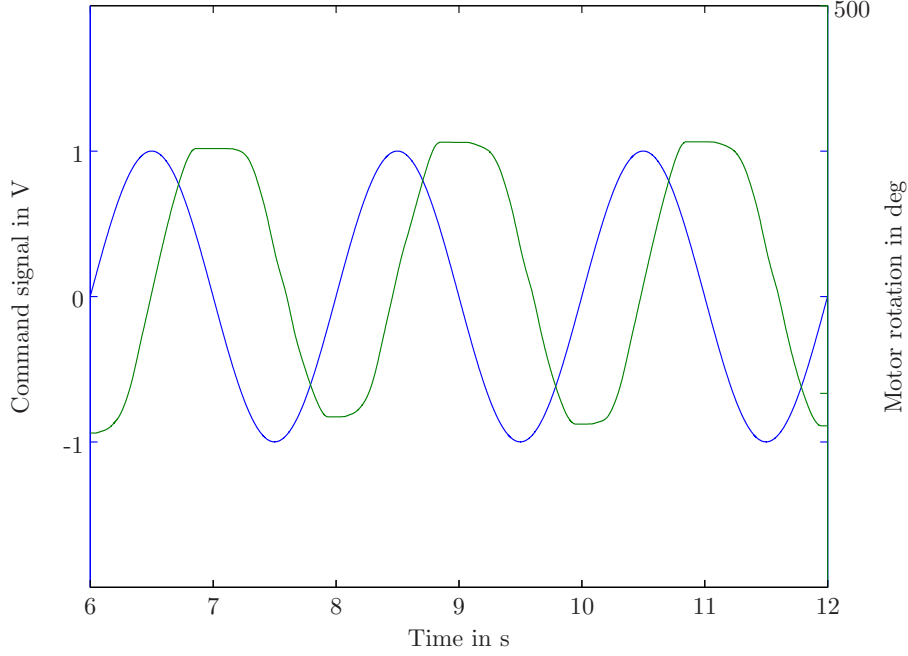


Figure 44: Encoder and Command signals

used filter removes the high frequencies with respect to  $f_0$ , which has to be tuned for each type of desired trajectories.

Then, we used a closed loop algorithm with only PD controller, same architecture than in Fig. 42 but without the inverse dynamics and friction compensation. The desired trajectory of the only motor used in this test is a square signal at  $\pm 50$  degrees and 0.5 Hz. The desired and actual trajectories are shown in Figs. 47 and 48 with different values of  $K_p$  and  $K_d$ .

With small gains, the error with reference to the desired trajectory is bigger, this is due to friction. In fact, when the error goes down:

$$\tau = K_p(q_d - q) + K_d(\dot{q}_d - \dot{q}) < \tau_{friction} \quad (67)$$

Therefore, the motor stops before reaching the desired position. We can notice that the upper and lower limits are not the same in Fig. 47. This is due to non-linear friction and non symmetry of the motors distribution.

In Fig. 48,  $K_p$  is higher than the value required. The motor goes over the desired position because of the inertia of the system. Therefore, an undesired oscillatory phenomenon appears.  $K_p$  and  $K_d$  have to be tuned to avoid it.

#### 4.3.4 Comments

After some tests with Pan and Tilt motions, we noticed that there are some plays and backlash in the Drives, the RAGB and in the distal joints. The backlash is amplified especially in tilt motion and for high speeds.

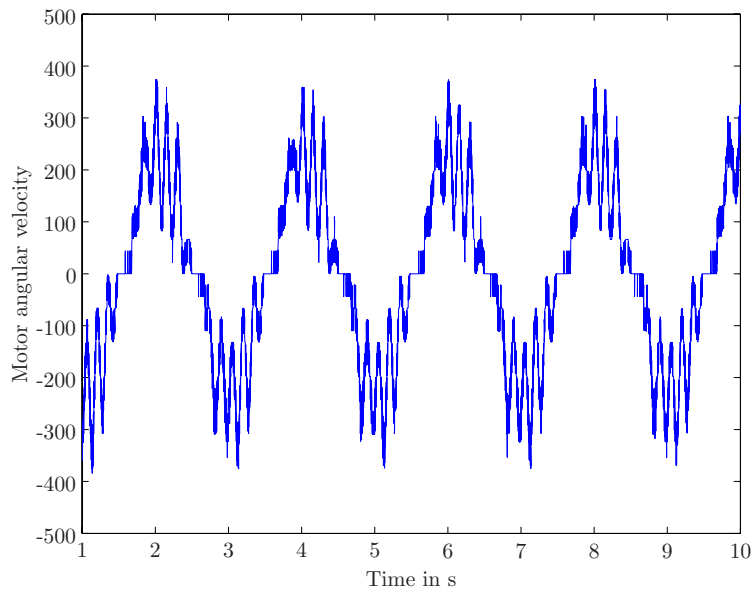


Figure 45: Time-derivative of the encoder signal,  $f_0 = 10^3\text{Hz}$

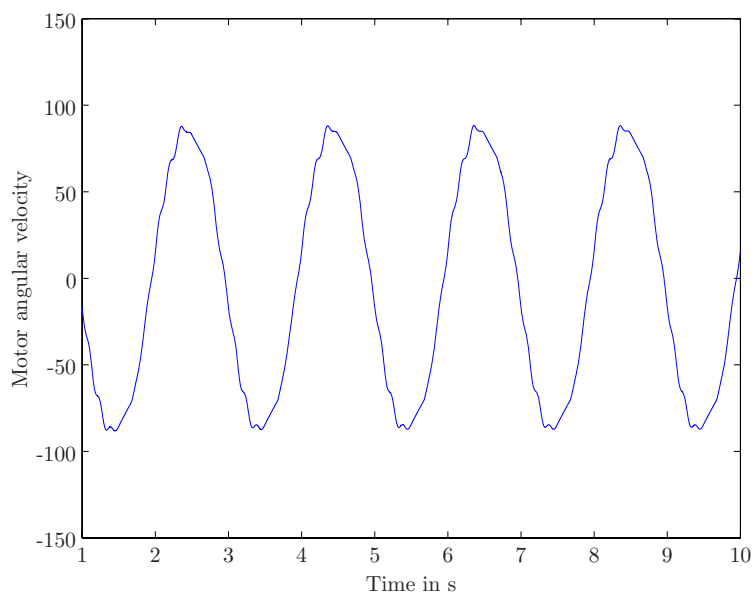


Figure 46: Time-derivative of the encoder signal,  $f_0 = 1\text{Hz}$



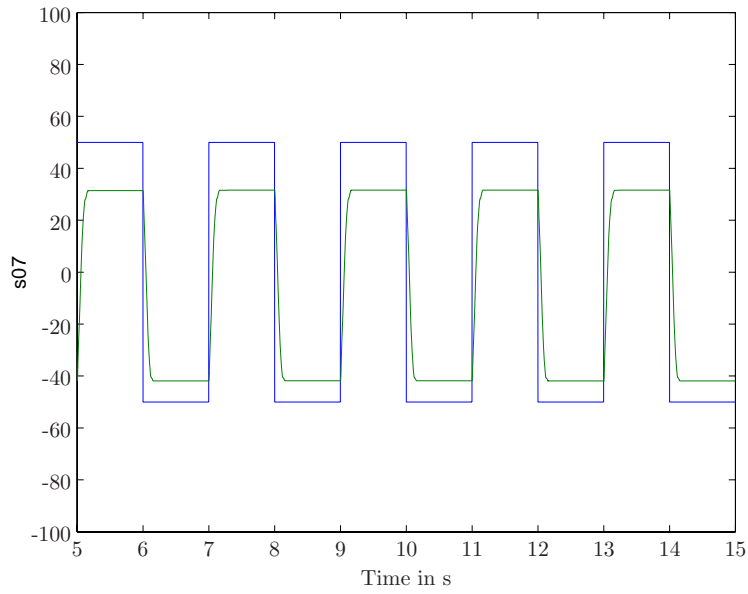


Figure 47: Desired and Actual trajectories,  $K_p = 0.025$  and  $K_d = 0$

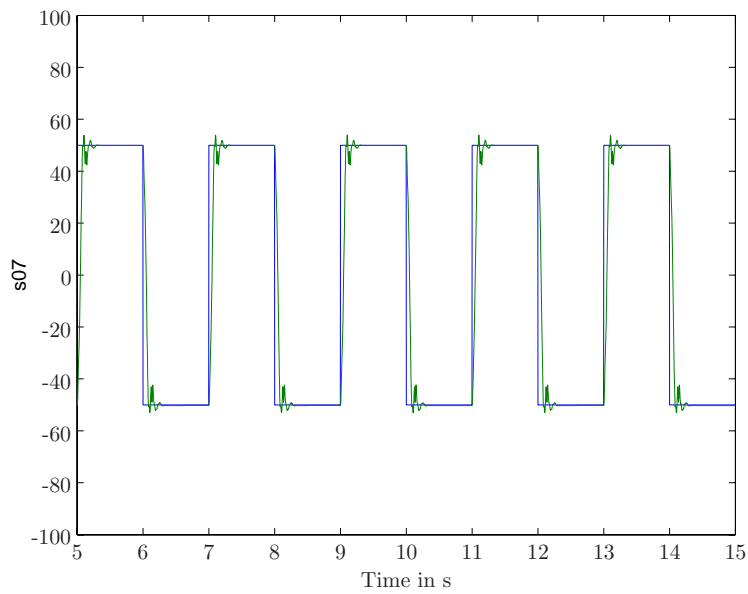


Figure 48: Desired and Actual trajectories,  $K_p = 0.5$  and  $K_d = 0.06$

## 5 Detailed Design

### 5.1 Design of links and joints

In order to minimize the weight impact of links, extensive use has been made of advanced carbon fiber composite materials. Both sets of parallelogram joints 3 and 6 have been designed using carbon fiber composite materials. The main advantage of using such materials is their excellent properties (stiffness-to-weight ratio and strength-to-weight ratio). For the case of this manipulator, the design was driven mostly by the stiffness-to-weight ratio. When compared to comparable metallic designs, composite materials provide the possibility for saving up to 50% of the link weight for the same resulting stiffness.

Composite component manufacturing involves combining carbon fibers with a suitable epoxy matrix material in order to achieve the desired lightweight properties. The resulting composite materials have good internal damping properties due to the epoxy matrix. Roughly, the damping coefficient is three times the damping coefficient of typical metal such as aluminium. This is an added benefit of the carbon fiber composite materials.

Some important aspects must be considered in order to design efficient parts using composite materials. Firstly, it is desirable to design composite parts as single structures rather than assemblies of smaller structures in order to avoid joints or other areas where composites can fail. The links in this project were designed as singular shell structures without using bolts or other attachments. As a disadvantage, composite materials do not perform as bearing (frictional) surfaces. Thus bearings remain as metallic structures and the resulting links must have metal parts (inserts) that join the bearings to the composite structures. The most efficient way to do this is to design inserts that join with the composite structures by means of bonding. In this project, efficient aluminium inserts were used on each end of the composite links. The alignment of the links was performed by combining the composite structures with the metallic inserts in a precise bonding jig. A specialized adhesive was used to ensure a good bond between the aluminium inserts and the carbon structures.

The resulting composite structures were then assembled with the robot.

The prototype fabrication methodology of the fibre-composite structures is illustrated in Appendix B.

### 5.2 Design of drives

The design of the drive unit of the SMG is based on a planetary gear train. The rotation of the two motors gives two degrees of freedom at the end of the drive unit: these are 2 rotations: the tilt and the pan. The tilt is produced by the rotation of the planets around their own axis, while the pan is produced by the rotation of the Planet Carrier of the epicyclic train.

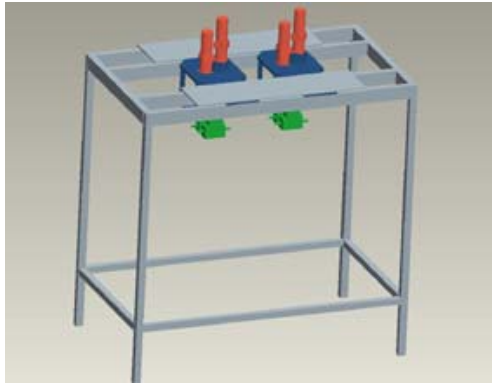
The drive unit is split into three parts:

1. The “support”, which corresponds to the fixed parts as the frame, i.e., the aluminium support of the robot, the motors and gear heads;
2. The “gearbox” based on a planetary gear train;
3. The “Transmission”, which is the link between the gearbox and the composite legs of the robot.

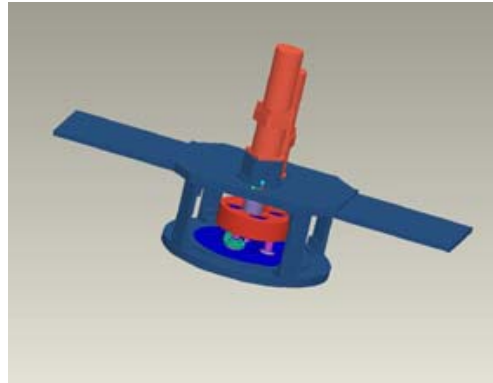
#### 5.2.1 The support

The SMG is hanged by a frame with aluminium bars in order to gain in stiffness, as depicted in Fig. 49(a).

Moreover, an aluminium support is fixed to that frame in order to carry each drive unit. As there are two drive units, there are also two aluminium supports. From now, we are talking only about one drive unit as the other one is the same.



(a) Frame



(b) Motors and gearbox

Figure 49: Drive units mounted on the frame

Each aluminium support is composed of two parallel plates: one at the top and the other at the bottom. The top plate is bigger and is linked to the frame. The motors and the gear head are mounted on the top plate. The bottom plate supports the “Gearbox” by means of a large ball bearing. Aluminium bars link these two plates.

A “motor gear” and an “extra shaft” are mounted to the output shaft of the gear heads. In order to use this extra shaft and to minimize the size of the mechanism, an “extra support” is added to put the corresponding motor upper than the other one.

### 5.2.2 The Gearbox

The planetary gear train, also called “gearbox”, is the core of the drive unit and depicted in Fig. 49(b). As a matter of fact, each gearbox is composed of eleven gears:

A couple of gears (ratio = 1) transmits the rotation between motor  $M_A$  and the sun shaft;

Another gear transmits the rotation of the other motor to the ring gear (ratio = 1);

The sun gear is directly driven by the first motor;

Three planet gears are driven simultaneously by the sun gear (ratio = 1.5), and the “internal gear” of the ring gear;

A couple of gears is used to reverse the orientation of the rotation of one planet.

This planetary gear train uses three planets directly driven by the sun and the ring gear. Amongst the three planets, only two are used to generate the tilt motion. However, the other one is useful to balance the system. According to section 3.6.4, the ratio between the planets and suns had better be between 1.5 and 2. In order to minimize the size of the mechanism, the ratio 1.5 was chosen (constraining also the ratio between planets and ring gear). Finally, all the other ratios were set to 1, and two additional gears are used to reverse the orientation of the rotation of one planet, and to place the second output shaft symmetrically regarding to the first one.

Even they can be less efficient than helical gears, spur gears have been chosen because of their low cost (particularly for the internal gear). To dimension all these gears (as all the parts of the drive unit), we used all the data coming from the dynamics study. Moreover, in order to protect our system, we also take into account the maximum power that the motors can deliver (adding also a safety factor). In this

way, all the gears can support the maximum torque and the maximum speed of the motors, even if the predefined trajectory of the robot need not to go until these limits.

Table 9: Description of the Gears of the SMG

Gear Name	Material	App. Weight [kg]	Quantity	Drawing No	Number of teeth
Motor Gear 1 (Sun)	Steel 4320	0.43	2	1	38
Motor Gear 2 (Ring)	Steel 4340	0.62	1	2	38
Ring Gear	Steel 4340	4.34	1	3	38/94
Sun Gear	Steel 4320	0.34	1	4	23
Planet Gear	Steel 4320	0.63	3	5	35
Reverser Gear	Steel 4320	0.33	2	6	39

Besides, the characteristics of some gears are summarized in Table 9.

In order to support the gears of the planetary gear train, we need to use a planet carrier (PC). The planet carrier is in aluminium and is driven by the planets. As a matter of fact, the planet carrier transmits the pan motion to the legs of the manipulator.

The PC is made up of three dependant plates:

Two plates to support the planets shafts (one at the top, one at the bottom);

One intermediate plate smaller than the others to support the sun shaft and the reverser shaft They are linked by bars so as to make a stiff assembly.

For the dimensioning, we used the results from the dynamics study. For example, with the solution using universal joint, some dimensioning are summarized in Table 10.

where

$D$  is the diameter of without considering “shaft” width;

$D'$  is the diameter of considering the “shaft”;

$D_{PC}$  is the external diameter of the planet carrier;

$D_{tot}$  is the diameter of the support.

where

About the other parts of the design, we use shafts with a diameter of 22 mm, and with grooves to insert snap rings. Moreover, we use some spacers to locate the components.

In order to simplify the design, we use identical bearings (6004.2RSR from FAG).

Finally, two solutions were investigated to link to the rotating parts to the support:

A Roller Guide (with rail and carriages);

A large Ball Bearing.

The second solution was selected for a matter of cost. The bearing is mounted between the bottom plate of the support and the bottom plate of the planet carrier. Some covers are used to protect it.

Table 10: Planet carrier dimensioning

	$a$	$d$	$d'$	$\alpha$	$x$	$y$	$y_{ext}$	$D$	$D'$	$D_{PC}$	$D_{tot}$
Standard solution	175	118.6	180.6	90	175	118.6	180.6	369.55	393.85	503.85	543.85
	175	118.6	180.6	80	154.41	116.8	178.8	349.5	374.81	484.81	524.81
	175	118.6	180.6	70	134.44	111.45	173.45	328.9	354.74	464.74	504.74
	175	118.6	180.6	60	115.7	102.71	164.71	308.31	334.12	444.12	484.12
	175	118.6	180.6	50	98.77	90.85	152.85	288.45	313.55	423.55	463.55
	175	118.6	180.6	40	84.15	76.23	138.23	270.13	293.71	403.71	443.71
	175	118.6	180.6	30	72.29	59.3	121.3	254.3	275.44	385.44	425.44
	175	118.6	180.6	0	56.4	0	62	231.4	239.56	349.56	389.56
Reduced Solution	150	118.6	180.6	90	150	118.6	180.6	322.59	350.17	460.17	500.17
	150	118.6	180.6	80	129.41	116.8	178.8	302.84	331.72	441.72	481.72
	150	118.6	180.6	70	109.44	111.45	173.45	282.37	312.08	422.08	462.08
	150	118.6	180.6	60	90.7	102.71	164.71	261.7	291.66	401.66	441.66
	150	118.6	180.6	50	73.77	90.85	152.85	241.51	270.99	380.99	420.99
	150	118.6	180.6	40	59.15	76.23	138.23	222.61	250.7	360.7	400.7
	150	118.6	180.6	30	47.29	59.3	121.3	206.01	231.6	341.6	381.6
	150	118.6	180.6	0	31.4	0	62	181.4	191.7	301.7	341.7
Minimum Solution	125	118.6	180.6	90	125	118.6	180.6	276.71	308.41	418.41	458.41
	125	118.6	180.6	80	104.41	116.8	178.8	257.43	290.86	400.86	440.86
	125	118.6	180.6	70	84.44	111.45	173.45	237.25	271.94	381.94	421.94
	125	118.6	180.6	60	65.7	102.71	164.71	216.6	251.98	361.98	401.98
	125	118.6	180.6	50	48.77	90.85	152.85	196.09	231.43	341.43	381.43
	125	118.6	180.6	40	34.15	76.23	138.23	176.46	210.8	320.8	360.8
	125	118.6	180.6	30	22.29	59.3	121.3	158.78	190.81	300.81	340.81
	125	118.6	180.6	0	6.4	0	62	131.4	145.29	255.29	295.29

### 5.2.3 The Transmission

The goal of this section is to transmit the motion from the Gearbox to the “proximal” links of the legs of the manipulator: the rotation of the planets (tilt) and the rotation of the planet carrier (pan), to the composite legs. In fact, it has to change the direction of the rotation. At the output of the gearbox, the rotations have a vertical axis. The transmission must convert them into rotations around a horizontal axis.

In order to realize this connection, we studied the implementation of two different systems:

1. Universal Joint;
2. Bevel gear box.

On the one hand, the universal joint would be tilted at 90 degrees to change the direction of rotation to a perpendicular axis. We need to mount some brackets on the final plate of the planet carrier in order to support the output shafts of the universal joints. For our design, according to the torques, which are required, the universal joint that we selected is: CJ650DBKW1SS from Curtis Universal. On the other hand, the use of bevel gears box aims at turning the direction of rotation of 90 degrees. To use this solution, we need to mount an extra plate linked to the bottom plate of the Planet Carrier in order to support the bevel gears box.

Table ?? shows the nomenclature of each drive unit.

## 5.2.4 Assembly

### General assembly procedure:

#### **Assembly of rotating parts**

1. Assemble the shafts of the planets and the reverser shaft separately as described in the other procedures;
2. Insert the reverser shaft into Planet Carrier End Plate;
3. Assemble the Intermediate Plate of Planet Carrier on the reverser shaft by means of the four bars;
4. Put the shafts of the three planets, already assembled, in the Planet Carrier End Plate, in their appropriate location;
5. Put the sun shaft, assembled at the end of step 1, in the Planet Carrier Intermediate Plate;
6. Put the Top Plate of the Planet Carrier on the top of the three planets shafts, and fix it with the bars.
7. Assemble the sun shaft (Step 2)

At that point, most of the rotating parts are assembled together and the design depicted in Fig. 50 is obtained.

#### **Assembly of motors and support**

8. Assemble the motors with their gear head;
9. Put the “extra support” of the gear head on the top of the superior plate of the support;
10. Put the Motor 1 (with gear head) in its location;
11. Put the motor gear 1 (to sun) on the gear head shaft;
12. Put the Motor 2 (with gear head) on the extra support of the gear head;
13. Assemble the extra shaft (as described below);
14. Link this extra shaft with the shaft of gear head 2, thanks to the coupling.

#### **Final assembly**

15. Put the big bearing on the plate which will support the rotating parts;
  16. Put a cover on this bearing;
  17. Put the final plate of the planet carrier (with all the rotating parts) inside the big bearing;
  18. Add the other cover of the bearing below this plate;
  19. Link the two big support plates (top plate with motors and bottom plate with rotating parts) thanks to the bars;
- Now, the drive unit is totally assembled.
20. Finally, it remains to assemble two drive units of this kind to the frame and to position them thanks to a positioning plate.

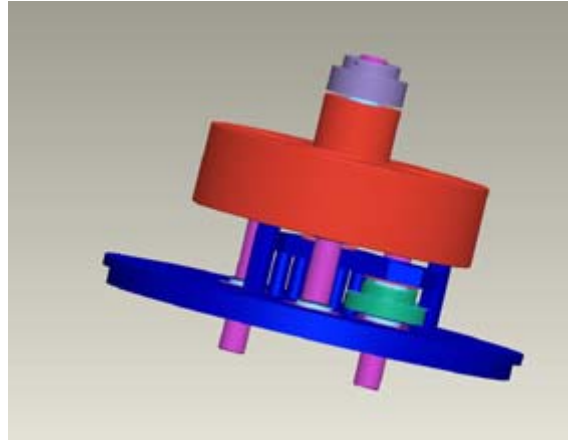


Figure 50: Assembly of the rotating parts

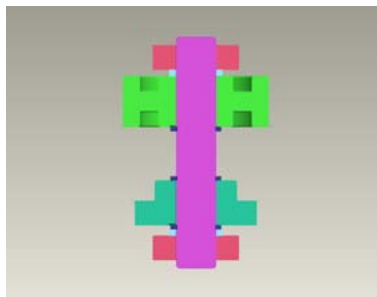
**Assembly of shafts:**

**Assembly of planet shaft 1**

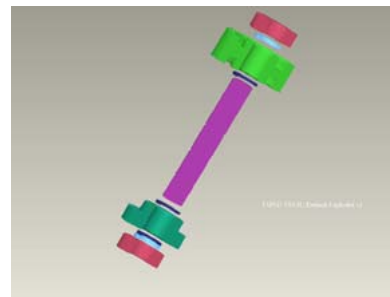
1. Put the 2 snap rings located in the middle of the shaft;
2. Put the gears (planet and reverser gear) on the shaft onto the corresponding snap ring;
3. Put the other snap ring on the other side of the reverser gear;
4. Put the spacers on the other side of the two gears;
5. Put the two ball bearings press-fitted on this shaft directly on the spacers.



(a)



(b)



(c)

Figure 51: Assembly of planet shaft 1 (with reverser gear)

**Assembly of planet shaft 2 and 3**

1. Put the 2 snap rings;
2. Put the planet gear on the shaft onto the corresponding snap ring;
3. Put the spacers on the other side of the planet and below the other snap ring;
4. Put the two ball bearings press-fitted on this shaft directly on the spacers.

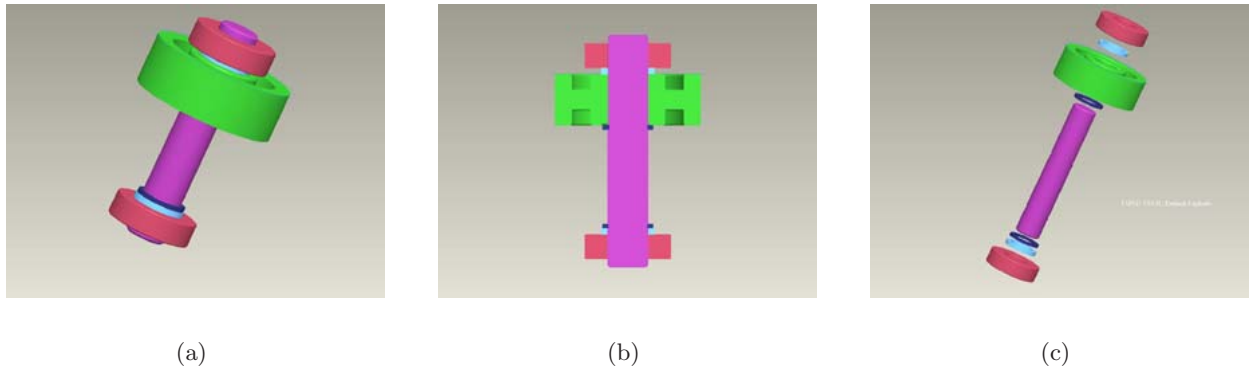


Figure 52: Assembly of planet shafts 2 and 3 (without reverser gear)

### Assembly of reverser shaft

1. Put the snap ring;
2. Put the reverser gear on the shaft onto the snap ring;
3. Put the spacers on the other side of the gear and on the other snap ring;
4. Put the two ball bearings press-fitted on this shaft directly on the spacers.

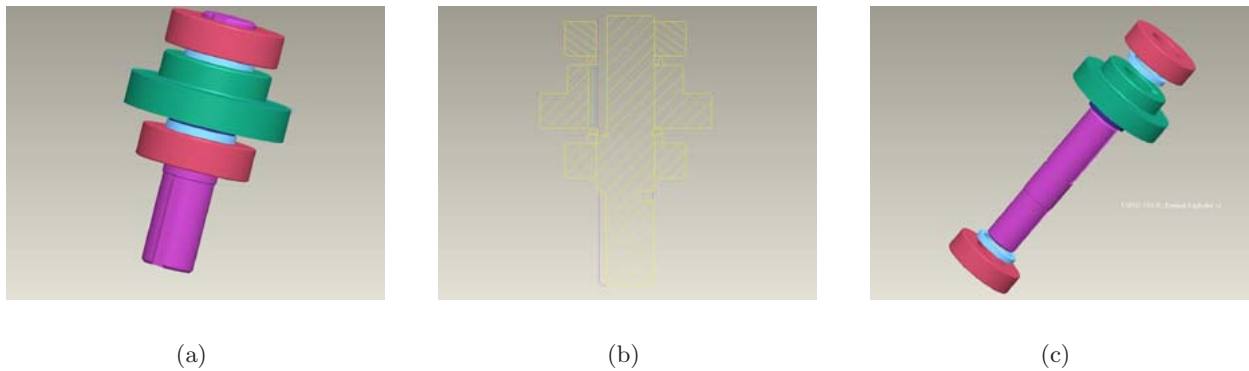


Figure 53: Assembly of reverser shaft

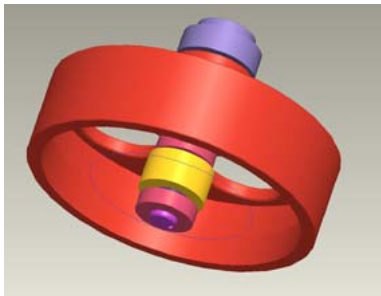
### Assembly of the sun shaft

- Step 1:
  1. Put the snap ring;
  2. Put the sun gear on the shaft onto the snap ring;
  3. Put the spacer on the other side of the snap ring;
  4. Put the ball bearing press-fitted on this shaft directly on this spacer;
  5. Add a spacer on the other side of the sun;
  6. Put another ball bearing on this shaft directly on this spacer.

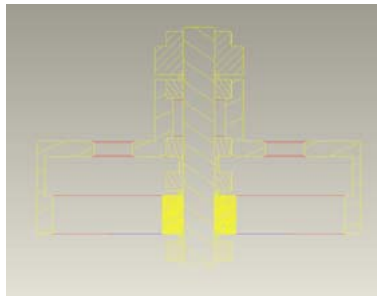


- Step 2:

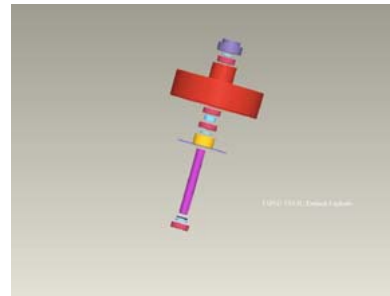
1. Add another spacer on this ball bearing;
2. Put another ball bearing directly on this spacer;
3. Put the ring gear on this ball bearing;
4. Put another ball bearing directly on the top of the ring gear;
5. Add another spacer on this ball bearing;
6. Put the motor gear press-fitted on this shaft directly on this spacer;
7. Set the set screw of the motor gear.



(a)



(b)



(c)

Figure 54: Assembly of sun shaft

#### **Assembly of the extra shaft to the motor**

1. Put the top snap ring;
2. Put the ball bearing press-fitted on this shaft directly on this spacer;
3. Put the intermediate snap ring;
4. Put the motor gear 2 on the shaft onto this snap ring;
5. Put the last snap ring;

## 6 Test results

## References

18

- (1992, 1990). *Québec Electrical Code* (16th ed.). 178 Rexdale Boulevard, Rexdale, ON, Canada M9W 1R3: Canadian Standards Association. CSA Standard C22.1-1990 — CEC Part I. [73](#), [74](#), [77](#)
- Adept Technology, Inc. *Adept Servo Kit*. PHONE: (925) 245-3400, FAX: (925) 960-0452, EMAIL: info@adept.com: Adept Technology, Inc. [63](#)
- Angeles, J. (2002). *Fundamentals of Robotic Mechanical Systems: Theory, Methods, and Algorithms* (2 ed.). New York: Springer-Verlag. [18](#), [31](#)
- Angeles, J. (2004). The qualitative synthesis of parallel manipulators. *ASME Journal of Mechanical Design* *126*(4), 617–624. [8](#)
- Angeles, J. (2005). The morphology design for a parallel schonflies-motion generator. In *Robotics Systems for Handling and Assembly*, Braunschweig. [9](#)
- Angeles, J. and A. Morozov (2003a). A device for the production of schonflies motions. *International Patent Application*. [6](#)
- Angeles, J. and A. Morozov (2003b). A device for the production of schonflies motions. *International Patent Application*. [10](#)
- Angeles, J., A. Morozov, and O. Navarro (2000, April 24–28). A novel manipulator architecture for the production of scara motions. In *Proc. IEEE Int. Conf. Robotics and Automation*, San Francisco, pp. 2370–2375. CD-ROM 00CH37065C. [8](#)
- Bayside Controls, Inc. *Stealth™ PS Advanced Series: The Ultimate in Gearhead Performance*. Bayside Controls, Inc. [45](#), [64](#)
- BEI (2002). *BEI Industrial Encoder Division*. 7230 Holister Avenue - Goleta, CA 93117-2891. [42](#)
- Bottema, O. and B. Roth (1979). *Theoretical Kinematics*. Amsterdam: North Holland. [6](#)
- Brumson, B. (2005). Parallel kinematic robots. <http://www.roboticsonline.com>. [3](#)
- Clavel, R. (1988). Delta, a fast robot with parallel geometry. In *Proc. 18th Int. Symp. Industrial Robots*, Lausanne, pp. 91–100. [8](#)
- Company, O., F. Pierrot, T. Shibukawa, and K. Morita (2001, March 21). Four-degree-of-freedom parallel robot. *EP1084802*. [8](#)
- Denavit, J. and R. Hartenberg (1964). *Kinematic Synthesis of Linkages*. McGraw-Hill Book Company, New York. [9](#)
- Dietmaier, P. (1992, Sept. 13-16). Inverse kinematics of manipulators with 3 revolute and 3 parallelogram joints. In *Proc. ASME 22nd. Biennial Mechanisms Conference*, Volume 45, Scottsdale, pp. 35–40. [8](#)
- Hervé, J. (1978). Analyse structurelle des mécanismes par groupes de déplacements. *Mechanism and Machine Theory* *13*, 437–450. [6](#)
- Hervé, J. and F. Sparacino (1992, September 7–9). Star, a new concept in robotics. In *Proc. 3rd Int. Workshop on Advances in Robot Kinematics*, Ferrara, pp. 176–183. [8](#)

- Heumann, G. (1961). *Magnetic Control of Industrial Motors — Part 1*. John Wiley & Sons, Inc. 75
- Hillier, F. and G. Lieberman (1995). *Introduction to Mathematical Programming*. McGraw-Hill, Inc., New York. 10
- Juvinall, R. and K. Marshek (2000). *Fundamentals of Machine Component Design, Third Edition* (2 ed.). John Wiley & Sons. 26
- Leang, B. (2002, December). *Sigma II Wiring Guidelines — Application Notes*. 2121 Norman Drive South Waukegan, IL 60085 — (847) 887-7000: Yaskawa Electric America, Inc. Rev.3/26/02. 77, 80
- Littelfuse (2005). *Circuit Protection Technology*. Littelfuse. 76, 77
- Malik, I. (2005). *Tools for the Simulation-Based Design of a Fast Parallel Schönflies Motions Generator*. Ph. D. thesis, Centre for Intelligent Machines, McGill University, Montreal, Quebec, Canada. 31
- Mathworks (2002). “*fsolve*” function, the MathWorks, Inc. 15
- Mathworks-Simulink (2002). “*SIMULINK*” Simulation and Model-Based Design, the MathWorks, Inc. 40
- McMaster-Carr (2005). *Internet Catalog*. McMaster-Carr. 75, 76
- Merlet, J.-P. (1997). *Les robots parallèles* (2 ed.). Hermès. 3
- Millermaster, R. (1970). *Harwood’s Control of Electric Motors* (Fourth ed.). Wiley Interscience. 62
- Moeller Electric Corp. (2003a). *03 Magnetic Contactors, Magnetic Starters — Online Catalog*. Moeller Electric Corp. 80, 81
- Moeller Electric Corp. (2003b). *04 Overload Relays — Online Catalog*. Moeller Electric Corp. 81
- Moeller Electric Corp. (2003c). *05 RMQ Titan, Control Circuit Devices — Online Catalog*. Moeller Electric Corp. 81
- Opal-RT (2004). “*RT-LAB*” Real-Time Simulation, Opal-RT Technologies Inc. 40
- Parker Hannafin, Corp. *Daedal Precision Gearheads*. Parker Hannafin, Corp. Catalog 8085/USA. 64
- Phason Electronic Control Systems (2004). *129-0 240V Power Contactor Unit — Online Catalog*. Phason Electronic Control Systems. 80
- Salerno, A. and J. Angeles (2004). The control of semi-autonomous two-wheeled robots undergoing large payload-variations. In *Proc. IEEE Int. Conf. Robot. Automat.*, New Orleans, LA. 62
- Salerno, A., R. Perlin, and J. Angeles (2004, July). The embodiment design of a two-wheeled self-balancing robot. In *Proc. The Inaugural CDEN Conference*, Montreal, Canada. 62
- Sprecher+Schuh. *KWIK Starters — Online Catalog*. Sprecher+Schuh. 80
- Stewart, D. (1965). A platform with six degrees of freedom. In *Proc. Inst. Mech. Engineering*, Volume 180, London, pp. 371–386. 4
- Taghirad, H. (1997, March). *Robust torque control of harmonic drive systems*. Ph. D. thesis, McGill University, Montreal. 45

- Taghirad, H. and P. Blanger (1996, Dec). An experimental study on modelling and identification of harmonic drive systems. *Proceeding of IEEE Conference on decision and control*. 45
- Taghirad, H. and P. Blanger (1998, Sept). Robust friction compensator for harmonic drive transmission. *Proceeding of IEEE Conference on Control applications*. Trieste, Italy. 45
- Traister, J. (1994). *Complete Handbook of Electric Motor Controls* (Second ed.). The Fairmont Press, Inc. 71, 72, 73, 74, 75
- Wohllhart, K. (1992). Displacement analysis of the general spatial parallelogram manipulator. In *Proc. 3rd International Workshop on Advances in Robot Kinematics*, Ferrara, Italy, pp. 104–111. 8
- Yang, T., Q. Jin, A. Liu, F. Yao, and Y. Luo (2001, Sept. 9–12). Structure synthesis of 4-dof (3-translation and 1-rotation) parallel robot mechanisms based on the units of single-opened-chain. In *Proc. ASME Design Engineering Technical Conference DETC'01*, Pittsburgh. 8
- Yaskawa Electric America, Inc. (2004, May). *Sigma II Servo System — Product Catalog Supplement*. Yaskawa Electric America, Inc. G-MI#99001I-SigmaOO Printed In U.S.A. 81
- Yaskawa Electric America, Inc. (2005, January). *Sigma II Series Servo System User's Manual*. Yaskawa Electric America, Inc. YEA-SIA-S800-32.2G Printed In U.S.A. 40, 77, 80, 81, 83, 88, 90, 91

# A SMG Robot Control: Actuation System, I/O Control-Signal Board, and Motor-Starter Design & Testing

This section explains the detailed dimensioning aspects of the actuation system of the SMG. Design and testing issues related to an implementation of a custom-made magnetic motor starters for the robot at hand are reported as well.

## List of Abbreviations:

AC	Alternate-Current
DC	Direct-Current
MC	Magnetic Contactor
OBCC	On-Board Control Circuit
PG	Planetary Gearhead
SMG	Schönflies Motion Generator

## A.1 Introduction

The success of any installation of electrically driven machinery is dependent on the proper selection and correlation of the machine, the motor and the controller. Each is important, as improper application of a motor or a controller will lower the efficiency of the installation and may cause it to be a failure (Millermaster, 1970).

In order to produce successful installations, it is necessary to understand the factors which enter into the selection of the machine, motor, and controller, and therefore, to have a good knowledge of the characteristics of the three devices. The requirements of the machine with respect to speed, torque and special functions must be known. An understanding of motor characteristics is necessary to properly select a motor which will accomplish the desired results; a knowledge of control apparatus is required to ensure the application of a controller which will cause the motor to perform the functions required (Millermaster, 1970).

## A.2 Motor and Servo Amplifier Dimensioning

In order to select an electric motor and the corresponding power amplifier, several parameters need to be taken into account (Salerno et al., 2004); (Salerno and Angeles, 2004):

- maximum continuous torque  $\tau_{maxcont}$  of the motor, which needs to be greater than the root-mean-square (RMS) torque  $\tau_{rms}$  measured at the output shaft of the motor,
- peak torque (a.k.a. stall torque)  $\tau_{peak}$  of the motor, which needs to be greater than the maximum torque  $\tau_{max}$  measured at the output shaft of the motor,
- rated speed (a.k.a. nominal speed)  $n_{nom}$  of the motor, which needs to be greater than the operating speed  $n_{op}$  measured at the output shaft of the motor,
- maximum permissible speed  $n_{maxperm}$  of the motor, which needs to be greater than the maximum speed  $n_{max}$  measured at the output shaft of the motor, and
- rated power  $P_{rated}$  of the motor, which needs to be greater than  $n_{max}\tau_{max}$ .

When dimensioning an electric motor, there are of course other issues to take into account, such as motor dimensions, weight, power density etc. Once all these factors have been considered, a motor/power amplifier can be selected.

Motor P/N	Type	$\tau_{maxcont}$ Nm	$\tau_{peak}$ Nm	$n_{nom}$ rpm	$n_{maxperm}$ rpm	$P_{rated}$ W
Adept Servo Kit (750W)	AC servo	2.39	5.1	3000	4500	750
Bayside BM090-2	DC brushless	2.97	8.90	n/a	3600	n/a
Pacific Scientific PMA24	DC Brushless	2.6	9.6	3000	4950	n/a
Yaskawa Sigma II SGMAH-08A	AC servo	2.39	7.1	3000	5000	750

Table 11: Motor specs - comparison

Component	$\tau_{rms}$ Nm	$\tau_{max}$ Nm	$n_{op}$ rpm	$n_{max}$ rpm
Motor #1 (associated with sun gear of the custom-made drive)	N/A	5.85	N/A	4800
Motor #2 (associated with ring gear of the custom-made drive)	N/A	7.0	N/A	4460

Table 12: Numerical simulation results

In selecting the SMG robot motors one basic guideline was added to the standard guidelines outlined above: the actuation system should have better performance than those of the Adept Cobra i600 serial manipulator, whose manufacturers claim that it is capable of to completing the standard test cycle in less than 500 ms. In this light the first candidate as motor type for the SMG is the AC motor of the Adept Servo Kit ([Adept Technology, Inc.](#), [Adept Technology, Inc.](#)). However, the specifications of the servomotors of the Adept Servo Kit were compared with those of the Yaskawa Sigma II AC motors, the Pacific Scientific PMA brushless servomotors and the Bayside BM brushless servomotors, as recorded in Table 11. The Yaskawa Sigma II SGMAH-08A characteristics are the same of those of the Adept AC; however the former has a better peak torque. Of the two DC brushless motors reported in Table 11, the Pacific Scientific PMA24 has a better maximum speed. The Yaskawa Sigma II SGMAH-08A is preferred to the Pacific Scientific PMA24 because it is an AC servo as the motors of the Adept Servo Kit (we recall that one of the guidelines is to design a robot with better performance than the Adept Cobra i600, described in Subsection 3.5.1.).

Numerical simulations of the SMG kinematics and dynamics, including the inertia of the custom-made drive, were run in order to predict the behaviour of the robot while performing the test cycle. The results showed that the robot should be capable to complete the test cycle in 400ms by imposing on its motors the speeds and torques<sup>1</sup> reported in Table 12. Comparing the values of Table 12 with the values of Table 11 associated with the Yaskawa Sigma II SGMAH-08A, one can infer that the selected motors can achieve the simulated performance. It is noteworthy that during the test cycle the motors will mostly operate in saturation, hence the non-availability of  $\tau_{rms}$  and  $n_{op}$  does not affect significantly their operation.

Once the motor is selected, the amplifier can be directly selected by entering a table of the servomotor manufacturer (Yaskawa in this case). The corresponding servo-amplifier is an SGDH-08AE-S. Of course, one can select another type of amplifier from another manufacturer; however, this solution was not considered in order to fully exploit the performance of the actuators.

### A.3 Gearhead Dimensioning

The selection of a suitable gearhead is the next step in the design of the actuation system of a robot. Knowing the desired speed reduction ratio  $i = 20$  (stemming from simulation results of the kinematics and dynamics of the SMG, one can derive the requirements to be met by the gearhead:

- the maximum output torque of the gearhead  $\tau_{Gmax}$  has to be greater than  $i\tau_{peak} = 142$  Nm;
- the maximum continuous torque of the gearhead  $\tau_{Gmaxcont}$  has to be greater than  $i\tau_{maxcont} = 48$  Nm;

<sup>1</sup>All the values are reduced to the motor shaft

PG	$i$	$e$ [%]	$I$ [kgm <sup>2</sup> ]	$F_{a,max}$ [N]	$F_{r,max}$ [N]	$\tau_{Gmax}$ [Nm]	$\tau_{Gmaxcont}$ [Nm]	$n_{Gmax}$ [rpm]	$n_{Gnom}$ [rpm]	$\tau_{sl,max}$ [Nm]
Bayside PS-90	20	94	$8.496 \times 10^{-6}$	600	1700	130	107	5300	3800	299
Parker GTN-115	20	> 95	$1.41 \times 10^{-4}$	12000	5000	260	520	8000	4000	260

Table 13: PG Comparison

- the maximum input speed of the gearhead  $n_{Gmax}$  has to be greater than  $n_{max} = 5000$  rpm; and
- the nominal input speed of the gearhead  $n_{Gnom}$  has to be greater than  $n_{nom} = 3000$  rpm.

Other important parameters to take into account in the gearhead selection are efficiency, radial and axial loads at the root of the output shaft, moment of inertia of the moving parts (a.k.a. moment of inertia of the PG), backlash and torsional stiffness.

Table 13 reports the characteristics of two different planetary gearheads, which are good candidates for the selected motors. We have indicated with  $i$  the speed reduction ratio, with  $I$  the moment of inertia of the PG reduced to the input shaft, with  $F_{a,max}$  the maximum axial load, with  $F_{r,max}$  the maximum radial load, with  $e$  the efficiency and with  $\tau_{sl,max}$  the maximum holding torque of the shaft-lock mechanism of the PG, which is intended to secure the motor shaft to the input shaft of the PG.

**Remarks:**

- $I$  of the Bayside PG was computed from the company catalog ([Bayside Controls, Inc.](#), [Bayside Controls, Inc.](#)):  $0.006 \text{ oz in sec}^2 = 8.496 \times 10^{-6} \text{ kgm}^2$ ,
- $F_{a,max}$  and  $F_{r,max}$  of the Bayside PG were computed at 29 mm from the flange and 5000 rpm ([Bayside Controls, Inc.](#), [Bayside Controls, Inc.](#)),
- $I$  of the Parker PG was computed from the catalog ([Parker Hannafin, Corp.](#), [Parker Hannafin, Corp.](#)):  $1.41 \times 10^{-4} \text{ kgm}^2$ ,
- $F_{a,max}$  and  $F_{r,max}$  of the Parker PG are the maximum values throughout the usable shaft length ([Parker Hannafin, Corp.](#), [Parker Hannafin, Corp.](#)),
- the  $\tau_{sl,max}$  of the Parker PG is higher than Bayside PGs, and
- the “Emergency Stop Output Torque”, worth 299 Nm for the PS-90, reported in ([Bayside Controls, Inc.](#), [Bayside Controls, Inc.](#)), is not to be confused with the maximum output torque (indicated as “maximum acceleration output torque” in ([Bayside Controls, Inc.](#), [Bayside Controls, Inc.](#))).

From the comparison table one can infer that

- the two PGs satisfy motor speed specs <sup>2</sup>,
- the efficiency is practically the same for the two PGs;
- the Bayside PG has a smaller  $I$  with respect to the Parker PG;
- the two PGs satisfy motor maximum continuous torque specs;
- the Parker PG, as opposed to the Bayside PG, does not need an extra support bearing to prevent excessive radial loads (below are given more details on this issue); and
- the Parker PG, as opposed to the Bayside PG, satisfies the motor peak torque specs (below are given more details on this issue).

<sup>2</sup>More specifically, the Bayside PG can sustain the  $n_{Gmax}$  for not more than one second. Given the simulation results and the cycle time (0.5 sec) of the application, the Bayside PG  $n_{Gmax}$  turns out to be acceptable.



In this light, the best solution is the Parker PG. However, the latter turns out to be much more expensive (the overall cost of for four PG would have increased by 64%) than the Bayside PG. Therefore, the final decision converged to the Bayside PG<sup>3</sup>. However, some important design warnings need to be given on three critical aspects associated with this selection:

- the actual braking torque measured at the input shaft of the gearhead cannot exceed 30 N;
- the actual output torque of the gearhead cannot exceed 133 Nm; and
- an extra support bearing needs to be used for limiting the radial load acting on the output shaft of the gearhead.

More on these last two important aspects can be found in the Subsections below.

### A.3.1 Maximum Output Torque

Taking into account also the efficiency of the PG we have that the  $\tau_{Gmax} = 130$  Nm of the Bayside PG is smaller than  $i\eta\tau_{peak} = 133$  Nm. In spite the foregoing relation is not satisfied, Bayside confirmed that the predicted value of 133 Nm is compatible with the gearhead specs.

### A.3.2 Extra Support for the Gearhead Pinion Shaft

The radial load  $F$  acting on the output shaft of the PG is mainly contributed by the torque transmitted by the pinion:

$$F = \frac{\tau \tan(\alpha) i \eta}{D_p/2} = [7.1 \times 20 \times 0.94 \times \tan(\pi \times 20/180)] / (0.057/2) = 1705 \text{ N}$$

where  $D_p = 57$  mm is the pitch diameter of the pinion,  $i = 20$  is the speed reduction ratio of the planetary gearhead,  $\eta = 94\%$  is the efficiency of the PG,  $\alpha = 20^\circ$  is the pressure angle of the pinion and  $\tau$  is the peak torque delivered at the output shaft of the motor. This value is greater than the maximum radial load at 29 mm from the flange of the PG (1700 N). In order to bring the value to specs, an extra support bearing need be added as far as possible from the flange of the PG, as depicted in Fig. 55, and proven with a simple stress analysis in the sequel.

With reference to Fig. 55, the dimension  $a$  depends on  $d_1$ ,  $d_2$  and  $d_3$ , while  $b$  depends on  $d_3$ ,  $d_4$ ,  $d_5$  and  $d_6$ .

### A.3.3 Reaction Forces

The shear force acting at the tip of the beam in Fig. 55 is given by

$$F = \frac{\tau \tan(\alpha) i e}{D_p/2}$$

where  $D_p$ ,  $i$ ,  $\eta$ ,  $\alpha$  and  $\tau$  were all defined above.

From Fig. 55 we have

$$\delta_C = 0 \quad v_C = 0, \tag{68}$$

---

<sup>3</sup>A remark on backlash and torsional stiffness issues is in order here: With a 10% of extra-cost factor we selected a low-backlash PG (6 arcmin instead of 8 arcmin, both measured at 2% of the rated torque). However, a warning is in order here: the SMG robot will operate in short-time (0.5 sec) and mostly at the maximum torque (133 Nm); as a consequence, the torsional displacements, estimated to be 10 arcmin for the given torsional stiffness, will dominate over the rigid displacements introduced by the backlash, thus limiting the benefits stemming from the low-backlash PG.

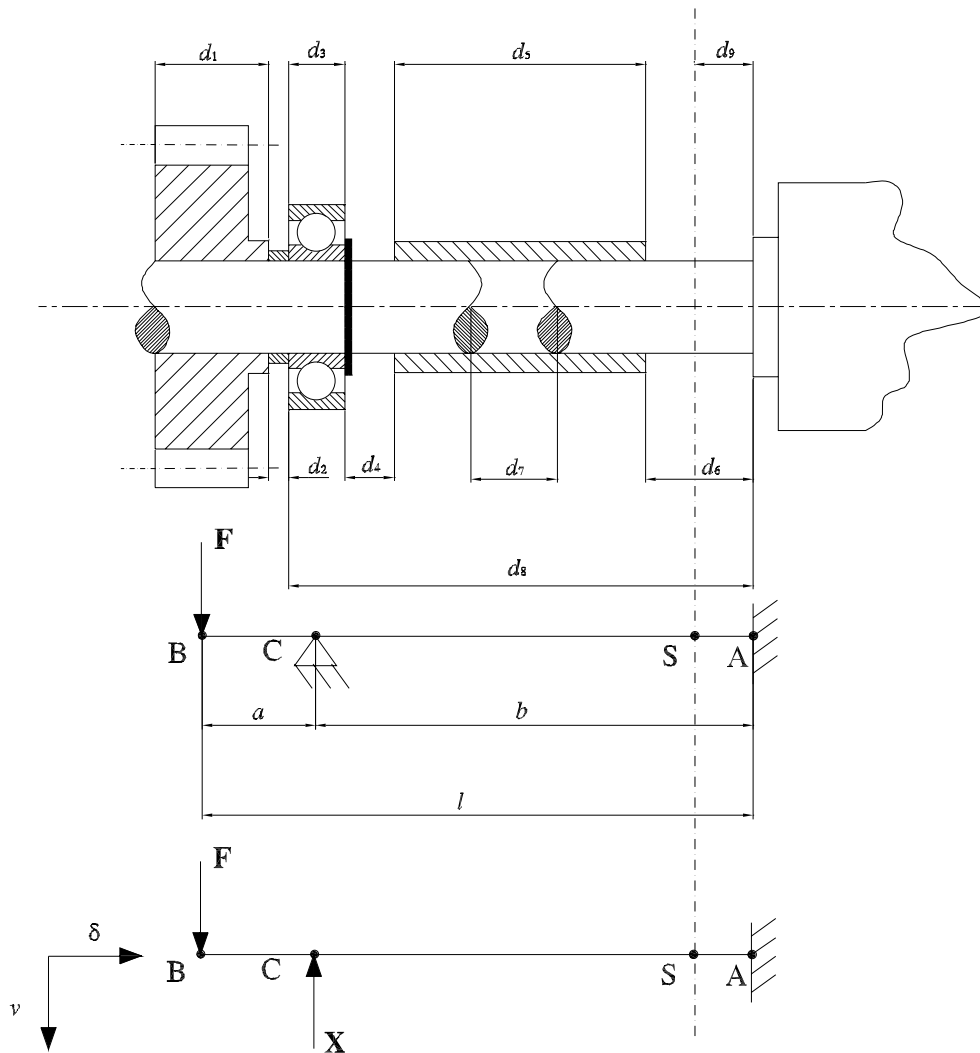


Figure 55: Design solution with bearing for the extra support of the output shaft of the PG

$d_1$	width of the pinion
$d_2$	axial distance between pinion and bearing
$d_3$	width of the bearing
$d_4$	axial distance between bearing and shaft coupler
$d_5$	length of the shaft coupler
$d_6$	distance between shaft coupler and the planetary gearhead (PG) flange
$d_7$	axial distance between the shafts
$d_8$	distance between pinion and PG
$d_9$	distance of the cross-section of interest

Table 14: Legend of Figure 55

where  $\delta_C = X_1 b / EA$ , where  $A$  is the cross-section area and  $E$  is the Young modulus of the output shaft of the PG. From the first of eqs. (68) we have

$$\delta_C = X_1 b / EA = 0 \Rightarrow X_1 = 0$$

Moreover, we have that the contribution of the force  $F$  to the vertical displacement  $v_C^F$  of section  $C$  is

$$v_C^F = \frac{F a^3}{6EI} - \frac{F l^2 a}{2EI} + \frac{F l^3}{3EI}$$

where  $I = \pi r^4 / 4$  and  $r$  is the radius of the PG output shaft, while that of force  $X$ ,  $v_C^X$ , is

$$v_C^X = -\frac{X b^3}{3EI}$$

Therefore,

$$v_C = v_C^F + v_C^X = \frac{F a^3}{6EI} - \frac{F l^2 a}{2EI} + \frac{F l^3}{3EI} - \frac{X b^3}{3EI}.$$

From the second of eqs. (68) we have

$$\frac{F a^3}{6EI} - \frac{F l^2 a}{2EI} + \frac{F l^3}{3EI} - \frac{X b^3}{3EI} = 0,$$

which yields

$$X = \left( \frac{F a^3}{6EI} - \frac{F l^2 a}{2EI} + \frac{F l^3}{3EI} \right) \frac{3EI}{b^3} = \frac{3F}{b^3} \left( \frac{a^3}{6} - \frac{l^2 a}{2} + \frac{l^3}{3} \right) = \frac{3F}{b^3} \left( \frac{a^3 - 3l^2 a + 2l^3}{2} \right).$$

#### A.3.4 Bending Moment and Shear Analysis

The contribution of force  $F$  to the bending moment of the structure at hand is given by

$$M^F(\sigma) = F\sigma$$

while the contribution of the reaction force  $X$  is

$$M^X(\sigma) = X(\sigma - a) \quad \text{for } \sigma \geq a$$

and for  $\sigma < a$ ,  $M^X(\sigma) = 0$ .

Therefore, the overall bending moment acting on the structure is

$$M(\sigma) = M^F(\sigma) + M^X(\sigma) = X(\sigma - a) - F\sigma = (X - F)\sigma - Xa \Rightarrow M(\sigma) = R_A \sigma - Xa \quad \text{for } \sigma \geq a.$$

where  $R_A$  is the reaction force estimated at Section A, while, for  $\sigma = \sigma^*$ , we have  $M(\sigma) = 0$ , with  $\sigma^* = Xa / R_A$ . Moreover,

$$M(l) = R_A l - Xa.$$

The diagram of the bending moment acting on the structure is given in Fig. 56a and can be computed as the algebraic sum of the diagrams of Figs. 56b and 56c.

Moreover, a Matlab algorithm was coded, and included in the Appendix, for

- The analysis, at the two boundary values 0.088 mm and 0.093 mm, of the bending moment at 29 mm from the flange of the PG upon varying the position  $a$  of the extra-support bearing — see Fig. 57 for the results.

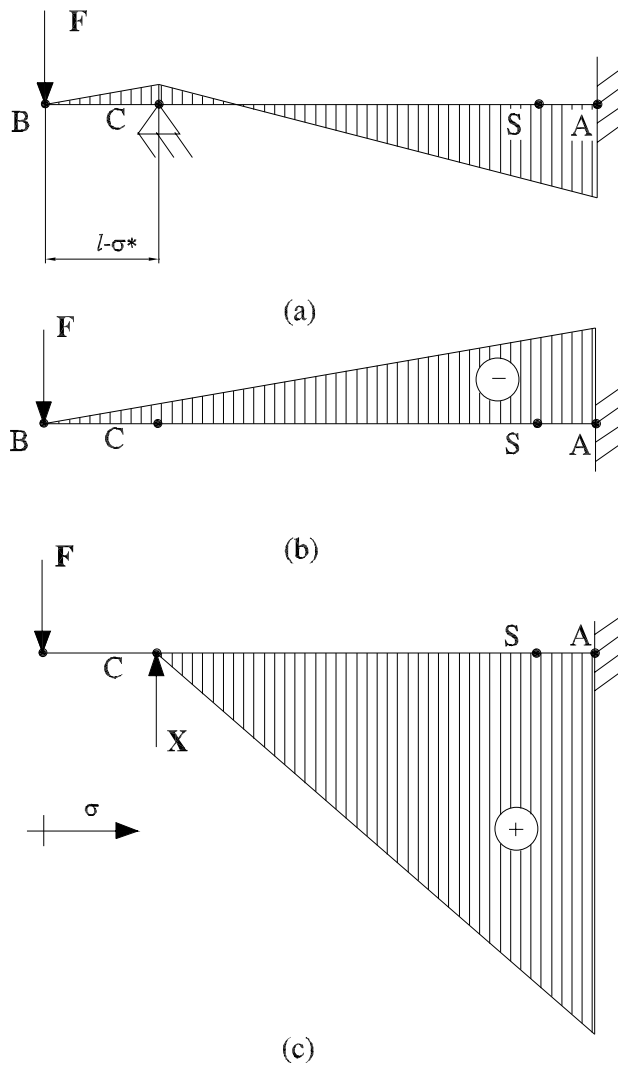


Figure 56: Bending moment diagram: (a) contribution of  $F$ , (b) contribution of  $X$

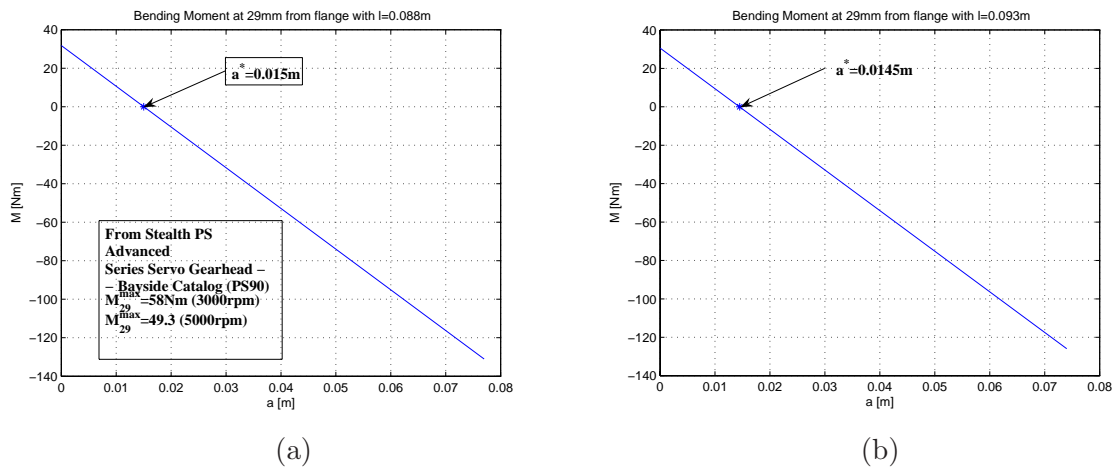
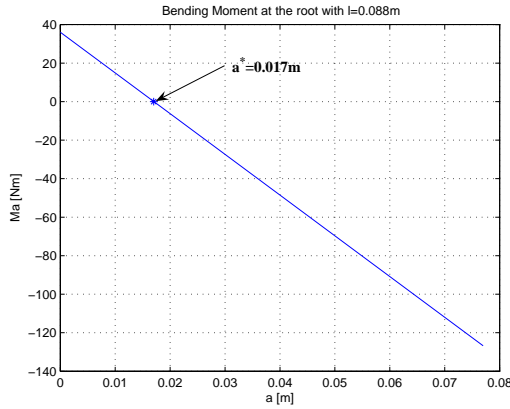
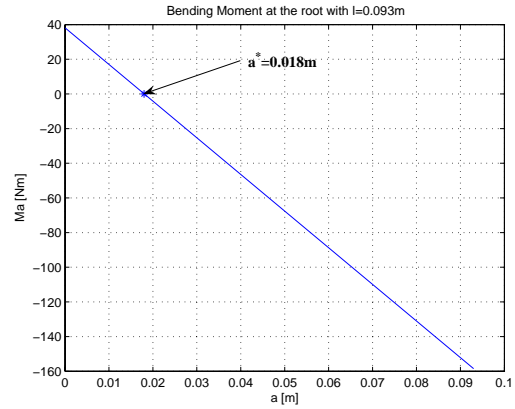


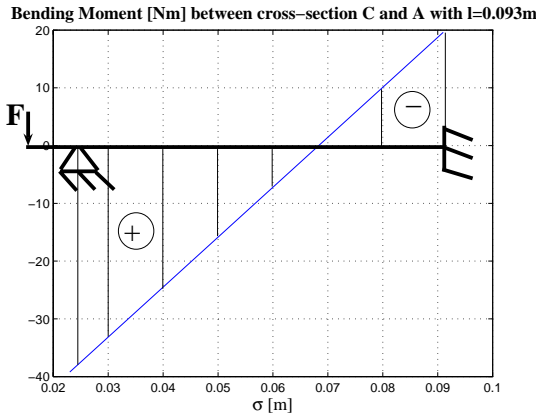
Figure 57: Bending moment at 29 m from the flange, with: (a)  $l = 0.093\text{m}$ ; (b)  $l = 0.093$



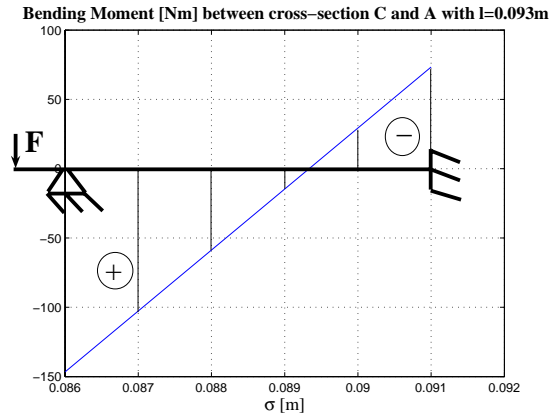
(a)



(b)

Figure 58: Bending at the root for: (a)  $l = 0.088$  m; (b)  $l = 0.093$  m

(a)



(b)

Figure 59: Bending moment between sections A and C: (a) with  $d_2 = 0.002$  m (b)  $d_2 = 0.065$  m

- The analysis, at the two boundary values 0.088 mm and 0.093 mm, of the bending moment at the root of the PG shaft upon varying the position  $a$  of the extra-support bearing — see Fig. 58 for the results.
- The analysis, for  $l = 0.093$  mm, of the bending moment diagram of the PG shaft locating the extra-support bearing as far as possible from the flange of the PG ( $d_2 = 0.002$  mm) — see Fig. 59a for the results.
- The analysis, for  $l = 0.093$  mm, of the bending moment diagram of the PG shaft locating the extra-support bearing as close as possible to the flange of the PG ( $d_2 = 0.065$  mm) — see Fig. 59b for the results.

As we can see from the foregoing results, the bending moment increases with roughly the same derivative for both boundary values of  $l$ . Moreover, the closer the extra-bearing is to the flange, the higher the bending moment throughout the portion of the shaft between sections  $C$  and  $A$ . In this light, the extra-bearing has to be located as far as possible to the flange of the PG.

Moreover, as we can see from Fig. 60, that the closer the extra-bearing is to the flange, the higher shear stress throughout the portion of the shaft between sections  $C$  and  $A$ .

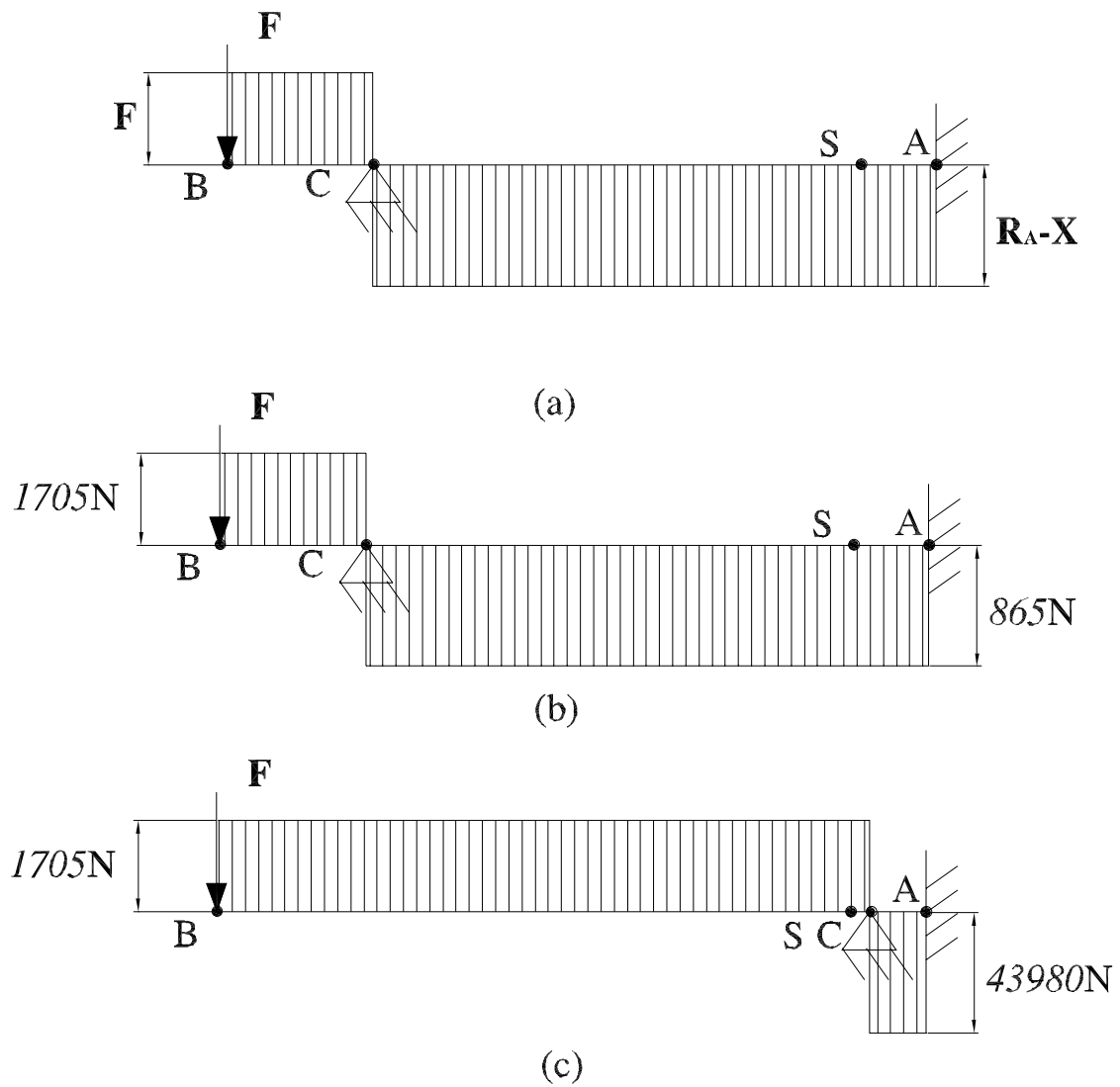


Figure 60: Shear stress distribution: (a) general scheme; (b) with  $d_2 = 0.002$  m; and (c)  $d_2 = 0.065$  m

## A.4 Motor Starter Design and Testing

### A.4.1 Background Material

**Motor Starters** A motor starter is the simplest form of motor controller and is capable of starting/stopping the motor and providing it with overload protection (Traister, 1994).

Manual starters are used mostly on small machine tools, pumps/compressors, conveyors, fans and blowers. They are lowest in cost of all motor starters, have simple mechanisms, and provide quiet operation with no direct electric-magnetic field coupling (a.k.a. AC hum). The contact, however, remains closed and the lever stays in the “ON” position in the event of a power failure, causing the motor to restart automatically when the power returns. Therefore, *low-voltage protection*<sup>4</sup> and *low-voltage release*<sup>5</sup> are not possible with these manually operated starters. However, this action is an advantage when the starter is applied to motors that should run continuously (Traister, 1994).

Fractional-horsepower manual starters are designed to control and provide overload protection for motors of 1 hp or less on 120 – 240 V single-phase circuit. They are available in single and two-pole versions and are operated by a toggle-handle on the front. When a serious overload occurs, the thermal units “trips” to open the starter contacts, disconnecting the motor from the line. The contacts cannot be reclosed until the overload relay has been reset by moving the handle to the full “OFF” position, after allowing about two minutes for the thermal unit to cool. The open-type starter will fit into a standard outlet box and can be used with standard flush plate (Traister, 1994).

The integral-horse power manual starter is available in two and three-pole versions to control single-phase motors up to 5 hp and polyphase motors up to 10 hp, respectively. Two-pole starters have one overload relay and three-pole starters usually have three overload relays. Integral-horsepower manual starters work as fractional-horsepower manual starters. However, integral-horsepower manual starters with low-voltage protection prevent automatic start-up of motors after a power loss. This is accomplished with a continuous solenoid which is energized whenever the line-side voltage is present. If the line-voltage is lost or disconnected, the solenoid deenergizes, opening the starter contacts. The contact will not automatically close when the voltage is restored to the line. To close the contacts, the device must be reset manually. This manual starter will not function unless the line terminals are energized. This is a safety feature that can protect personnel or equipment from damage and is used on such equipment as grinders, metalworking machinery, mixers, woodworking machinery, and whenever standards require low-voltage protection (Traister (1994)).

#### Magnetic Motor Starters

Magnetic motor starters, a.k.a. magnetic contactors, use electromagnetic energy for closing switches. The electromagnet consists of a coil of wire placed on an iron core. When current flows through the coil, the iron of the magnet becomes magnetized, attracting an iron bar called the *armature*. When a controller armature has been sealed-in, it is held closely against the magnet assembly. However, a small gap is always deliberately left in the iron circuit. When the coil becomes deenergized, some magnetic flux (residual magnetism) always remains, and if it were not of the gap in the iron circuit, the residual magnetism might be sufficient to hold the armature in the sealed-in position (Traister, 1994).

The shaded-pole principle is used to provide a time delay in the decay of flux in the DC coils, but is used more frequently to prevent chatter and wear in the moving parts of AC magnets. A shading-coil is a single turn of conducting material mounted in the face of the magnet assembly or armature. The alternating main magnetic flux induces currents in the shading coil; these currents set up an auxiliary magnetic flux which is out of phase from the main flux. The auxiliary flux produces a magnetic pull out of phase from the pull due to the main flux, which keeps the armature sealed in when the main flux fails to zero (which occurs 120 times per second with 60 Hz AC) . Without the shading coil, the armature

---

<sup>4</sup>Low-voltage protection means that in the case of a power loss the motor starter will not close automatically when power returns.

<sup>5</sup>Low-voltage release means that in the case of power loss the magnetic starter will open-up.

<b>Protection against:</b>	Overload protection	Protection against shorts
<b>Equipment :</b>	Time-delay fuse or overload relay	Fast-acting fuse
<b>Selection Parameter:</b>	Motor full-load current	Motor in-rush current

Table 15: Type of equipment and selection parameters for overload and short-circuit protection

would tend to open each time the main flux goes through zero, see Fig. 61(a). As a consequence, excessive noise, wear on magnet and heat would result (Traister, 1994).

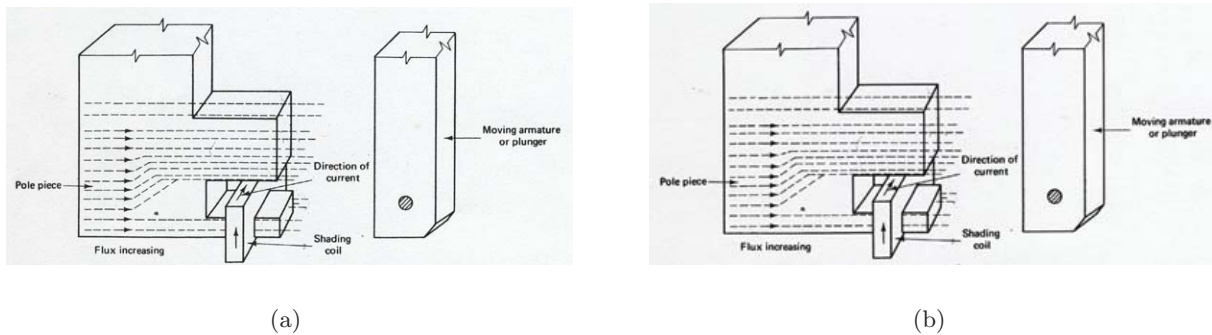


Figure 61: Section of pole face with current in (a) clockwise and (b) counterclockwise direction

### Overload Protection

Overload relays are the heart of motor protection. They have inverse-trip time characteristics, permitting them to hold in during the accelerating period (when in-rush current is drawn), yet providing protection on small overloads above the full-load current when the motor is running. Unlike dual-element fuses, overload relays are renewable and can withstand repeated trips and reset cycles without need of replacement. Overload relays cannot, however take the place of fuses<sup>6</sup> (Traister, 1994). A summary on dimensioning of overload and fuses is reported in Table 15.

Overload relays can be classified as being either thermal or magnetic. Magnetic overload relays react only to current excesses and are not affected by temperature. A magnetic overload relay has a movable magnetic core inside a coil which carries the motor current. The flux set up inside the coil pulls the core upward. When the core rises far enough it trips a set of contacts on the top of the relay. Thermal overload relays rely on the rising temperature caused by the current to trip the overload mechanism. The latter can be further subdivided into two types: melting alloy and bimetallic. Standard overload relay contacts are closed under normal conditions and open when the relay trips. An alarm signal is sometimes required to indicate when a motor has stopped due to an overload trip. Also, with some machines, particularly those associated with continuous processing, it may be required to signal an overload condition rather than have the motor and process stop automatically. This is done by fitting the overload relay with a set of contacts that close when the relay trips, completing the alarm circuit. These contacts are appropriately called alarm contacts (Traister, 1994).

### Control Relays

A relay is an electromagnetic device whose contacts are used in control circuits of magnetic starters, contactors, solenoids, timers and other relays. They are generally used to amplify the contact capability

<sup>6</sup>Fuses are not designed to provide overload protection. Their basic function is to protect against short circuits. Motors draw a high in-rush current between this temporary and harmless in-rush current and a damaging overload. Such fuses, chosen on the basis of motor full-load current, a.k.a. rated current, would “blow” every time the motor is started. On the other hand, if a fuse were chosen large enough to pass the starting current or inrush current, it would not protect the motor against small, harmful overloads that might occur later. Dual-element or time-delay fuses can provide motor overload protection but suffer the disadvantage of being nonrenewable and must be replaced.



or multiply switching functions of a pilot device<sup>7</sup>. A control relay can be used for current amplification or voltage amplification.

### **Canadian Electrical Code and Québec Amendments**

With minor exceptions, the Canadian Electrical Code (CEC) along with the Québec Amendments require a disconnect means for every motor. A combination starter consists of an across-the-line starter and a disconnect means wired together in a common enclosure. The starter may be controlled remotely with push-buttons, selector switches, and the like, or these devices maybe installed in the cover. The single device makes a neat as well as compact electrical installation that takes little mounting space. A combination starter provides safety for the operator, because the cover of the enclosing case is locked with an external operating handle [Traister \(1994\)](#).

**Guarding (Rule 28-012)** Exposed live parts of motors and controllers operating at 50V more between terminals shall be guarded against accidental contact by means of enclosures or by location.

**Methods of Guarding (Rule 28-014)** Acceptable methods of guarding of motors having exposed live parts are by [QEC \(1992\)](#):

- installation in a room or enclosure which is accessible only to authorized persons; or
- installation on a suitable balcony, gallery, or platform elevated and arranged so as to exclude other than qualified persons; or
- elevation by 2.5 m or more above the floor; or
- Guard rails if the motor operates at 750V or less.

**Remote Control Circuit** A remote control circuit is any electrical circuit which controls any other circuit through a relay or any equivalent device [QEC \(1992\)](#).

**Stationary Motors (Rule 28-100)** The wiring method of stationary motors shall be in accordance with the applicable requirements of Section 12 “Wiring Methods” and 36 “High Voltage Installations” of [QEC \(1992\)](#).

**Classifications (Section 16) of QEC (1992)** Circuits covered by this section are the portion of the wiring system between the load side of the *overcurrent device*<sup>8</sup> or the power-limited supply and all connected *equipment*<sup>9</sup>, and shall be classified as follows [QEC \(1992\)](#):

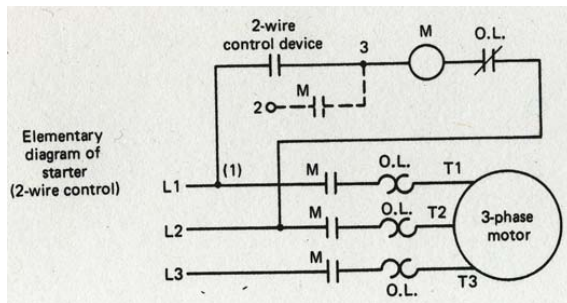
- a) Class 1 - Circuits which are supplied from sources having limitations in accordance with Rule 16-100.
- b) Class 2 - Circuits which are supplied from sources having limitations in accordance with Rule 16-200.

---

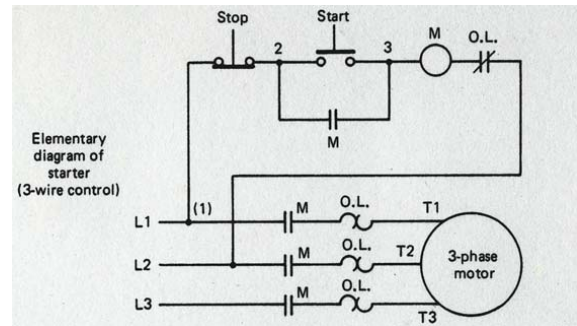
<sup>7</sup>Pilot devices control certain operations of the circuit; they can consist of push buttons, limit switches, flow switches, temperature switches and pressure switches.

<sup>8</sup>An overcurrent device is a device affording protection from excess current, but not necessarily short-circuit protection, and capable of automatically opening an electric circuit either by fusing of metal or by electro-mechanical means [QEC \(1992\)](#).

<sup>9</sup>Electrical equipment means any apparatus, appliance, device, instrument, fitting fixture, machinery, material, or thing used in or for, or capable of being used in or for, the generation, transformation, transmission, distribution, supply, or utilization of electric power or energy, and without restricting the the generality of the foregoing includes any assemblage or combination of materials or things which is used, or is capable of being used or adapted, to serve or perform any particular purpose or function when connected to an electrical installation, notwithstanding that any of such materials or things may be mechanical, metallic, or non-electric in origin [QEC \(1992\)](#).



(a)



(b)

Figure 62: Elementary diagram of: (a) two-wire and (b) three-wire motor control.

**Extra-Low-Voltage Power Circuits (Rule 16-004)** Circuits which are neither remote-control circuits nor signal circuits, but which operate at not more than 30 V where the current is not limited in accordance with Rule 16-200 and which are supplied from a transformer or other device restricted in its rated output to 1000 VA, shall be classed as extra-low-voltage power circuits and shall be considered to be class 1 circuits [QEC \(1992\)](#).

**Low-Energy Power Circuits (Rule 16-006)** Circuits which are neither remote-control circuits nor signal circuits but in which the current is limited in accordance with Rule 16-200, shall be classed as low energy power circuits and shall be considered to be Class 2 circuits [QEC \(1992\)](#).

### Limitations of Class 1 Circuits

- 1) Class 1 extra-low-voltage power circuits shall be supplied from a source having a rated output of not more than 30 V and 1000 VA.
- 2) Class 1 remote-control and signal circuits shall be supplied by a source not exceeding 600 V.

**Other Rules of Interest** Other rules of interest are 12-020 and 14-508 of [QEC \(1992\)](#).

### Two-Wire Control

Figure 62a shows the wiring diagram for a two-wire control circuit. The control itself could be a thermostat, float switch, limit switch, or other maintained contact device to the magnetic starter. When the contacts of the control device close, they complete the coil circuit of the starter, causing it to pick up and connect the motor to the lines. When the control device contacts open, the starter is deenergized, stopping the motor. Two-wire control provides low-voltage release but not low-voltage protection. When wired as illustrated, the starter will function automatically in response to the direction of the control device, without the attention of an operator. In this type of connection, a holding circuit is not necessary [Traister \(1994\)](#).

### Three-Wire Control

A three-wire control circuit uses [Traister \(1994\)](#):

- momentary contacts,
- start-stop buttons and
- a holding circuit interlock wired in parallel with the start button to maintain the circuit.

Figure 62b shows the wiring diagram for a three-wire control circuit. Pressing the normally open (NO) start button completes the circuit to the coil. The power circuit contacts in lines 1, 2 and 3 close, completing the circuit to the motor, and the holding circuit contact also closes. Once the starter has picked up, the start button can be released, as the now-closed interlock contact provided an alternative current path around the reopened start contact. Pressing the normally closed (NC) stop button will open the circuit to the coil causing the starter to drop out. An overload condition, which caused the overload contact to open, a power failure, or a drop in voltage to less than the seal-in value would also deenergize the starter. When the starter drops out, the interlock contact reopens, and both current paths to the coil, through the start button and the interlock, are now open. Since three wires from the push-button station are connected into the starter at points 1, 2 and 3, this wiring scheme is commonly referred to as *three-wire control*. The holding circuit interlock is a normally open auxiliary contact <sup>10</sup> provided on standard magnetic starters and contactors. In addition to the main power contacts, which carry the motor current, and the holding circuit interlock, a starter can be provided with externally attached auxiliary contacts, commonly called electrical interlocks. Both NO and NC versions are available. Among a wide variety of applications, interlocks can be used to control other magnetic devices where sequence operation is desired, to electrically prevent another controller from being energized at the same time, and to make and break circuits to indicating or alarm devices such as pilot lights, bells, or other signals Traister (1994).

### Circuit Breakers

Functionally, circuit breakers serve as disconnecting means and as protective devices. Compared with switches, they possess much higher interrupting ability. Circuit breakers are equipped with automatic overcurrent trips which open the breaker if the current through it exceeds the trip setting. They are designed to interrupt overload and fault current which exceed the operating overload which motor starters are expected to handle. The primary purpose of circuit breakers as part of controllers is to protect against damage resulting from short circuits. Selection of circuit breakers for any installation is based not only on the continuous current rating of the breaker but also on the interrupting capability. The latter must be at least as great as the largest fault current the system can produce at the point of breaker installation. Selection of circuit breakers is governed by analysis of the power system rather than motor performance. The functions of circuit breakers and motor starters in a controller should not be confused. Starters are designed for frequent operations and for interruption of motor load and operating overloads. Circuit breakers stay closed for long periods of time, but they must be relied upon to trip and clear the system promptly when unusual overload or fault condition occurs. While mechanical life of motor starters is measured in terms of millions of operations, that of circuit breakers is measured in terms of thousands of operations. Under certain conditions, circuit breakers may be used as motor starters. For very large motors and for voltages above 5000 V, starters are not available. Such large motors, for instance, for driving motor generator sets, pumps, compressors, fans, and the like, are never started frequently Heumann (1961). **Fuses**

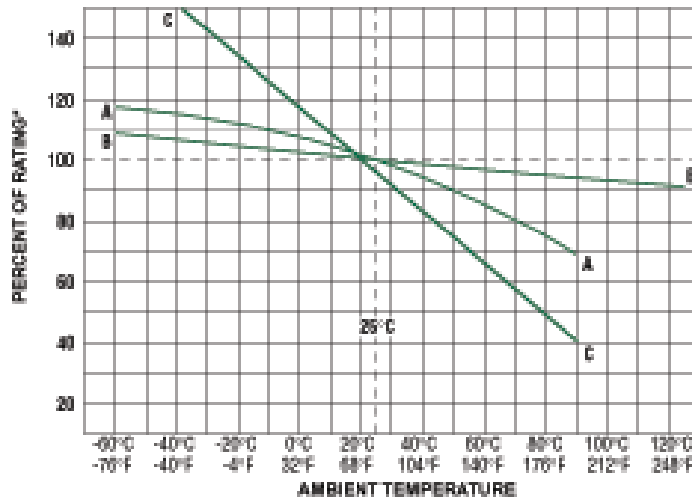
Fuses are protective devices that act as conductors in an electrical circuit. When an overload or short-circuit current exceeds a fuse's continuous-current rating, the fuse will stop the flows of the current to protect equipment and personnel. Overload currents typically are up to 10 times larger than the fuse's continuous-current rating and occur when the equipment draws more current than it needs. Short circuits are greater than 10 times the fuse's continuous-current rating and occur when the current finds a "shortcut" outside its normal path. A few definitions are needed before outlining the fuse dimensioning methodology:

**Time-delay fuses:** these fuses delay opening on low-level overloads until the overload has been sustained for a specific amount of time. This prevents the fuse from blowing when exposed to harmless temporary overload currents such as motor start-ups and switching surges. Certain time-delay fuses are also known as dual-element fuses McMaster-Carr (2005).

---

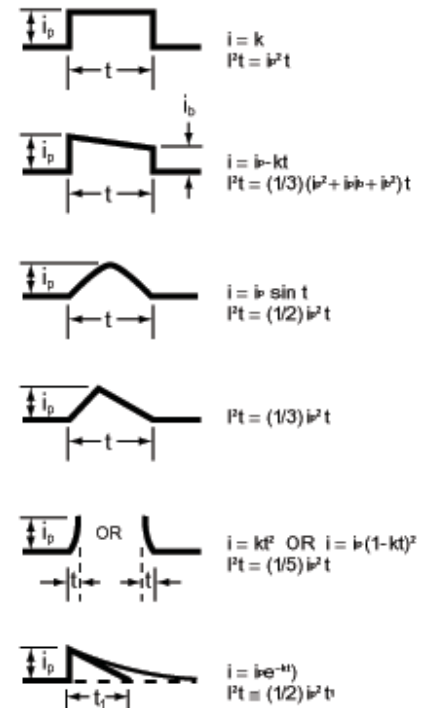
<sup>10</sup>An auxiliary contact is a contact circuit device that uses a small current to modify its default state.

Curve A: Thin-Film Fuses and 313 Series (.010 to .150A)  
 Curve B: Very Fast-Acting, Fast-Acting, and Spiral Wound Slo-Blo® Fuses  
 Curve C: Resettable PTC's



\*Ambient temperature effects are in addition to the normal derating, see example.

(a)



(b)

Figure 63: (a) Fuse temperature diagram; (b)  $I^2t$  energy associated to a specific waveform.

**Fast-acting fuses:** these fuses do not have a time-delay opening. Use them when temporary overload currents are not present [McMaster-Carr \(2005\)](#).

**Continuous-current rating, a.k.a. nominal current rating:** the maximum current that a fuse carries under normal conditions.

**Interrupting rating, a.k.a. breaking capacity:** the maximum current that a fuse can safely stop in the event of a short-circuit [Littelfuse \(2005\)](#).

**Nominal melting energy:** it is a measure of the energy required to melt the fusing element and is expressed as Ampere Squared Seconds ( $A^2s$ ). The nominal melting energy is a value which is constant for each fusing element [Littelfuse \(2005\)](#).

**Rerating:** For 25°C ambient temperatures, it is recommended that fuses be operated at no more than 75% of the nominal current rating established using the controlled test conditions. These test conditions are part of UL/CSA/ANCE (Mexico) 248-14 Fuses for Supplementary Overcurrent Protection whose primary objective is to specify common test standards necessary for the continued control of manufactured items intended for protection against fire, etc. The purpose of the controlled test conditions is to enable fuse manufacturers to maintain unified performance standards for their products. However, the fuse selection process has to take into account the variable conditions of the specific application. In order to guarantee a trouble-free and long-life fuse protection, it is crucial to compensate for the foregoing variable conditions by generally loading the fuse with not more than the 75% of the nominal rating listed by the manufacturer, keeping in mind that overload and short-circuit protection must be adequately provided for. Fuses are generally temperature-sensitive devices whose ratings have been established in a 25°C ambient. The fuse temperature generated by the current passing through the fuse increases or decreases with ambient temperature change. The ambient temperature chart in Fig. 63a illustrates the effect that ambient temperature has on the nominal current rating of a fuse [Littelfuse \(2005\)](#).

There are several factors which affect fuse selection, namely [Littelfuse \(2005\)](#)

- 1) normal operating current, which has to be smaller than 75% of the nominal current rating of the fuse.
- 2) application voltage (AC or DC), which has to be smaller than the nominal voltage of the fuse.
- 3) ambient temperature, which needs to be accounted for by means of derating.
- 4) overload current and length of time in which the fuse must open: time-current curves should be consulted to try to match the fuse characteristic to the circuit needs, while keeping in mind that the curves are based on average data.
- 5) maximum available fault current, which has to be smaller than the interrupting rating of the fuse.
- 6) high-energy current pulses, such as surge currents, inrush currents, start-up currents, and circuit transients, whose  $I^2t$ -energy (see Fig.63b) has to be smaller than the nominal melting energy of the fuse.
- 7) physical size limitations, such as length, diameter, or height,
- 8) agency approvals required, such as UL, CSA, VDE, or Military,
- 9) considerations: mounting type/form factor, ease of removal, axial leads, visual indication, etc.
- 10) fuseholder features: clips, mounting block, panel mount, PC board mount, R.F.I. shielded, etc.

### Fuseholders

In many applications, fuses are installed in fuseholders. For 25°C ambient temperatures, it is recommended that fuseholders be operated at no more than 60% of the nominal current rating established using the controlled test conditions specified by Underwriters Laboratories [Littelfuse \(2005\)](#).

#### A.4.2 Wiring Scheme

The wiring diagram of the motor starter of the SMG robot is reported in Fig. 64. The latter complies with CEC norms and regulations and successfully interfaces the four 220 Vac split phase power cables and the SMG power amplifiers in the respect of guidelines and specifications provided in the manual [Yaskawa Electric America, Inc. \(2005\)](#). More specifically the circuit outlined in Fig. 64 is a Class 1 remote-control circuit, in the wording of the CEC [QEC \(1992\)](#), supplied by a source of 220 V not exceeding 600 V. All components have their chassis ground points tied together at a single point. This point is connected with a single conductor to an earth ground. This prevents ground loops and insures that all components are properly grounded against shock hazard [Leang \(2002\)](#).

**Remark:** The schematics of Fig. 64 needs to be integrated with a control relay with contact voltage of 220 V and coil voltage of 24 VDC with two NO and two NC contacts, namely a DILER-22-G(24VDC) (supplied standard with a resistor/diode combination surge suppressor) from Moeller Electric Corporation. The coil of the latter will be connected to the positive terminal of an external 24 VDC and to the *ALM+* (CN1-31 port of the CN1 connector of the Yaskawa servo amplifier). One of the NO contacts of the foregoing control relay needs to be connected in series with the Emergency-stop pushbutton of Fig. 64. While the one of the NC contacts of the foregoing control relay needs to be connected in series with the pilot light of Fig. 64. Only two DILER-22-G(24VDC) will be needed to complete the servo alarm circuit of the SMG robot (for more details see "Signal Connectors" Section further below). Note that this solution complies with the CEC, since if there is a power failure on the external 24 VDC power supply the pilot light will turn on and at the same time the MC will trip. In this light the new wiring scheme would be the one indicated in Fig. 65<sup>11</sup>

---

<sup>11</sup>This wiring scheme does not include the wiring of the motor braking system power supply, which needs to be implemented in order to release the brakes [Yaskawa Electric America, Inc. \(2005\)](#). Please note also that the wiring scheme in Fig. 65 is

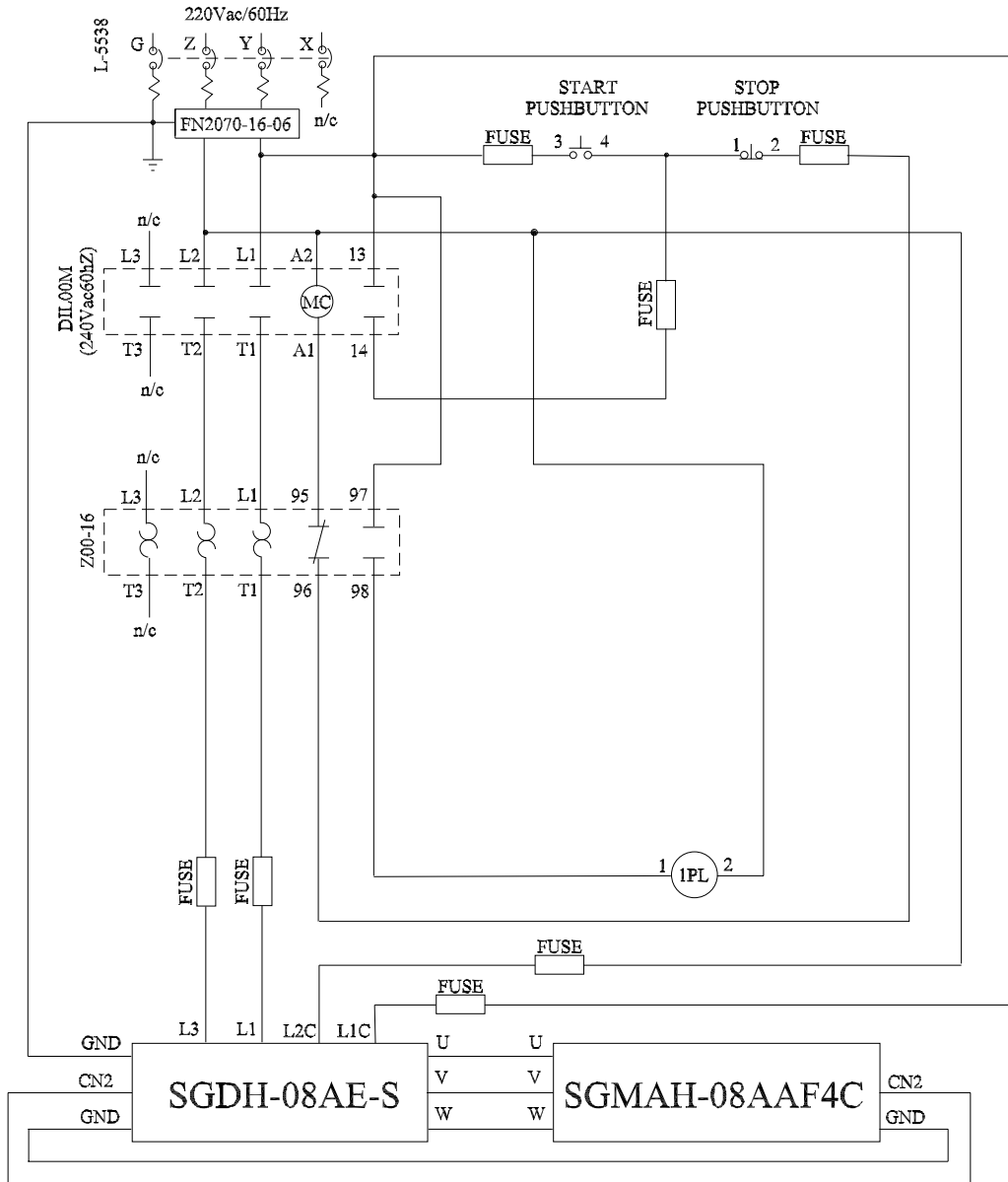


Figure 64: SMG parallel manipulator — Motor starter wiring diagram

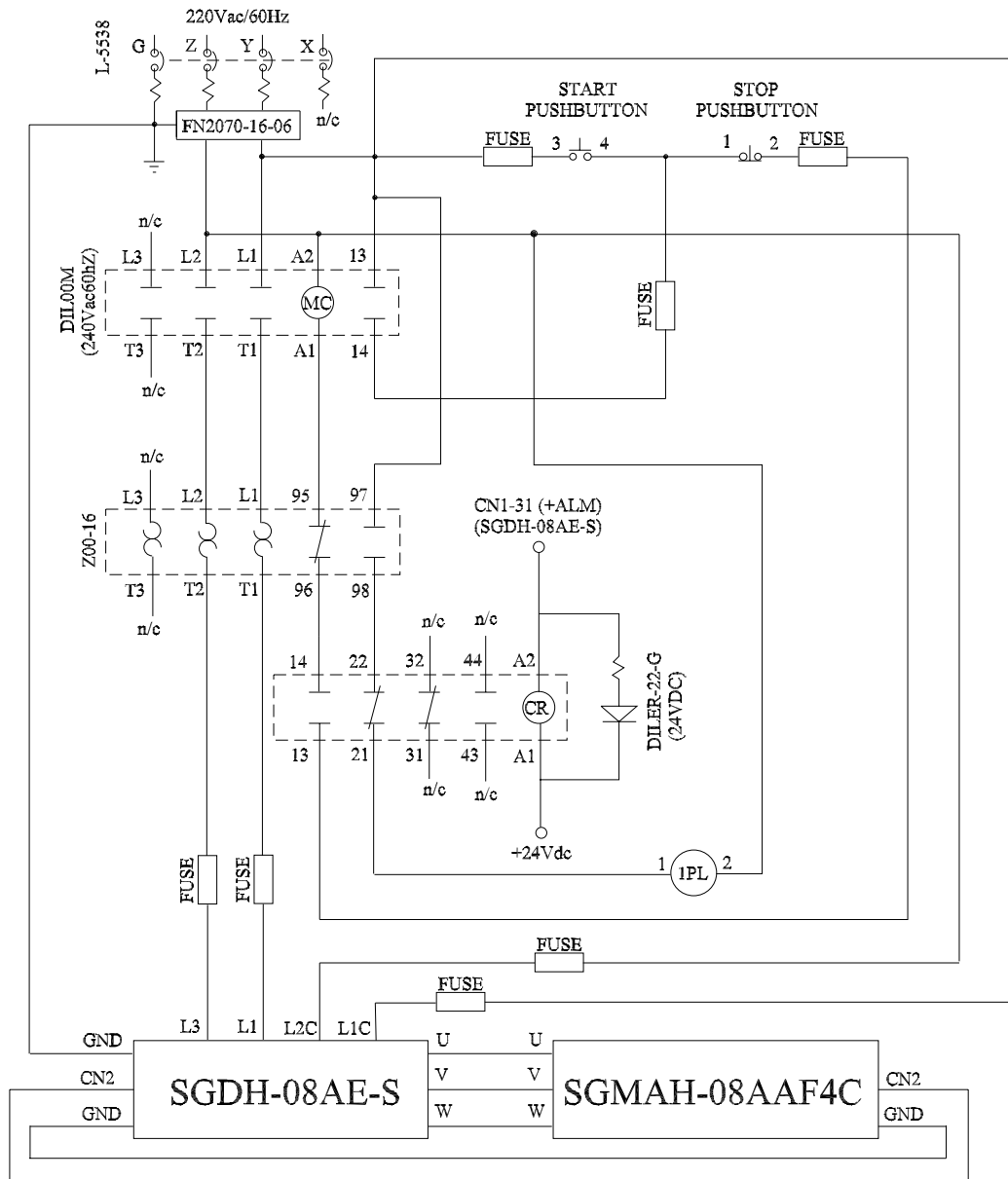


Figure 65: SMG parallel manipulator — Motor starter wiring diagram (with Servo Alarm)

### A.4.3 Component Dimensioning

#### A.4.4 Power

Power for the system is provided via two different sources. The most important consists of four 220 VAC split-phase<sup>12</sup> power cables. Each of the four 220 split-phase cables is connected to a servo amplifier, with appropriate power-switch equipment. An illustration of how power-related connections should be set-up on an individual servo amplifier can be found in Fig. 65.

A 24VDC “wall wart” is used to provide power to a number of signal lines leading to or from the SGDH servo amplifier. This DC power supply is connected to a regular 110 VAC outlet. **Circuit Breaker** The rated current and voltage of the power amplifier, an AC servo from Yaskawa (part number (p/n): SGDH-08AE-S) are 11 A and 220 V, respectively [Yaskawa Electric America, Inc. \(2005\)](#). Using a safety factor of 1.8, one can select a 220/240 V circuit breaker rated at 20 A, with a breaking capacity of 10.000 A. The circuit breaker has to be of the two-pole type in order to act as a stand-alone disconnecting means for each of the 220 V AC lines<sup>13</sup>. In light of the above four circuit breakers from Siemens (p/n: L5538) were selected and installed in the Robotic Mechanical Systems Laboratory of McGill University, site of installation of the SMG robot. Each of this circuit breaker features a breaking capacity of 10.000 A which is mainly justified by the type of power system rather than motor performance. **Motor Starter Design** A custom-made motor starter was designed and implemented for the McGill SMG robot, although many commercial off the shelf (COTS) motor starters are available on the market, such as the 129-0, 240 V power contactor unit from Phason Electronic Control Systems [Phason Electronic Control Systems \(2004\)](#), the PKZ 2-SP, self-protected combination starter from Moeller Electric Corp. [Moeller Electric Corp. \(2003a\)](#) or the KWIK Starter from [Sprecher+Schuh \(Sprecher+Schuh\)](#). The advantage of a custom-made motor starter is modularity for the design, cost-effectiveness and last but not the least clear understanding of the system functioning, which enhances safety (as opposed to “black-box” approaches which mask several physics phenomena).

**Noise Filter** A noise suppression filter was used to prevent noise generated by the power supply line. The filter also helps to reduce the amount of noise generated by the amplifier that are transferred to the power line. The noise filter was installed on the power line since other peripheral equipment are connected to the same line. In order to obtain best results with respect to a potential incorrect application of the noise filter, the following guidelines were followed [Leang \(2002\)](#):

- the input lines were separated from the output lines,
- the input and output lines were not put in the same duct or bundle them together,
- the noise filter ground was isolated from the output lines,
- the noise filter ground wire, output lines and other signal lines were not bundled (installed) together (in the same duct),
- the noise filter ground wire was connected directly to the ground plate, and

---

only for one servo, however it can be extended to the other three servos. In this regard, all the equipment necessary to complete the wiring of the other three servo has already been dimensioned, selected, ordered, please see bill of materials in the Appendix.

<sup>12</sup>The Yaskawa documentation refers to the power lines as “single phase”. Discussions with technical staff at Yaskawa revealed that they actually meant “split-phase”; that is, two in-phase 110 VAC lines connected in series to form 220 VAC, with a neutral line connected between them. It is important that this neutral line **not** be used as the ground reference. More information on split-phase power can be found at [http://www.allaboutcircuits.com/vol\\_2/chpt\\_10/1.html](http://www.allaboutcircuits.com/vol_2/chpt_10/1.html).

<sup>13</sup>We recall that the SMG robot draws power from four (one for each servo) independent 220 V AC split-phase lines.



- being the noise filter located inside an enclosure, its ground wire and the ground wires from other devices were connected to the ground plate of the enclosure first and then grounded.

The noise filter recommended by Yaskawa is the Fn2070-16/07 from Schaffner [Yaskawa Electric America, Inc. \(2004\)](#).

**Magnetic Contactor** The core component of the motor starter of the SMG robot is the magnetic contactor (MC), a three-pole, 2 kW (at 220 Vac single phase contact voltage), 240 Vac (coil voltage), from Moeller Electric Corporation (p/n: DIL00M(240Vac60Hz)). The latter meets the following requirements:

- The rated voltage of the circuit breaker (220 V) is in the tolerance range of the MC coil voltage rating (192 – 264 V, i.e. 80% – 110% of the rated coil voltage 240 V) [Moeller Electric Corp. \(2003a\)](#); hence, the coil of the MC can be energized by the same single-phase 220 V which supplies power to the servo, in the respect servo specifications (see page C-2 of [Yaskawa Electric America, Inc. \(2005\)](#)).
- The rated current of the MC (20 A) is greater or equal than the rated currents of the servo (11 A) and of the circuit breaker (20 A) [Moeller Electric Corp. \(2003a\)](#),
- For the given servo voltage (220 V, single phase), the rated power of the MC (2 kW) is bigger than the rated power of the servo (800 W) [Moeller Electric Corp. \(2003a\)](#).
- the current rating of the MC (20 A) meets the recommendations by Yaskawa [Yaskawa Electric America, Inc. \(2004\)](#).

Knowing that the pick-up (sealing) power consumption of the MC at the nominal coil voltage is 67 VA (8.5 VA), one can easily compute the in-rush current (nominal) flowing through the coil:  $67/240 = 0.28$  A ( $8.5/240 = 0.036$  A) [Moeller Electric Corp. \(2003a\)](#). These current values will be used in the fuse selection for push-button protection. For stock availability reasons the DIL00M(240Vac60Hz) was preferred to the DIL00M(220Vac60Hz) and to a two-pole magnetic contactor. The holding circuit contact in the three wire control scheme of Fig. 64 is the NO auxiliary contact of a 11DILM from Moeller Electric Corporation, which is rated for 10 A and 600 V. Protection from inductive kick is provided by the RC snubber circuit, implemented by a RCB DIL250 from Moeller Electric Corporation, which snaps (as the 11DILM does) on the MC.

**Overload Relay** The SMG motor starter overload relay is a Z00-16 from Moeller Electric Corporation, whose tripping current can be set in the following range: 10 – 16 A. It provides protection for the motor by sensing the current flowing to the latter and tripping in case a pre-set current value is exceeded for a specific amount of time. The motor at hand is a SGMAH-08AAF4C from Yaskawa, which has a service factor <sup>14</sup> of 1.15, according to NEMA standards, hence the trip current of the overload relay has to be set at 125% of the full-load current of the motor (11 A), i.e. 13.75 A [Moeller Electric Corp. \(2003b\)](#).

**Pushbuttons and Pilot Light** The Start and Emergency push-buttons were selected along with their momentary contacts in such a way to comply with the electrical requirements stemming from the specifications of the above-mentioned components, namely auxiliary contact, MC, and overload relay. In Table 16 full description of SMG motor starter pushbuttons and pilot lights is reported [Moeller Electric Corp. \(2003c\)](#). The pushbuttons are both rated for 10 A and 600 V.

---

<sup>14</sup>The motor service factor is the factor which multiplied by the nominal power of the motor, returns the power at which the motor can be overloaded maintaining frequency and voltage stated on the motor plate.

Component	Description	P/N
Start Pushbutton	Green Push-Button with screw terminal NO momentary contact	M22-D-G-GB1/1
Emergency-Stop Pushbutton	Tamper-proof ISO 13 850/EN 418 with screw terminal NC pull to release contact	M22-PV/K01
Pilot Light	Indicating light, extended lens, with LED element (85 – 264 V)	M22-LH-R/230-1

Table 16: Pushbuttons and pilot light

Component	Fuse Description	P/N	Fuseholder Description	P/N
Power Circuit	13/32" Time-Delay Fuse 12 Amps	7706K31 (McMaster-Carr)	22mm (W) Screw Clamp Fuse	7641K932 (McMaster-Carr)
Control Circuit	3AG SLO-BLO <sup>TM</sup> .175A/250V	F307-ND (Digi-Key)	13mm (W) Screw Clamp Fuse	7641K36 (McMaster-Carr)
Pushbuttons	3AG SLO-BLO <sup>TM</sup> .062A/250V	F303-ND (Digi-Key)	20 A fuse block for 11/4" × 1/4"	2700742 (TheSource)

Table 17: Fuses/Fuseholders of the motor starter

**Fuses** The fuses selected for the SMG robot motor starter can be classified as follows:

- power circuit protection fuses: two fuses intended to protect the power circuit of the servo-amplifier, namely port L1 and L3 of the schematic diagram reported in Fig. 64. (This represents an safety solution intentionally redundant w.r.t. the overload relay.)
- control circuit protection fuses: these are intended to protect the control circuit of the servo-amplifier, namely port L1C and L2C of the schematic diagram reported in Fig. 64.
- push-button protection fuses: these are intended to protect personnel when operating the START and Emergency push-buttons, see Fig. 64.

Table 17 indicates the p/n of the foregoing fuses and of their fuseholders.

#### A.4.5 Implementation

An implementation of the motor starter was tested along with the motor and the amplifier. The implementation is indicated in Figs. 66-71.

#### A.4.6 Power supply circuit, Servomotor Wiring and Encoder Wiring Test

A validation test of the design of the main power distribution circuit was conducted on August 10, 2005 at the McGill Robotic Mechanical Systems Laboratory.

#### A.4.7 Equipment and Test Set-up

In order to conduct the test the following equipment is needed:

- 220 Vac 20 A split-phase outlet (label: Lp4/1 cir6/8)
- power amplifier (Yaskawa P/N: SGDH-08AE-S)
- servomotor (Yaskawa P/N: SGMAH-08AAF4C)
- custom-made motor starter, see Fig.66
- encoder cable (Yaskawa P/N: JZSP-CMP00-05(A))
- motor power cable (Yaskawa JSZP-CMM10-10(A))

Here is a set of instructions to be followed in order to set-up the test

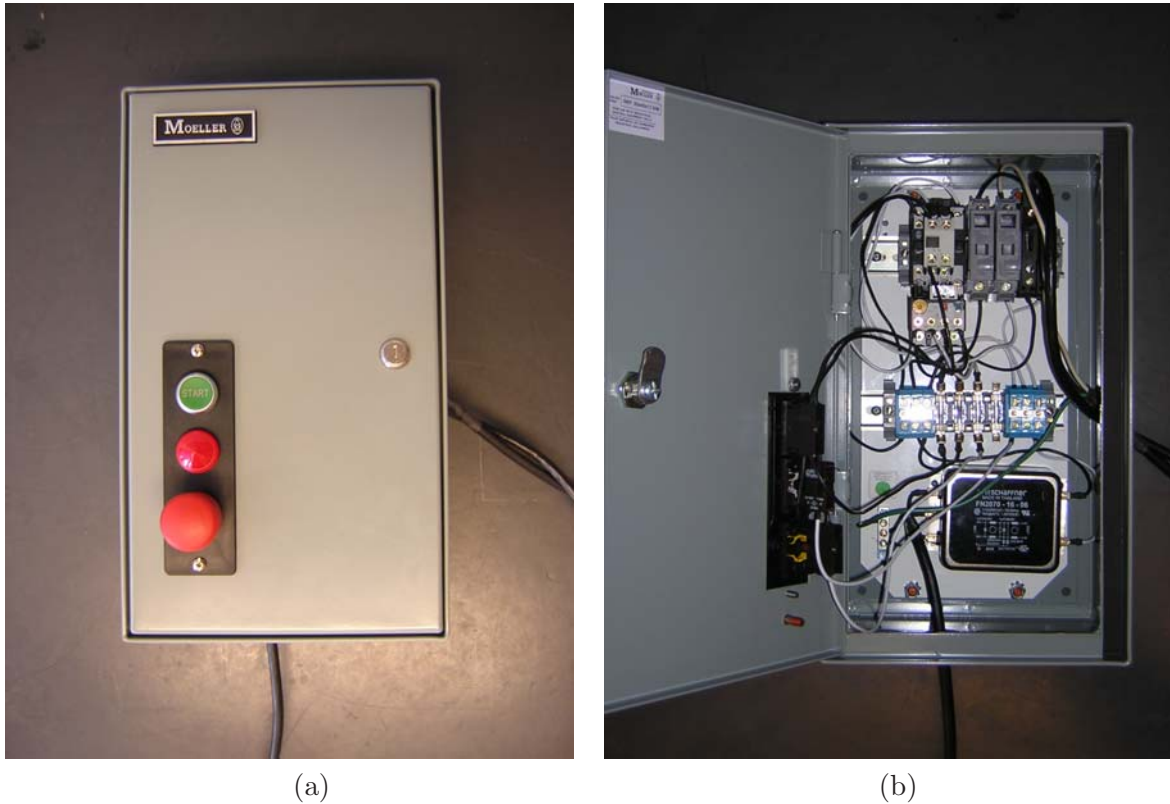


Figure 66: Custom-made motor starter: (a) closed enclosure (b) open enclosure

- Secure the motor with a C-clamp to the bench test (see Fig.70).
- Lay out the motor starter and the power amplifier as in Fig.69.
- Connect the male fire-wire connector of the encoder cable to to the CN2 terminal of the power amplifier.
- Connect the female fire-wire connector of the encoder cable to the single-ended cable coming out from the encoder case.
- Connect the motor cable to the “servomotor terminal” of the power amplifier [Yaskawa Electric America, Inc. \(2005\)](#) and connect its other end to the single-ended cable coming out from the motor case.
- Connect the three-position output plug of the motor starter unit to the “main circuit power supply terminal” (L1 and L3) of the power amplifier [Yaskawa Electric America, Inc. \(2005\)](#) and to the ground screw terminal of the servo (using the green cable with ring-terminal).
- Connect the two-position output plug of the motor starter to the “control power supply terminal” (L1C and L2C) of the power amplifier [Yaskawa Electric America, Inc. \(2005\)](#).
- Using a digital multimeter (DMM) check that there is no short.
- Close and lock the panel cover of the motor starter.

The wiring set-up is summarized in Fig. 69, which is an implementation of the schematics in Fig. 64.

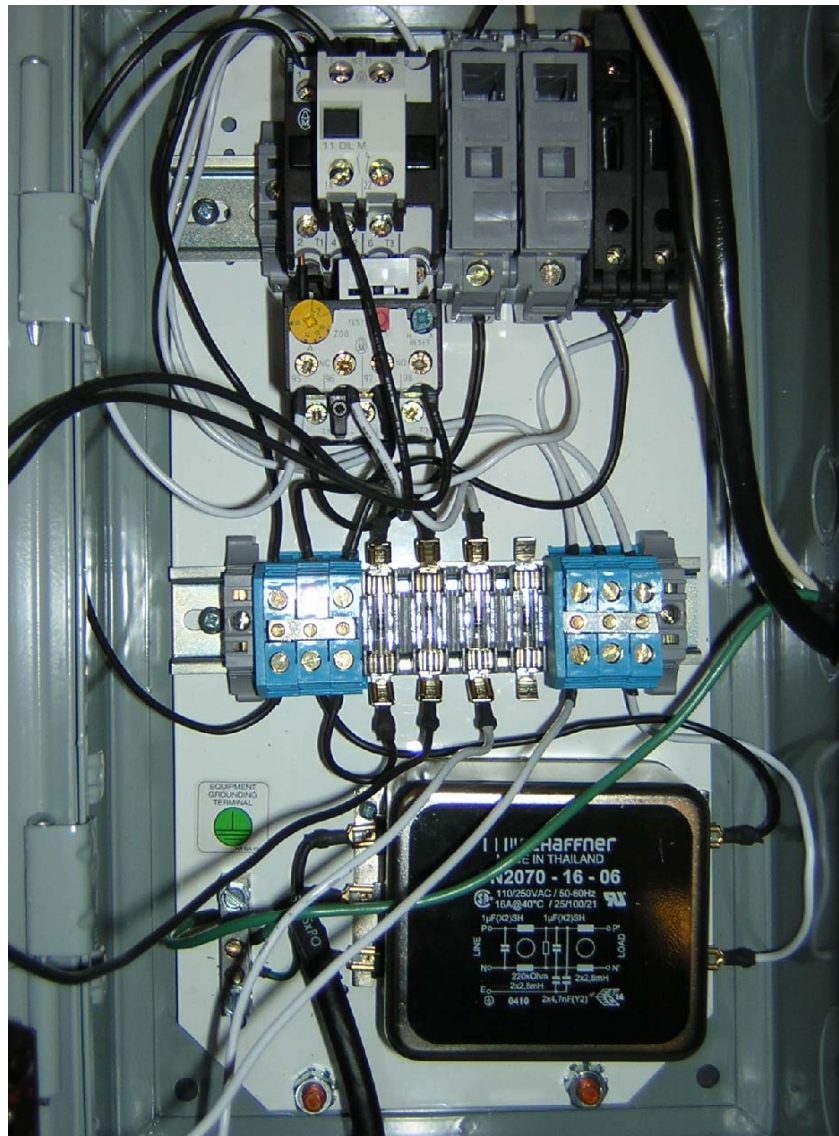
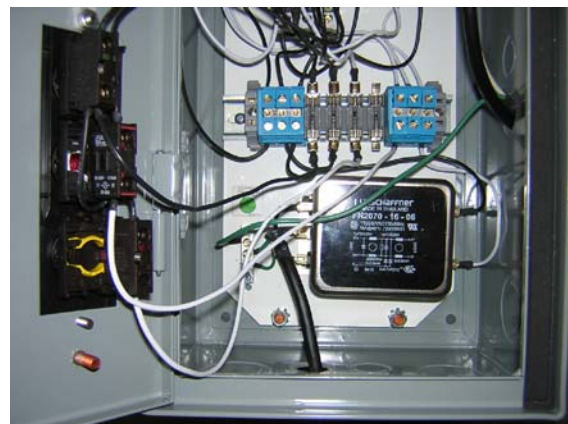


Figure 67: Motor starter wiring



(a)



(b)

Figure 68: Motor starter wiring: (a) upper part (b) lower part



Figure 69: Experimental set-up

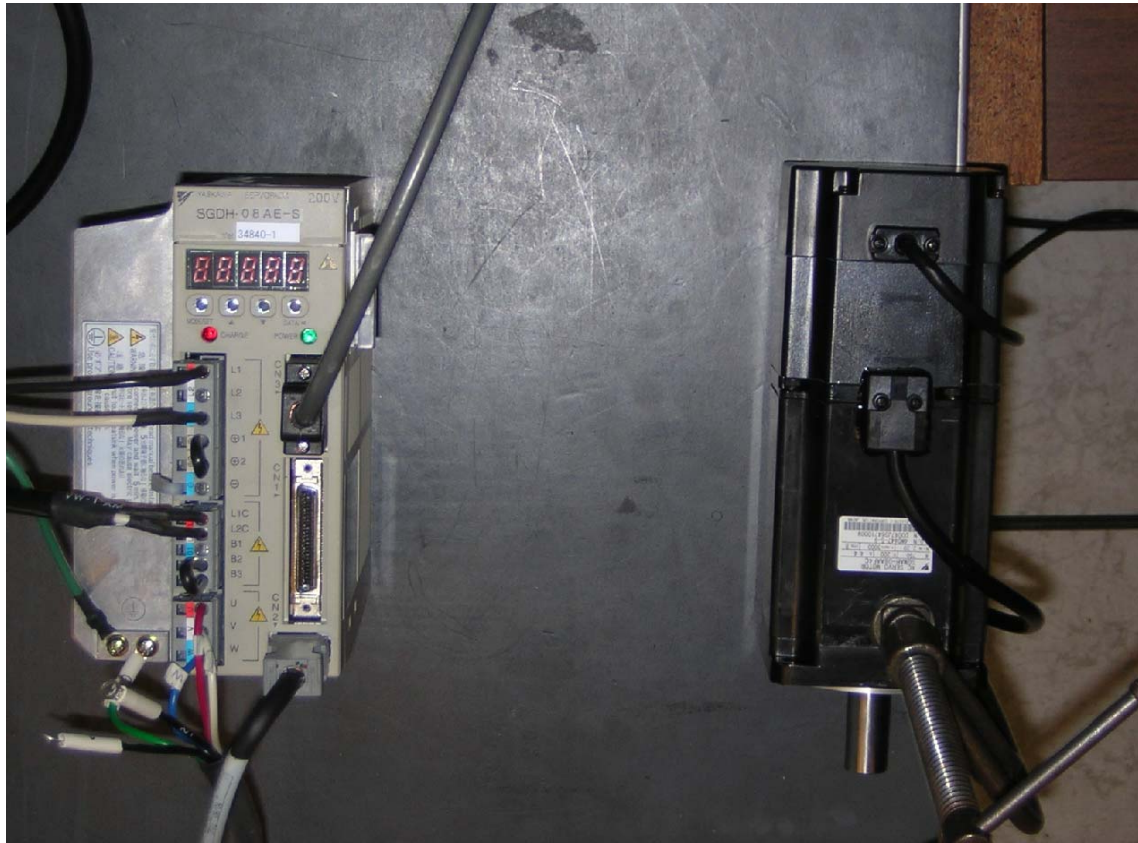


Figure 70: Wiring between amplifier and motor



Figure 71: Wiring between amplifier and starter

#### A.4.8 Warnings

A set of warnings <sup>15</sup> is in order here:

- Double-check that power supply terminal screws and motor output terminal screws are securely fastened.
- Do not touch the heat sinks of the power amplifier during operation.
- Do not touch the power amplifier while red LED is ON.
- Before starting operation, make sure that an emergency stop can be applied at any time.
- Use the servomotor alone with the motor shaft disconnected from the load.
- Close the panel cover rotating 90° clockwise the custom-made enclosure of the motor-starter before turning on the power.
- Do not touch terminals for five minutes after the power has been turned OFF.
- Do not attempt to change wiring while the power is ON.
- If the charge indicator (red LED) on the front panel of the power amplifier is ON, do not touch the servo amplifier, even after the power supply is turned OFF.
- Avoid frequently turning power ON and OFF. Do not turn power ON and OFF more than once.

#### A.4.9 Turning on the Control Power Supply of the Power Amplifier

The on-board control circuit (OBCC) of the power amplifier is supposed to be always in the ON state (L1C and L2C always powered) when wiring is completed, much like a PC in standby condition (see schematics on page C-2 of [Yaskawa Electric America, Inc. \(2005\)](#)). The first step of the test consists in powering-up the OBCC power supply, also called “control power supply” [Yaskawa Electric America, Inc. \(2005\)](#). Here are the steps to follow:

- connect the motor starter power input plug needs to be connected to one of the four 220V power outlet (in the specific case the “Lp4/1 cir6/8” was used)
- the green LED on the front-panel of the servo-amplifier should light-up (which indicates that the control power supply is ON) and contemporary the panel display <sup>16</sup> should indicate normal operation (Pot/Not) as in Fig. 72a.

As we can see from the above-mentioned Figure, the test was successful: the green LED lighted-up and the panel display output Pot/Not.

#### A.4.10 Turning ON the Main Circuit Power Supply of the Power Amplifier

In order to turn ON the “main circuit power supply” [Yaskawa Electric America, Inc. \(2005\)](#) which powers the IGBT-bridge of the power amplifier, the following step should be taken:

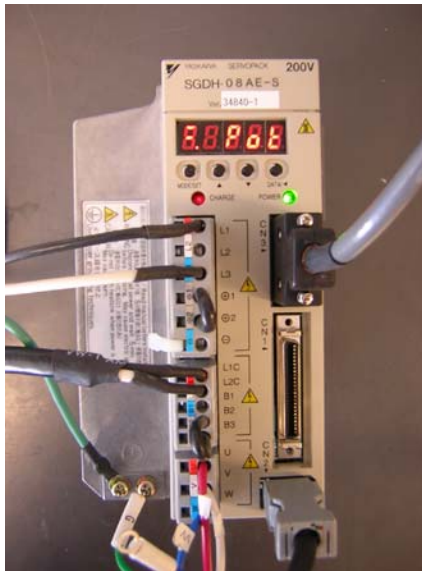
- Push for at least two seconds the green START button on the front panel of the motor starter.

---

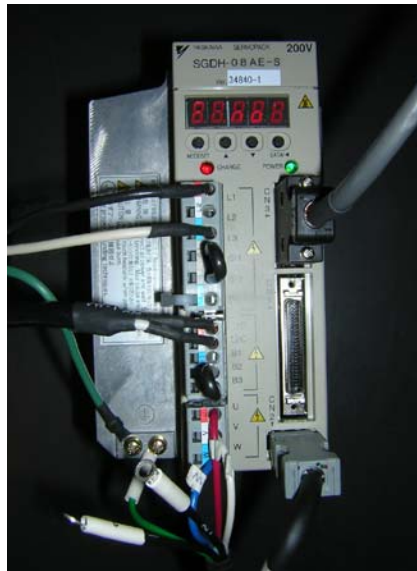
<sup>15</sup>Warning: Indicates a potentially hazardous situation, which, if not heeded, could result in death or serious injury.

<sup>16</sup>A five-digit seven-segment display panel used to show servo status, alarm status, and other values when parameters are entered.





(a)



(b)

Figure 72: LED display: (a) green LED ON (control power supply is ON); (b) red LED ON (main circuit power supply is ON)



(a)



(b)

Figure 73: Magnetic contactor status: (a) MC armature sealed-in; (b) MC armature drop-out.

- A “click” should be heard, coming from the motor starter enclosure, which indicates that the armature of the magnetic contactor has been sealed-in, Fig. ?)a.
- At the same time the red LED, a.k.a. charge indicator <sup>17</sup>, on the front panel of the power amplifier should light-up (main power circuit supply is ON), as in Fig. 72b and
- Contemporary the panel display should indicate normal operation (Pot/Not) as in Fig. 72b.

As shown in Figs. 73a and 72b , the test was successful: the armature was sealed-in, the red LED lighted-up and the panel display output was normal (Pot/Not).

#### A.4.11 Turning OFF the Main Circuit Power Supply of the Power Amplifier

In order to turn OFF the “main circuit power supply” [Yaskawa Electric America, Inc. \(2005\)](#) which powers the IGBT-bridge, the following step should be taken:

- push the red button on the front panel of the motor starter.
- a double “click” should be heard: one is coming from MC, which indicates that the armature of the magnetic contactor has been dropped out, Fig. ?)b, while the other comes from the actuation of the red button (which is of the pull to release type).
- contemporary the panel display <sup>18</sup> should indicate normal operation (Pot/Not) as in Fig. 72b.

As shown in Figs. 73b and 72a, the test was successful: the armature was dropped out and the panel display output was normal (Pot/Not).

#### A.4.12 Alarm Signal Testing

As we have seen all the testing were successful. However, it is important to be aware also of alarm signal output on the panel display of the power amplifier.

The Yaskawa SGDH-08AES is what is commonly called a ”smart” amplifier capable of self-checking. More specifically, when the control power supply is turned ON the panel display can output an alarm signal such as A.F1, see Fig. 74, which means one of the following problems:

- faulty main power distribution circuit.
- faulty encoder wiring.
- defective servo amplifier.
- faulty servomotor wiring.

In order to double-check the result, the control power supply was turned OFF (i.e. the motor starter power input plug was disconnected from the split-phase outlet) and motor and encoder were intentionally disconnected. The power was then re-applied and the LED amplifier displayed the alarm output A.F1, giving us confirmation of the fact that encoder and servomotor were not connected.

---

<sup>17</sup>Lights when the main circuit power supply is ON and stays as long as that component s capacitor remains charged

<sup>18</sup>A five-digit seven-segment display panel used to show servo status, alarm status, and other values when parameters are entered.

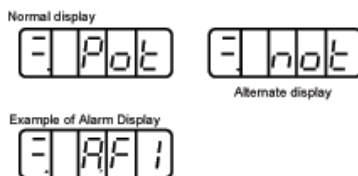


Figure 74: Panel display of the Yaskawa servo amplifier [Yaskawa Electric America, Inc. \(2005\)](#).

## A.5 High Level Control of the Motor Amplifiers

Two methods are used for interfacing with the SGDh amplifiers which are used to drive the motors of the SMG manipulator. The first, used during setup and calibration, is via the standard RS-232 serial port of a personal computer and the RS-232 serial connector on the individual amplifiers. It is possible to use either manufacturer-provided software or terminal programs such as RealTerm, MiniCom or HyperTerminal to communicate with the amplifiers using the serial communication method.

The second method for communication with the amplifiers is used during regular operation. This method uses two computers, a “master” and a “slave”. The master computer is manipulated directly by the user. It is a standard Microsoft Windows based personal computer equipped with Matlab/Simulink and the Opal RT RT-Lab toolbox. The Simulink graphical user interface is used to manipulate RT-Lab control sequences that are compiled and transferred via ethernet to a second slave computer which houses much of the necessary interface hardware for the SGDh amplifiers. This second PC executes RL-Lab commands in hard real time through the use of the QNX real time operating system. The user is required to connect the amplifiers to the various ribbon cable connectors which are found at the rear of the slave PC. These cables are connected to two internal Sensoray 626 input/output cards. The connection configuration is described in Tables 18, 19, and 20. The user requires no direct interaction with the slave PC beyond setting up external connections between the Sensoray boards and the SGDh amplifiers (including intermediate isolation boards).

Although there are a number of methods for establishing a user interface to the motor amplifiers the above setup was chosen for a number of reasons. The most important reason was the fact that both the Sensoray hardware and RT-Lab software was already in use for another project in the Robotic Mechanical Systems Lab. A knowledge base has already been developed within the RMSL with respect to the particular nature of the Sensoray hardware and RT-Lab software. In addition, the Matlab/Simulink interface is widely used amongst engineering students, making it relatively easy for new users to become familiar with control of the SMG hardware.

## A.6 The Yaskawa SGDh-08AE-S Servo Amplifiers

There are six connectors on the front of the servo amplifier. Three of these connectors are for high-power wires, while the other three are for low-power signals. The high power connectors are distinguishable by the “shock” symbol.

### A.6.1 Signal Connectors

The three signal connectors are named “CN1”, “CN2”, and “CN3”. See pages 3-18, 3-19, 3-20 and 3-26 of the Sigma II User Manual for details about the various signals. Below are the method in which we propose using these cables for the SMG Project.

#### **CN1: I/O Signal Connector**

CN1 is the main signal connector, with 50 individual pins. Use the Honda MR-50L cable and the JUSP-TA50P breakout box to interface it to other electronics such as the Sensoray Model 626 PCI Multifunction I/O Board.

Seven of the outputs from the Sensoray 626 I/O board need to be optically isolated in order to interface them to a number of discrete control signal lines on the Yaskawa SGDh amplifier. These control signal lines (CN1-40 through CN1-46) on the SGDh require 24 VDC to function properly, while the Sensoray board only provides 5 VDC outputs. The conversion circuit is illustrated in Fig. 75. A prototype for one amplifier has been completed and requires testing. More details about the requirements for these inputs can be found in Section 5.2.4 of the Sigma II User’s Manual.

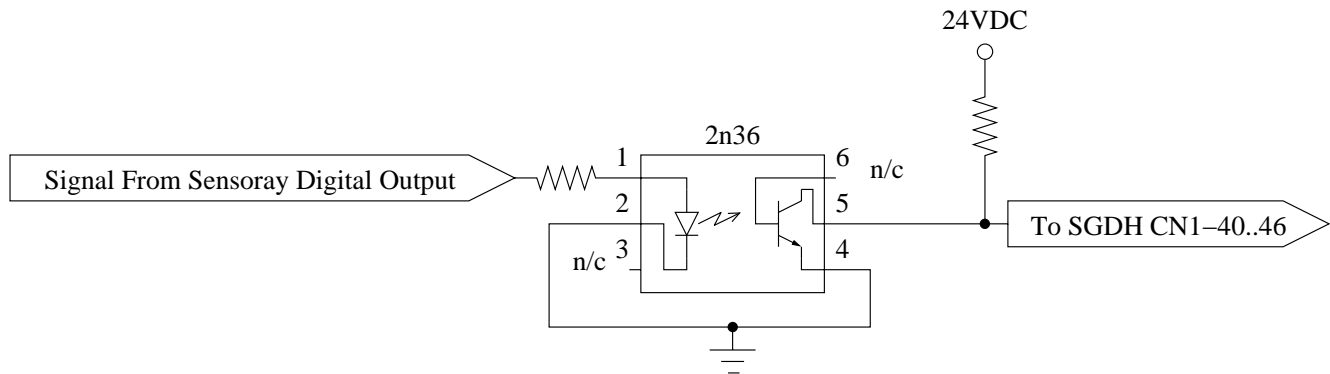


Figure 75: Schematic for the optically isolated conversion circuit which drives a number of digital inputs on the SGDh amplifier.

A number of discrete 30 VDC outputs are also available on the SGDh amplifiers. They are meant to either drive relays or opto-isolators. In the example of the the *ALM* signal, it is used to drive a relay which can shut down power to the amplifier in the event of an emergency, as shown in Fig. 76. A detailed example of the power switch configuration, including alarm shut-down functionality, can be found in Fig. 65. In the case of 50 mA output lines (i.e. *ALM*, *V-CMP*, *TGON* and *S-RDY*) the resistors R1 and R2 (see Fig. 76) have values 470 Ohm and 4.7 kOhm, respectively. In the case of the 20 mA outputs (e.g. *AL01*, *AL02* and *AL03*) R1 is 1.3 kOhm, while R2 is 4.7 kOhm. In addition, the *AL01*, *AL02* and *AL03* outputs are internally grounded and thus don’t require an external ground connection. More details about the requirements for these outputs can be found in Section 5.2.4 of the Sigma II User’s Manual.

### CN2: Encoder Connector

CN2 is used to connect the motor’s quadrature position encoders to the amplifier. No modifications need to be made with respect to this connector; simply use the Yaskawa-supplied cables to connect the motor encoder for one motor to the amplifier. These cables have Firewire-type (IEEE-1394) connectors, making them relatively easy to identify.

### CN3: Connector to PC or Digital Operator

As with CN2, you simply need to use a Yaskawa supplied cable to connect to this port. The other end of the cable should be plugged into a personal computer’s DB-9 RS-232 serial port. Yaskawa also provides custom software to allow the user to send configuration information from the PC to the amplifier via this serial port cable.

## A.7 Computer Interface Card: Sensoray Model 626

The Sensoray Model 626 board was chosen to interface the four servo amplifiers to a computer since it provides appropriate input/output (general purpose digital I/O, quadrature decoder and analogue I/O), is currently in use with another project and uses a Matlab-compatible interface which is familiar to many university students. Two of these boards are housed within a “slave” computer which is controlled via a “master” computer running Matlab/Simulink and the RT-Lab toolbox interface software.

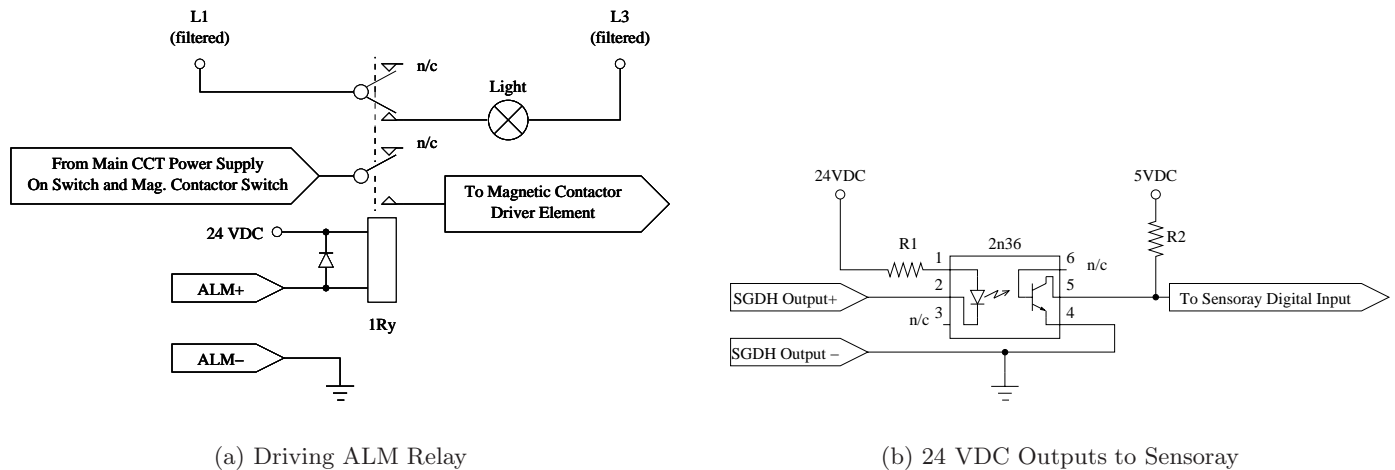
### Quadrature Decoders on Sensoray 626

Table 18: SGDH Amplifier CN1 Connections (1-25)

SGDH Pin No.	SGDH Function	Function	Interface to Sensoray	Sensoray Connector	Sigma II Reference	Note
CN1-1	SG	Ground	Yes, Direct	J2-2,4,6,8	5-72	-
CN1-2	SG	Ground	Yes, Direct	J3-2,4,6,8	5-72	-
CN1-3	PL1	Open-Col PWR	No	n/c	5.2.1	Position Ref.
CN1-4	SEN	SEN Input	No	n/c	5.2.3	Abs. Enc.
CN1-5	V-REF	Ref. Speed Input	Yes, Direct	J1-42,44,46,48	5.2.1	-10 to +10 VDC
CN1-6	SG	Ground	Yes, Direct	J1-40	5-72	-
CN1-7	PULS	Ref. Pulse In.	No	n/c	5.2.1	Position Ref.
CN1-8	PULS'	Ref. Pulse In.	No	n/c	5.2.1	Position Ref.
CN1-9	T-REF	Ref. Torque In.	No	n/c	5.2.1	Torque Ref.
CN1-10	SG	Ground	Yes, Direct	(J2-2,4,6,8) <sup>19</sup>	5-72	-
CN1-11	SIGN	Ref. Sign In.	No	n/c	5.2.1	Position Ref.
CN1-12	SIGN'	Re. Sign In.	No	n/c	5.2.1	Position Ref.
CN1-13	PL2	Open-Col PWR	No	n/c	5.2.1	Position Ref.
CN1-14	CLR'	Clear Input	No	n/c	5.2.1	Position Ref.
CN1-15	CLR	Clear Input	No	n/c	5.2.1	Position Ref.
CN1-16	-	-	No	n/c	-	(nothing)
CN1-17	-	-	No	n/c	-	(nothing)
CN1-18	PL3	Open-Col PWR	No	n/c	5.2.1	Position Ref.
CN1-19	PC0	C-Phase Encoder	No	n/c	5.2.3	Third Encoder
CN1-20	PC0'	C-Phase Encoder	No	n/c	5.2.3	Third Encoder
CN1-21	BAT (+)	Battery	No	n/c	5.2.3	Abs. Encoder
CN1-22	BAT (-)	Battery	No	n/c	5.2.3	Abs. Encoder
CN1-23	-	-	n/c	n/c	-	(nothing)
CN1-24	-	-	n/c	n/c	-	(nothing)
CN1-25	V-CMP+'	Speed Coinc. Out	Yes, Opto	J2-1,3,5,7	5.5.4	Fig. 76b., 50 mA.

Table 19: SGD H Amplifier CN1 Connections (26-50)

SGDH Pin No.	SGDH Function	Function	Interface to Sensoray	Sensoray Connector	Sigma II Reference	Note
CN1-26	V-CMP-'	Speed Coinc. Out	Yes, Ground	J2-2,4,6,8	5.5.4	To Power Ground
CN1-27	T-GON+'	TGON Out	Yes, Opto	J2-9,11,13,15	5.5.5	Fig. 76b., 50 mA.
CN1-28	T-GON-'	TGON Out	Yes, Ground	J2-10,12,14,16	5.5.5	To Pwr Ground
CN1-29	S-RDY+'	Servo Ready Out	Yes, Opto	J2-17,19,21,23	5.5.6	Fig. 76b., 50 mA.
CN1-30	S-RDY-'	Servo Ready Out	Yes, Ground	J2-18,20,22,24	5.5.6	To Pwr Ground
CN1-31	ALM+	Servo Alarm Out	Yes, Relay	n/c	5.5.1	To Pwr Relay
CN1-32	ALM-	Servo Alarm Out	Yes, Ground	n/c	5.5.1	To Pwr Ground
CN1-33	PA0	Encoder A	Yes, Direct	J4 or J5	5.2.3	Table 20
CN1-34	PA0'	Encoder A	Yes, Direct	J4 or J5	5.2.3	Table 20
CN1-35	PB0	Encoder B	Yes, Direct	J4 or J5	5.2.3	Table 20
CN1-36	PB0'	Encoder B	Yes, Direct	J4 or J5	5.2.3	Table 20
CN1-37	AL1	Alarm 1	Yes, Opto	J2-25,27,29,31	5.5.1	Fig. 76b., 20 mA
CN1-38	AL2	Alarm 2	Yes, Opto	J2-33,35,37,39	5.5.1	Fig. 76b., 20 mA
CN1-39	AL3	Alarm 3	Yes, Opto	J2-41,43,45	5.5.1	Fig. 76b., 20 mA
CN1-40	S-ON'	Servo ON in	Yes, Opto	J3-1,3,5,7	5.5.2	Fig. 75
CN1-41	P-CON	P operation in	Yes, Opto	J3-9,11,13,15	5.2.1-7	Fig. 75
CN1-42	P-OT	Forward Overtravel in	Yes, Opto	J3-17,19,21,23	5.1.2	Fig. 75
CN1-43	N-OT	Reverse Overtravel in	Yes, Opto	J3-25,27,29,31	5.1.2	Fig. 75
CN1-44	ALM-RST'	Alarm Reset in	Yes, Opto	J3-33,35,37,39	5.5.1	Fig. 75
CN1-45	P-CL'	Fwd current limit On in	Yes, Opto	J3-41,43,45,47	5.1.3, 5.2.6	Fig. 75
CN1-46	N-CL'	Rev current limit On in	Yes, Opto	(J2-1,3,5,7) <sup>20</sup>	5.1.3, 5.2.6	Fig. 75
CN1-47	24V-IN	External Input Power	No	n/c	5.2.4	To Wall Wart
CN1-48	PSO	S-phase signal out	No	n/c	5.2.3	Abs. Encoder
CN1-49	PSO'	S-phase signal out	No	n/c	5.2.3	Abs. Encoder
CN1-50	-	-	No	n/c	-	(nothing)



(a) Driving ALM Relay

(b) 24 VDC Outputs to Sensoray

Figure 76: On the left is an example of using the SGDH to drive a relay responsible for emergency shutdown of the amplifier. On the right is a schematic for interfacing one of these 24 VDC outputs to the Sensoray I/O board.

According to Appendix C: Encoder Connectors of the Sensoray 626 Instruction Manual, two 26 pin IDC ribbon cable connectors are available for interfacing with the quadrature encoders on the SMG robot. The quadrature encoder outputs from the servo amplifiers are set up in RS-422-compatible differential pairs (see Section 3.4.3 of the Sigma II User’s Manual) which are compatible with the quadrature decoders of the Sensoray board (see Section 10. Counters of the Sensoray manual). The index signals are not required, nor are connections to the ground and 5 volt pins on connectors J4 and J5 of the Sensory board since power is supplied internally within the SGDH amplifier and the signal ground reference is available from other pins on the CN1 connector. This requires a total of four signal wires per motor axis, consisting of two separate phases, each with their own differential pair.

### A.7.1 Home Position Calibration

Four Hall Effect Sensors and associated magnets are to be installed on the robot mechanism. These sensors are to be used to “home” the robot prior to normal operation.

Orientation of the Hall Effect Sensor and its magnet is critical. It is also recommended that the surface of the magnet and the Hall Effect Sensor be permitted to pass within three millimeters of one another. If a greater distance is required then it is recommended that two or more magnets be stacked one on top of another in order to strengthen the magnetic field detectable by the Hall Effect Sensor. A battery-powered, hand-held Hall Effect Sensor has been developed within the Mechatronic Locomotion Lab to aid in alignment and installation tasks.

An algorithm for calibration of the Home position of each of the four motor axes will need to be developed. It is recommended that each motor axis be calibrated individually. Since the Hall Effect Sensor is a binary sensor with a relatively high threshold (it’s not very sensitive) of detection it is important that the calibration algorithm be setup in such a way as to allow the magnet and Hall Effect Sensor to approach one another from both the clockwise and counter-clockwise directions. This, when combined with information from the motor position encoders, will allow the edges of the Hall Effect’s band of detection to be determined (each sensor will have a unique value for the width of this band due to variation in magnet material properties and installation variation).

Two types of magnets are available for installation in the SMG robot: the grey rectangular H-

Table 20: Quadrature Connections.

Sensoray Connector	Sensoray Pin Num.	Sensoray Function	Servo Number	Servo Pin Num.	Servo Function
J5	1	Encoder (0A) A-	1	CN1-33	PA0
J5	2	Encoder (0A) A+	1	CN1-34	PA0'
J5	3	GND	n/a	n/a	n/a
J5	4	Encoder (0A) B-	1	CN1-35	PB0
J5	5	Encoder (0A) B+	1	CN1-36	PB0'
J5	6	5VDC	n/a	n/a	n/a
J5	7	Encoder (0A) I-	n/a	n/a	n/a
J5	8	Encoder (0A) I+	n/a	n/a	n/a
J5	9	GND	n/a	n/a	n/a
J5	10	Encoder (1A) A-	2	CN1-33	PA0
J5	11	Encoder (1A) A+	2	CN1-34	PA0'
J5	12	5VDC	n/a	n/a	n/a
J5	13	Encoder (1A) B-	2	CN1-35	PB0
J5	14	Encoder (1A) B+	2	CN1-36	PB0'
J5	15	GND	n/a	n/a	n/a
J5	16	Encoder (1A) I-	n/a	n/a	n/a
J5	17	Encoder (1A) I+	n/a	n/a	n/a
J5	18	5VDC	n/a	n/a	n/a
J5	19	Encoder (2A) A-	3	CN1-33	PA0
J5	20	Encoder (2A) A+	3	CN1-34	PA0'
J5	21	GND	n/a	n/a	n/a
J5	22	Encoder (2A) B-	3	CN1-35	PB0
J5	23	Encoder (2A) B+	3	CN1-36	PB0'
J5	24	5VDC	n/a	n/a	n/a
J5	25	Encoder (2A) I-	n/a	n/a	n/a
J5	26	Encoder (2A) I+	n/a	n/a	n/a
J4	1	Encoder (0B) A-	4	CN1-33	PA0
J4	2	Encoder (0B) A+	4	CN1-34	PA0'
J4	3	GND	n/a	n/a	n/a
J4	4	Encoder (0B) B-	4	CN1-35	PB0
J4	5	Encoder (0B) B+	4	CN1-36	PB0'
J4	6	5VDC	n/a	n/a	n/a
J4	7	Encoder (0B) I-	n/a	n/a	n/a
J4	8	Encoder (0B) I+	n/a	n/a	n/a



33 magnet<sup>21</sup>, while the gold-coloured D063A-AU disk magnets are available from Amazing Magnets, <http://www.amazingmagnets.com/products.asp?ID=1000-10-1100>.

The Hall Effect Sensor is a Micronas HAL506UAE, <http://www.micronas.com/products/documentation/senso>. The branded side of the sensor is the sensitive surface and will respond to magnetic south poles. When a magnetic field with the correct orientation and strength is detected, the output pin (3) of the sensor is grounded; otherwise it is electrically neutral unless connected to a pull-up resistor.

**Prior to final installation** it is recommended that the orientation of the magnet be tested with a hand-held Hall-Effect test circuit, as illustrated in Figure 77.

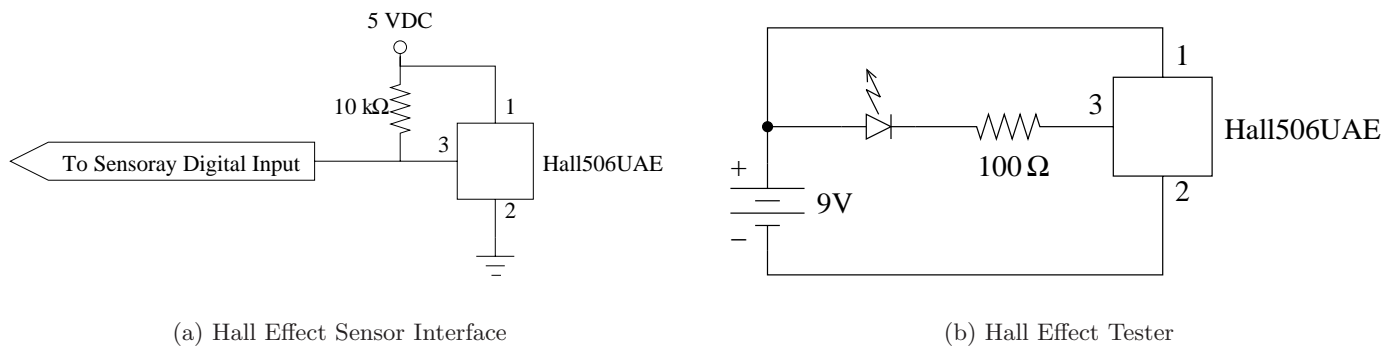


Figure 77: Schematics for a Hall Effect Sensor & Magnet Tester. Note that the branded side of the sensor is sensitive; Pin 1 is on the left when facing the branded side.

## A.8 Appendix

### A.8.1 Bill of Materials

Prices are all in Canadian dollars and before sales taxes and shipping charges.

Description	P/N	qty	total cost(\$)
Servomotor	SGMAH-08AAF4C	4	4988.00
Servo-amplifier	SGDH-08AE-S	4	4768.00
Motor power cable	JZSP-CMM10-10	4	220.00
Encoder cable	JSZP-CMP00-05(A)	4	280.00
I/O Cable with terminal block	DAPSXS50/JUSP-TA50P	4	1144.00
PC serial port cable	YS-12	1	40.00
SigmaWin with set-up and monitoring s/w	JZSP-WP001	1	40.00

Table 21: Servomotor and Servo-amplifier (Yaskawa Electric America Inc.)

Description	P/N	qty	total cost(\$)
Bayside planetary reducer, ratio 20:1	PS-90-020-SD	4	6,971.04
Bayside mounting kit for Yaskawa SGMAH08	MT90-020-081	4	0.00

Table 22: Planetary Gearhead (Bayside Controls Inc.)

<sup>21</sup>H-33 Magnet is available from Digikey (# HE512-ND); dimensions are found in <http://rocky.digikey.com/WebLib/Hamlin/WEB%20INFO/H-33%20Magnet.pdf>

Description	P/N	qty	total cost(\$)
Magnetic contactor	DIL00M(230V50HZ,240V60HZ)	4	380.80
Overload relay	Z00-16	4	238.00
Auxiliary contact	11DILM	4	54.40
RC surge suppressor	RCBDIL250	4	108.80
Pilot red light	M22-LH-R/230R	1	34.76
Start green push-button	M22-D-G-GB1/K10	1	18.56
Emergency stop push-button (pull to release)	M22-PV/K01	1	48.45
Control relay	DILER-22-G(24VDC)	2	137.72
Steel Enclosure for push-buttons	GKP23X40X17.5/M	1	220.85

Table 23: Motor Starter — part 1 (Moeller Electric Corp.)

### A.8.2 Bending Moment of the Extra-Support Bearing Structure — Matlab Code

```

f20=[7.1*20*.94*tan(pi*20/180)]/(0.057/2)    %radial force in section B of Fig.2
F=f20
d2=0.065;d1=0.032;d3=0.010;d8=0.075;        %see Fig.1 of BDC.pdf
l=(d1/2)+d8
a=d2+(d1/2)+d3/2                               %see Fig.2 of BDC.pdf
b=l-a;                                           %see Fig.2 of BDC.pdf
X=F*((a^3)-(3*a*l^2)+(2*l^3))/(2*b^3)         %reaction force, see Fig.2
Ra=X-F                                           %reaction force in section
sigma_star=X*a/Ra
l-sigma_star    %section in which the bending moment is zero
sigma29=l-0.0185
M=Ra*sigma29-X*a    %bending moment in section S
a=0:0.001:sigma29; %a has to be smaller than sigma
M=(F*((a.^3)-(3*a.*l^2)+(2*l^3))/(2*(1-a).^3)-F)*sigma29-...
(F*((a.^3)-(3*a.*l^2)+(2*l^3))/(2*(1-a).^3))*a;
plot(a,M)    %M_a_10093.fig
grid xlabel('a [m]') ylabel('M [Nm]') title('Bending Moment at 29mm
from flange with l=0.093m') a=d2+(d1/2)+d3/2;
Ma=Ra*l-X*a    %bending moment in section A
a=0:0.001:l; Ma=(F*((a.^3)-(3*a.*l^2)+(2*l^3))/(2*(1-a).^3)-F)*l-...
(F*((a.^3)-(3*a.*l^2)+(2*l^3))/(2*(1-a).^3))*a; figure
plot(a,Ma)    %M_a_10093.fig
grid xlabel('a [m]') ylabel('Ma [Nm]') title('Bending Moment at the
root with l=0.093m')
a=d2+(d1/2)+d3/2    %see Fig.2 of BDC.pdf
sigma=a:0.001:l;
Msigma=(F*((a.^3)-(3*a.*l^2)+(2*l^3))/(2*(1-a).^3)-F).*sigma-(F*((a.^3)-...
(3*a.*l^2)+(2*l^3))/(2*(1-a).^3))*a; %bending moment$
figure
plot(sigma,Msigma)    %Msigma_10093.fig
grid xlabel('sigma [m]') ylabel('Msigma [Nm]') title('Bending Moment
between cross-section C and A with l=0.093m')

```

	P/N	Manufacturer/Distributor	qty	total
single-conductor wire 14AWG, black	7587K971	McMaster-Carr	1	14.7
single-conductor wire 14AWG, white	7587K974	McMaster-Carr	1	14.7
single-conductor wire 14AWG, green	7587K995	McMaster-Carr	1	14.7
bar, DIN 3, 35mm	861K15	McMaster-Carr	2	8.66
time-delay, fuse 12Amps 250V	7706K31	McMaster-Carr	10	26.3
rail-mount terminal block DIN 3, screw clamp, 10mm width	7641K26	McMaster-Carr	50	83.0
rail-mount terminal block DIN 3, screw clamp fuse, 13mm width	7641K36	McMaster-Carr	8	72.0
rail-mount terminal block DIN 3, screw clamp fuse, 22mm width	7641K932	McMaster-Carr	8	99.9
DIN 3, 13mm, screw clamp fuse	7641K49	McMaster-Carr	20	14.6
for 5-10mm screw clamp DIN rail-mount terminal block	7641K32	McMaster-Carr	30	12.6
for DIN 3 screw clamp modular DIN rail-mount terminal block	7641K35	McMaster-Carr	20	16.8
rail-mount terminal block, DIN 3, screw clamp ground, 10mm width	7641K83	McMaster-Carr	25	123.0
for 10mmBlock width, DIN 3 modular DIN rail-mount terminal block	7641K17	McMaster-Carr	4	30.5
	FN2070-16-06	Schaffner/Newark	4	436.0
24V 3AG SLO-BLO	F303-ND	Digi-Key	10	22.0
24V 3AG SLO-BLO	F307-ND	Digi-Key	10	22.0
24V 3AG SLO-BLO	F307-ND	Digi-Key	10	22.0
for 14-18AWG	A29871CT-ND	Digi-Key	100	7.74
for 14-18AWG	A27610CT-ND	Digi-Key	100	5.16
(14AWG each) shielded cable	n/a	Canadian Tire	1	n/a
(14AWG each) shielded cable	n/a	Canadian Tire	1	n/a
block	2700742	The Source CC	1	3.99

Table 24: Motor Starter — part 2

Description	P/N	Manufacturer/Distributor	qty	total cost(\$)
PC board 3-hole	V1044-ND	Digi-Key	1	100.36
Optocoupler	4N36-ND	Digi-Key	28	17.15
Resistor 270Ohm	PPC270W-1CT-ND	Digi-Key	25	11.45
24V transformer 2.5Amps	T827-P5P-ND	Digi-Key	1	48.25
22AWG hook-up cable solid core (green, red, black)	n/a	The Source CC	1	n/a
25ft 22AWG hook-up cable (white)	n/a	Future Active	1	n/a

Table 25: Sequence Input Circuit Interface Board

## B Carbon Fibre Limbs: Prototype Fabrication Methodology

The prototype carbon fibre actuator arm was developed by the McGill Composites Group for the McGill Centre for Intelligent Machines and Technospin Inc. The actuator arm is to be used in the novel parallel Schnflies-Motion Generator. This document describes the procedure followed during the fabrication of the first set of four arms. Photographs and short descriptions are used to give a step-by-step narrative useful towards future part production.

### B.1 Basic Procedures

#### B.1.1 Cutting out Pre-Preg Material

This section explains how to cut the pre-preg material in order to prepare the various layers for the part lay-up. LTM 25 Woven Pre-Preg from distributor Advanced Composites Group was used in this project. The material may be left out of the freezer for up to 5 or 6 days before it begins curing.



The pre-preg material should be stored in the freezer.



The first step is to trace the shape of each piece needed for the lay-up on the pre-preg material. These pieces are outlined in the section entitled "Schedule of Lay-up Pieces"



The individual pieces must be cut out of the long sheet of fibre according the shapes traced.

#### B.1.2 Mold Preparation

Before any material can be set in place, the aluminum mold and all parts that come in contact with the carbon fibre materials must be cleaned and coated with release agent.

#### B.1.3 Bag Preparation

In order to provide internal pressure during the molding of the carbon fibre actuator arm, it was decided to use a system where compressed air is forced into bags within the part. A set of Airtech KM1300 nylon vacuum bags were used in this project.

#### B.1.4 Foam Rib Preparation

In order for the two air bags being used to have some surface area to press against in the middle of the part, a foam rib was created. This rib is used to provide support in the middle of the part and to cover the small parts where the air bags cannot reach.



The surface of the aluminum mold must be cleaned with Acetone in order to remove any dirt or resin residue. This must only be done before the first use, after which simply scraping away the resin with a wedge of plaxiglass will do.



In order to ensure the finished part can be easily removed from the mold, 5 coats of Chemlease 41-90 release must be applied before the first molding. Beyond that only 2 coats must be applied if no Acetone is used to clean the mold. At least 10 minutes must be left in between coats.



It is also necessary to clean and apply release to the aluminum 'end plugs'. There are 2 one-piece end plugs for the wide end of the part, and 2 two-piece end plugs for the thin end.



Chemlease Mold Sealer and ReleaseChemlease MPP-177Wipe on and wipe dry for high gloss. Two coats are needed, with 30 minutes in between coats. Must only be applied first time mold is used.Chemlease 41-90Wipe on and wipe dry for high gloss. Five coats are needed, with 10 minutes in between coats. Must be applied before every molding.



Two 5" wide bags of about 32" in length are needed during the making of one part.



Each bag must be turned inside out in order to seal the end of the bag.



Three seals are made about  $\frac{1}{4}$ " apart from each other at one end of the bag using an impulse sealer.



The bag is then undone to regain its original form.



The sealed end of the bag is folded up and placed within the hollow end plug.



The air input part is placed into the open end of the bag. The bag is then rolled around the part as tightly as possible. Sealing tape can be used to ensure there are no air leaks.



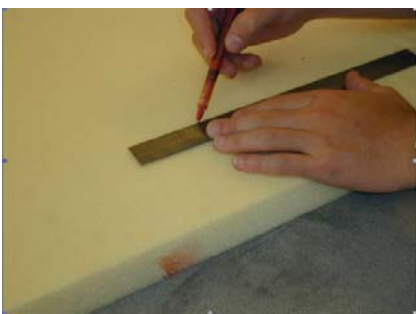
The wrapped air input is then placed into the two-piece end plug. It is important that no part of the bag get pinched on the sides.



The two sides of the end plug are squeezed together with the air input and bag inside it.



Sealing tape should be used to ensure the end plug is closed tightly. The tape should not cover any surface where the material will wrap around.



The shape of the foam rib needed is first drawn out on a large sheet of foam. The foam must be 1" in height.



The rib is cut out on the band saw.



Any sections that need to be bonded are done using 5 minute epoxy glue.



In order to obtain the proper curvature for the foam to fit in the part, the ends must be rounded to give  $\frac{1}{2}$ " radius.

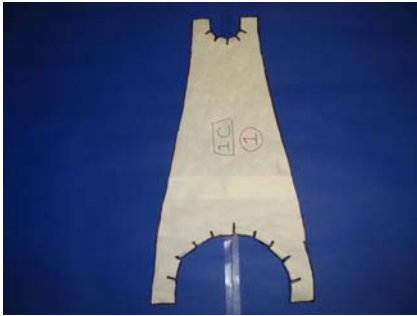


The completed part should fit snugly into the mold.

## B.2 Part Lay-up

### B.2.1 Schedule of Lay-up pieces

In order to obtain the desired number of layers of carbon fibre material in specific areas of the part, several different lay-up pieces must be used. The design of the carbon fibre actuator arm required 5 layers of woven pre-preg material at each of the ends, and 3 layers for the rest of the part. In order to better describe the lay-up procedure, photographs of each piece are shown below.



Piece 1 - (Qty: 2) The first layer placed on both the top and bottom mold.



Piece 1-A - (Qty: 2) Patch for openings created by cuts in Piece 1 on thin end.



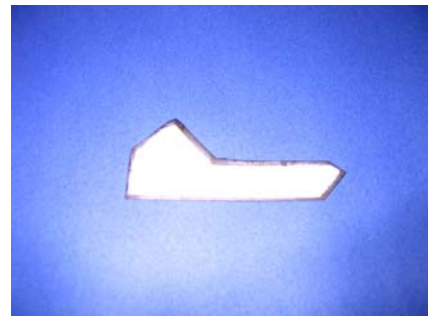
Piece 1-B - (Qty: 2) Patch for openings created by cuts in Piece 1 on wide end.



Pieces 2 & 3 - (Qty: 1 & 1) Interior layer meant to have flaps that can be overlapped. Piece 3 is the mirror or Piece 2.



Piece 2-A - (Qty: 4) "Triangle Patch" used to cover large opening created by cuts in Pieces 2 & 3.



Piece 2-B - (Qty: 4) "L Patch" used to cover openings created by cuts in Pieces 2 & 3.

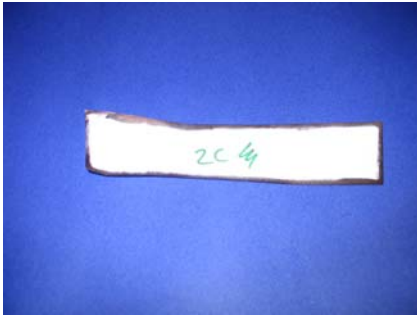
### B.2.2 Lay-up Instructions

The actual lay-up of the part can begin once the mold has been coated with release agent, the foam rib and bagging have been prepared, and the pre-preg material has been cut to size. The pre-preg material must be carefully placed into the mold in order to obtain a good surface finish. It is critical that the layers are positioned properly with respect to each other in order for the part to be strong and to have a good surface finish.

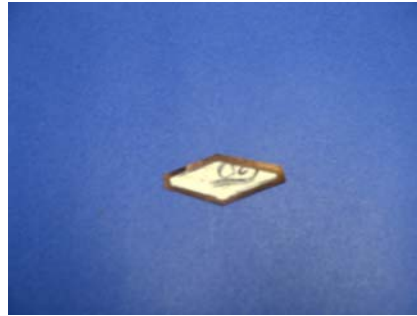
### B.2.3 Air bag setup

Once the lay-up is complete and the mold is closed, the air bags are ready to be inflated.

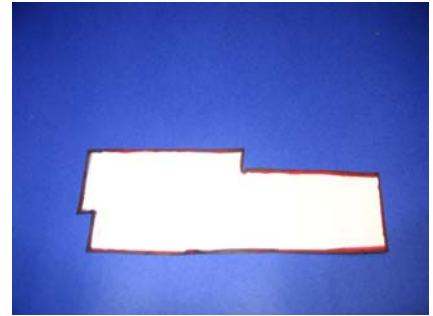




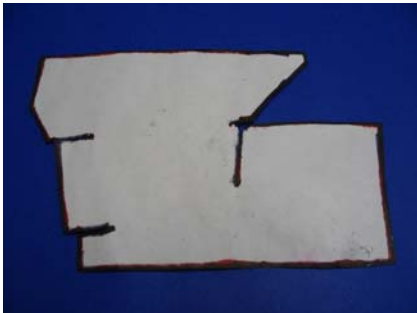
Piece 2-C - (Qty: 2) "Rectangle Patch" used to cover wide opening created by folding over flaps from Pieces 2 & 3.



Piece 2-D - (Qty: 8) "Diamond Patch" used to cover any small voids caused by folding over Pieces 2 & 3.



Piece 4 & 5 - (Qty: 1 & 1) Sheet meant to be wrapped around end plugs on thin end of piece, creating two additional layers. Piece 5 is the mirror or Piece 4.



Piece 6 & 7 - (Qty: 1 & 1) Sheet meant to be wrapped around end plugs on wide end of piece, creating two additional layers. Piece 7 is the mirror or Piece 6.



View of all pieces showing the relative sizing.



Each of the pieces of pre-preg material should be kept in the freezer until the time when they must be placed into the mold. Otherwise the material becomes very tacky and hard to maneuver.



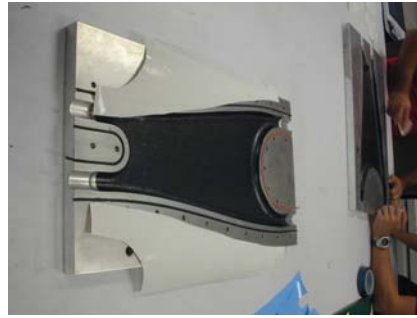
Piece 1 is the first to be placed. One piece must be placed carefully on the top of the mold, and similarly another on the bottom of the mold.



The piece should be smoothed out in order for it to cover directly up to the edge of the mold.



Part 1-A and Part 1-B are placed around the curve where openings remain on the thin and wide side of the mold.



The pieces of paper removed from the pre-preg material should be used to ensure that Piece 2 does not stick to the aluminum.



Piece 2 is then placed on top of Piece 1 into the bottom of the mold. It must be smoothed out along the areas where it touches Piece 1.



Similarly, Piece 3 must be placed on top of Piece 2 in the bottom of the mold and smoothed out. Again, scrap paper should be used to ensure that the flaps from Piece 3 do not stick to those from Piece 2.



Piece 4 (and Piece 5) is wrapped around the two-piece end plug. Sticking the material to the bagging should be avoided.



It is important that the piece is wrapped very tightly. This ensures that two full layers are obtained from the piece.



Piece 6 (and Piece 7) is wrapped around the one-piece end plug. Again, letting the bag stick to the material should be avoided.



The piece of material should be wrapped around tightly close to the end plug. At the outside edge, the material should gain a bit of a taper to mimic the part.



The foam rib should be placed in the middle of the part. The large end must be pressed firmly against the edge of the mold to ensure a good finish.

#### B.2.4 Oven setup

With the mold providing external pressure on the part and the air bags providing internal pressure, the part is finally ready to be cured. The entire setup must be placed in an oven to cure the pre-preg material.



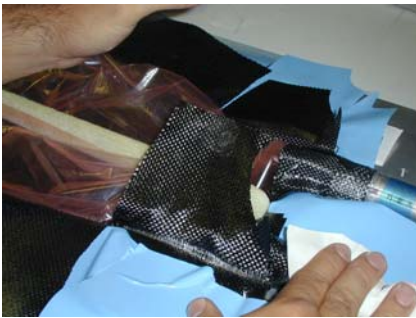
The bags (with the ends attached) are to be placed such that they cover the entire material surface. It must be placed such that it doesn't get caught up and fold over itself.



The end plugs should be forced all the way into the appropriate openings. The outside face of the plug should match that side face of the mold.



The flaps from Piece 3 are to be stretched over the end plug. The two ends of the flaps should meet up to form a complete layer.



The second largest flaps are next to be wrapped over. The small flaps within the curve are flapped over top of those.



The large flaps are last to be wrapped over. There is about  $\frac{3}{4}$ " overlap, so there is no need to stretch the material.



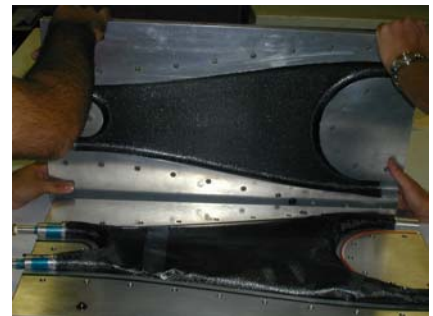
The "Triangle" and "L" patches are placed into the voids created by the latest wrap-overs.



The "Rectangle" patch is the last one to be added.



All the flaps for Piece 2 are then wrapped over, and the patches added. All the material within the bottom mold should now fit within the edges.

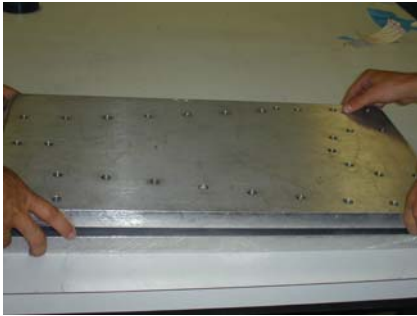


After having pressed everything down to ensure no pinching, the top of the mold should be placed on to the bottom.

**Program:** Saved as "PRT NO. 2"

**Cure Schedule:**

- 1 hour to get to 180 F;
- 4 hours at 180 F;



The top should be pressed down to allow the part to close.



The mold is then secured closed using cap screws.



A simple manifold is created using heat resistant air tubes and T-joints.



The air input is attached to the air supply using a set of quick-disconnect hose couplings.



The pressure regulator is used to obtain the desired pressure to be maintained throughout the curing process.



The pressure gauge reads 40 psi.

**Pressure Regulation** The pressure of the air bags should be: Internal Pressure: 40 psi

- 1 hour of cooling to get to room temperature.

**Cooling:** The oven doors should be opened to facilitate cooling once the curing cycle is done.

### B.2.5 De-molding

Once the part has cooled to room temperature following curing, the mold may be opened up.



The TPS Blue M oven is used to cure the part.



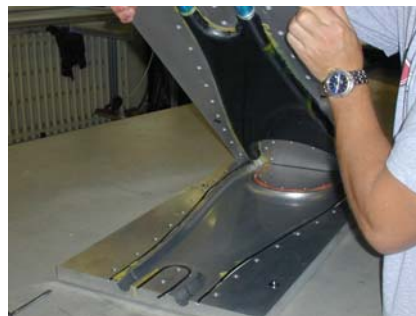
Once the oven is turned on, a program must be made to describe the curing cycle.



The oven control panel stores the program, after which a simple 'Start' is needed to begin.



The cap screws must be loosened at about the same rate. Otherwise much greater torque is needed to unscrew the mold.



Opening the mold reveals a shiny new part with bits of excess resin along the edges.



A great deal of post-machining work is needed to finish the part.

## B.3 Post-Machining

### B.3.1 Trimming rough edges

During the time when the part is curing, all excess resin is pushed to the edges of the part. Also, any pinching of the carbon fibre material will produce sharp edges coming out of the part. The unwanted rough edges on the part must be trimmed away.



A rough cutting bit is used with a Dremel rotary tool to trim the rough edges.



By passing the rotary tool along the edge of the part, a nice smooth finish can be obtained.

### B.3.2 Removing the end plugs

The aluminum end plugs used during the molding process are needed to maintain an inner diameter of 1". Since there is some carbon fibre that wraps around the part, removing the end plugs requires some careful application of force to the part.



Using a cutting head on the Dremel rotary tool, some material must be removed from the lip on the outside of the end plug.



Cut along the edge of the lip of the end plug to free the part.



On the wide end of the part, simply twisting the end plug will loosen it enough to be removed.

### B.3.3 Removing the vacuum bagging

The bagging used to create internal pressure in the part can be removed once the part is completely molded since it no longer serves any purpose. Removing the bag consists of twisting it until it is no longer stuck to any part of the inside of the actuator arm.

### B.3.4 Cutting ends to size

Before the inserts can be bonded into the part, the ends must be cut to the size needed in order to obtain the proper total length of the actuator arm.



The removal of the end plug must be done very carefully so as not to crack or damage the carbon fibre part.



On the thin side of the part, twisting will help to loosen the two-piece end plug.



The two-piece end plug must be cautiously knocked out. Once the sealing tape is cut, the air input part can be removed and cut away from the bag.



By grabbing on to the end of the bag using a set of pliers, the bagging can be twisted.



The bag will slowly remove itself from the inside of the part as it is twisted and pulled out.



The bag is removed.



A cutting jig was made in order to cut the part down to the right side.



A diamond tip rotary saw is used to cut the carbon fibre ends.



The wood cutting jig is aligned with the cutting table, and the end of the wood is lined up with the cutting blade.

### B.3.5 Preparing parts for bonding

In order to obtain the best possible bond, it is important that the surface being bonded together be cleaned.



The inside diameter of the end must be filed down slightly such that any imperfections do not block the inserts from entering properly.



The inserts are placed into the open ends and the part is test fitted into the bonding jig.



If the ends are too long (such that there would be initial loading on the ends), they should be filed to the right size.



The part is cleaned by evacuating all the particles of dust and carbon that remain around the bonding surface using compressed air.



The surface of the aluminum inserts is sanded lightly to clean away any dirt.



The surface is then cleaned using Acetone and dried.

### B.3.6 Bonding inserts into part

Once the surfaces to be bonded have been cleaned, the special adhesive can be prepared. The adhesive used was selected specifically for the purpose of bonding the aluminum inserts to the carbon fibre part.



The adhesive comes in two separate containers: a pink paste and a blue liquid.

#### **Hysol EA 9309.3NA Epoxy Paste Adhesive**

Resin Mix (100/22 ratio)

**Part A (Pink)** 10.0 g

**Part B (Blue)** 2.2 g

For information, the resin has a pot life of about 35 minutes.





A digital scale is used to ensure that the adhesive is mixed in the right proportions by weight.



The pink paste must be weighed out first since it is difficult to obtain an exact quantity.



The blue liquid is added to the pink paste in proportion. Pink:Blue = 100:22



The mixture must then be stirred until a consistent purple colour is obtained.



The adhesive should first be applied to the inside of the ends on the wide side of the part.



Next, the metal inserts (already secured to the " bar) should have the adhesive applied to them.



The wide end of the part should then be slid carefully onto the inserts.



The adhesive should now be applied to the inside of the ends on the thin side of the part.



Next, the inserts for the thin side (already slid onto the 6mm bar) should have the adhesive applied to them.

### B.3.7 Curing and Post-Curing

The last step towards a finished part is the curing and post-curing of the adhesive. The part must first be cured at room temperature, then post-cured at 180 F. During the initial curing, the part is fully constrained by the bonding jig. A weight placed on top of the part will ensure that it rests on the spacer bars.

**Cure Schedule:**     • 12 hours at room temperature, with support tooling

**Post-Cure Schedule:**     • 30 minutes to get to 180 F

• 1 hour at 180 F



Being careful not to give it an initial loading, the part should be placed into the bonding jig.



Any excess adhesive must be wiped away such that there is no purple paste left on the exterior of the part.



The alignment bars must then be fastened into place using a set of screws on each corner.



In order to cure the part in a clean environment, it is placed in an oven.



The part is cured for 12 hours at room temperature in the bonding jig.



The part then taken out of the jig and the alignment shafts are removed.



A smaller oven is used to post-cure the part.



The part by itself is placed in the oven to be heated at 180 F for 1 hour.



A post-curing cycle is programmed into the oven control panel.

- 15 minutes of cooling to get to room temperature.

**Cooling:** • The oven doors should be opened to facilitate cooling once the curing cycle is done.



Figure 78: The carbon fibre actuator arm is complete.